
Faculty of Engineering, Built Environment and Information Technology

# The coupled effect of surface roughness and nanoparticle size on the heat transfer enhancement of nanofluids for pool boiling

Sidhant Kumar

16041535

Submitted in partial fulfilment of the requirements for the degree of

Master of Engineering In Mechanical Engineering

in the

Department of Mechanical and Aeronautical Engineering

UNIVERSITY OF PRETORIA

12/31/2021

Supervisor:

Prof. M Sharifpur

Co-Supervisors:

Dr Mahdavi, Mostafa & Prof Meyer, Josua P.

# TABLE OF CONTENTS

# LIST OF FIGURES

## LIST OF TABLES

# Nomenclature

| | | | |
|---|---|---|---|
| $A_i$ | Interfacial area ($m^2$) | $Ja$ | Jakob number |
| $C_w$ | Lift coefficient | $k$ | Thermal conductivity (W/mK) |
| $C_L$ | Lubrication coefficient | $M$ | Molecular weight (g/mol) |
| $C_D$ | Drag coefficient | $\dot{m}$ | Mass transfer (m/s) |
| $C_p$ | Specific heat (J/kg.K) | $N$ | Avogadro's constant (units/mole) |
| $C_{wt}$ | Bubble waiting time coefficient | $N_w, NSD$ | Nucleation site density |
| | | $Nu$ | Nusselt's number |
| $CHF$ | Critical heat flux ($w/m^2$) | $P$ | Pressure |
| $d$ | Diameter (m) | $Pr$ | Prandtl number |
| $d_b$ | Bubble departure diameter (m) | $\dot{q}$ | Heat flux ($w/m^2$) |
| $F$ | Force (N) | $Ra$ | Surface roughness (m) |
| $g$ | Gravitational acceleration ($m/s^2$) | $Re$ | Reynolds number |
| | | $S$ | Source term ($N/m^3$) |
| $h, HTC$ | Heat transfer coefficient ($W/m^2K$) | $T$ | Temperature (K) |
| | | $UDF$ | User defined function |
| $h_{fg}$ | Enthalpy of vaporization (J/kg) | $V, U, u$ | Velocity (m/s) |

**Greek letters**

| | | | |
|---|---|---|---|
| $\alpha$ | Phase volume fraction | $\rho$ | Density ($kg/m^3$) |
| $\theta$ | Contact angle | $\sigma$ | Surface tension (N/m) |
| $\lambda$ | Bulk viscosity | $\tau$ | Shear stress ($N/m^2$) |
| $\mu$ | Viscosity (Pa.s) | $\varphi$ | Volume fraction |

**Subscripts**

| | | | |
|---|---|---|---|
| $bf, f$ | Base fluid | $s$ | Surface |
| $l$ | Liquid | $sat$ | Saturation |
| $nf$ | Nanofluid | $sub$ | Subcooled |
| $p$ | Particle | $sup$ | Superheat |
| | | $v$ | Vapour |

## Abstract

In the present work, the combined effect of surface roughness and nanoparticle size, also known as surface-particle interaction parameter (SPIP) and defined as the ratio of surface roughness to the particle size, was investigated numerically by simulating nanofluid/vapour two-phase pool boiling inside an unsteady 2-D symmetric chamber consisting of a heat sink as the heated wall. To account for the SPIP, new correlations for bubble departure diameter and nucleation site density were implemented as a user-defined function in ANSYS Fluent. The bubble waiting time coefficient was corrected at different nucleation site density during validation study where good agreement was found and then the same bubble waiting time coefficients were used during the rest of the investigations accordingly. The effect of nanoparticle concentration, fin aspect ratio, number of fins and different base fluids were also investigated. Aluminium oxide was used as the nanoparticle throughout this study. The results showed that when the SPIP is near 1, the lowest heat flux is achieved and thus will always show an inferior performance in heat transfer when compared to pure water. As SPIP increases past 1, higher heat transfer coefficient and heat flux is achieved and thus will show an enhancement in heat transfer performance when compared to water at appropriate concentrations. When SPIP is lower than 1, the heat flux is lower than when SPIP is higher than 1 but still higher than when SPIP is near 1. It was also found that as the number of fins and fin aspect ratio increases, the heat transfer coefficient increases. There is, however, a deterioration in heat transfer when the nanoparticle concentration increases. It was found that at SPIP close to 1, water based nanofluid always shows far better heat transfer capabilities than refrigerant based nanofluids. However, at SPIP: 16, R245FA based nanofluid achieves higher heat flux than water based nanofluid at higher wall superheat temperatures.

Keywords: Nanofluids · ANSYS-Fluent · Pool boiling · Heat sink · Surface-particle interaction parameter.

# 1. Introduction

In literature, most of the nanofluid pool boiling studies focus on investigating the effect of concentration, base fluid, geometry, surface roughness, particle type etc. on an individual basis and it is common to find that in some studies, the heat transfer coefficient has deteriorated while in some studies, it has enhanced when compared to pure water. This is because the experiments are carried out at different surface roughness to particle size ratio (surface-particle interaction parameter) and thus give different outcomes. This ratio must be carefully considered as it greatly influences the heat transfer performance of the nanofluid pool boiling and was the main focus of this study. Few experimental studies have been carried out studying this ratio but numerical studies are rare. For this reason, present study has been carried out to understand the effect of this ratio from the perspective of a numerical simulation.

Technological advancements have made it possible for humans to do much more than we could before. Advancements have been made in many areas such as power plants, automotive, solar-thermal systems, air conditioning, and microelectronics to increase their performance to keep up with the world's demand. However, with an increase in performance and output in high energy devices, there comes an increase in heat generation and cooling demand.

High heat flux generating devices are challenging to keep cool as traditional cooling methods such as air cooling cannot keep up. To overcome this problem, liquid cooling systems are used as they provide better cooling than air. The cooling heat flux in two-phase liquid systems is typically in the thousands of $W/m^2$, which is more significant than single-phase liquid systems (Faulkner, Khotan & Shekarriz, 2003). For this reason, boiling liquids is by far the most effective method for heat transfer.

Commonly, the two-phase systems use only the base fluids such as ethylene glycol (EG), water, oil, and refrigerants. However, their effectiveness is affected because of their limited heat transfer performance and poor specific properties value. They are unable to meet the cooling requirement of high heat flux devices. This forces system performance to be limited to avoid overheating. Nevertheless, by including nano-scale particles into the base fluids mentioned earlier, the fluid properties such as thermal conductivity can be dramatically enhanced, bringing quantifiable improvements in pool boiling performance.

Today, many industries use pool boiling heat transfer and are commonly found in refrigeration applications, power plants, high heat flux electronics, nuclear reactors, and others. Therefore, improvements in pool boiling heat transfer are of utmost importance to further improve efficiency.

Although nanoparticle addition in the base fluid brings about favourable enhancements in the thermal conductivity, it is not the only factor affecting heat transfer performance. At higher concentrations, the effect of nanoparticle deposition on the heating surface plays a crucial role as it influences crucial factors such as nucleation site density.

When nanoparticles deposit on a surface cavity, they can either clog the cavity where bubbles are produced and decrease the nucleation site density or split the cavity, which increases bubble nucleation sites and promotes heat transfer. This all depends on the particle size and the surface roughness.

Therefore, explicit knowledge of this critical mechanism is necessary to achieve the optimum surface roughness and particle size for maximum heat transfer. However, most studies in the literature have focused on the experimental investigation of this mechanism, whereas numerical investigations are rare. Therefore, this research focuses on the numerical analysis of the particle size and surface roughroughness's coupled effect

## 1.1 Problem statement

Every two years, the number of transistors will increase two folds, as Moore’s law states. The increase in transistors will increase the heat generation that is apparent in our computers today. This increase poses a considerable problem for cooling work-intensive computers and servers and limits system performance. Over the years, various techniques were in use to enhance the cooling of the processors, such as using a thermal interface material (Thermal paste) between the CPU and heatsink or even submerging the computer in a conductive liquid such as mineral oil, known as server immersion cooling (Walters, 2012). Phase change coolers were also used to cool computer processors, which use heat from the processor to evaporate the liquid, which runs in a vapour compression cycle. However, these conventional cooling methods limit their heat transfer rate, after which maintaining the desired temperatures

becomes difficult. Due to this reason, often, the performance needs to be sacrificed and limited. There is, therefore, a need for a method that can allow high heat flux cooling by having a higher heat transfer coefficient. As Figure 1 suggests, air or water cooling has a low heat transfer coefficient magnitude.

In contrast, for cooling applications, water boiling methods have the highest order of heat transfer coefficient, and for this reason, pool boiling is favourable. However, this method's heat transfer coefficient could be enhanced using nanofluid instead of conventional fluids such as water. This enhancement is the focus of this research and is discussed in the following sections in detail.

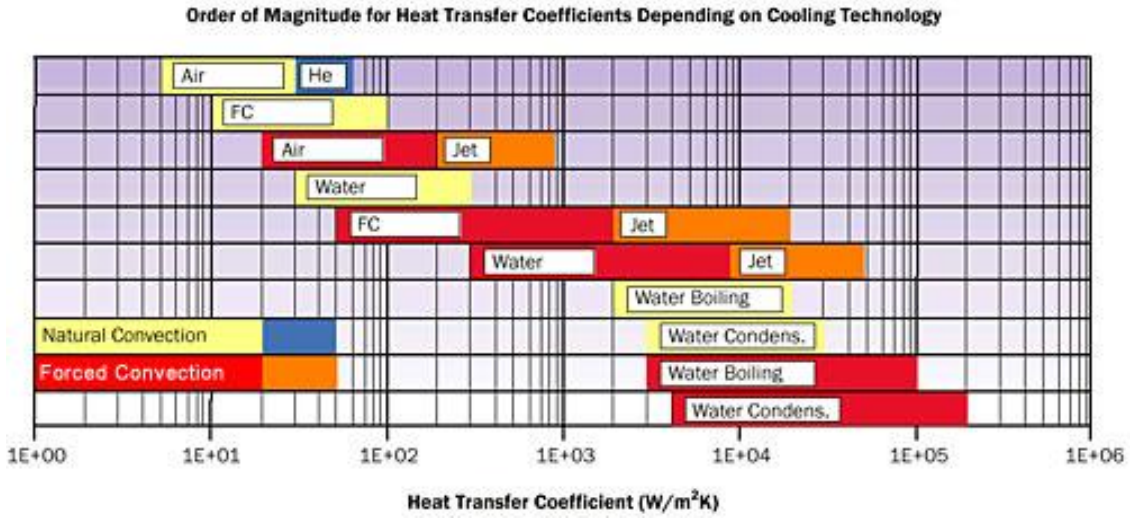


***Figure 1*** *Attainable heat transfer coefficients (Lasance, 2005).*

Although many studies have been carried out on nanofluid pool boiling, there are contradicting findings on enhancing heat transfer performance. Some studies report that the addition of nanofluids does improve the heat transfer performance, whereas, in some studies, it was found to cause deterioration.

Hence, there is no clear understanding of what decides the heat transfer performance when nanoparticles are added. There is, therefore, a need to better understand the crucial factors that play an essential role in determining this outcome. Few factors that significantly impact heat transfer performance are surface roughness, particle size, and their interactions. Therefore, by better understanding these factors, a more accurate prediction can be made on whether a set of parameters will lead to an enhancement or deterioration in heat transfer. An optimum point can also be found where the benefits of nanoparticle addition are at their maximum.

## 1.2. Methodology

The objective of this study was to understand the combined effect of the heater surface roughness and nanoparticle size on the enhancement of heat transfer performance. To do this, ANSYS Fluent was used to simulate nanofluid pool boiling in a 2D symmetric chamber consisting of a heat sink. Literature review was carried out to understand the models used and their accuracy and were implemented in this study. A user defined function was used to import a new nucleation site density equation into Fluent that is not only suitable for nanofluids, but also takes into account the ratio between surface roughness and particle diameter. A new and more accurate correlation was also implemented for bubble departure diameter using user defined function. A validation study was carried out and a new correlation for bubble waiting time coefficient was developed which was then used during the investigation. The influence of other parameters such as fin aspect ratio, particle concentration, fin number and different base fluids were also investigated. Where applicable, the results were compared to pure water to understand when can an improvement or degradation in HTC be expected.

# 2. LITERATURE STUDY

## 2.1 Nanofluids

The size modification of these particles to micrometre and millimetre scale to achieve enhanced fluid performance has not been successful. Moreover, they still had drawbacks such as high-pressure drops, particle deposition, clogging, minor thermal conductivity enhancement, and could cause corrosion in the system. Thus, there is an interest in the particles now at the nanoscale to study their performance in heat transfer applications.

Advancements in nanotechnology and increased nanoparticles' availability have allowed for a spike in nanofluid research. They have gained popularity as a new heat transfer fluid because of their higher heat transfer performance and a wide range of applications. Nanofluids are mixtures that contain nanoscale solid particles of less than 100 nm in size in a conventional heat transfer fluid such as water, ethylene glycol, oil, and others. Since metallic liquids have a higher thermal conductivity than non-metallic, the nanoscale particles are mostly metal (silver, copper, gold, and iron) or oxide of metal (copper oxide, silica, Titania, and alumina). However, non-metallic particles (Graphite, diamond, and carbon nanotubes) and hybrid nanoparticles are also used (Ali *et al.* 2018). The nanofluid's thermal conductivity depends on the nanoparticle shape, dimensions, added volume fraction, thermophysical properties, acidity, base fluid type, nanofluid temperature, clustering, and additives (Eggers & Kabelac, 2016).

The thermal conductivity and the fluid's dynamic viscosity affect the heat transfer behaviour the most (Ahmadi *et al.* 2018). The nanoparticles have the effect of increasing the dynamic viscosity and the thermal conductivity of the base fluid. An increase in thermal conductivity increases the convective heat transfer of the fluid, while an increase in the dynamic viscosity decreases the convective heat transfer. Nanoparticles have a higher surface area to volume ratio than microparticles, which explains why nanofluids have a higher thermal conductivity than micro fluids and pure fluids; hence why they are preferable in heat transfer applications. Nanofluids are also more desirable than micro fluids in high-performance microprocessors and other applications because of their ability to flow in microchannels without clogging, allowing devices to be compact and still run with high accuracy (Salman & Mohammed, 2013).

Nanofluids also open the possibility of a more efficient, compact, cost-effective, and lighter design for cooling systems with higher thermal performance.

Two methods are used to produce nanofluids, namely one- and two-step methods. The one-step method involves the direct formation of the nanoparticle in a base fluid, while the two-step method involves separate preparation of nanoparticles mixed into the base fluid. To obtain a stable suspension, surfactant use, controlling the pH, and ultrasonic vibrations can be applied for both methods. According to past research, nanofluids have an incredible potential to bring heat transfer improvements in areas mentioned earlier. In the two-step method, the synthesis and dispersion are done simultaneously. The one-step method produces fluids with stable and uniformly suspended particles. This is because the need to dry, store and transport the nanoparticles is removed by this method, which helps keep the unwanted aggregation of nanoparticles at a minimum, thus increasing the fluid's stability (Uppal, 2018).

Nanofluids are commonly prepared using the two-step method, which is also economical. In this method, the nanoparticles are first made as dry powders by using chemical and physical methods. The powder then gets dispersed into the base fluid using external stirring or mixing techniques such as ultrasonic agitators, magnetic agitators, ball milling, high shear mixing, and homogenizing. Since the nanoparticles have a high surface area, they accumulate together (Uppal, 2018).

### 2.1.1 Nanofluid applications

Nanofluids have a wide range of applications where they can potentially be used to bring performance enhancements. In this section, a few of the many applications are discussed.

*Electronics applications* – We have seen that technology is continuously improving to be as compact as possible to facilitate the use, storage, and transportation over the years. However, a more compact design makes the dissipation of heat a problematic task since a smaller heat transfer area is available. An efficient thermal management system is crucial for next-generation electronics devices to operate without thermal throttling. Nanoparticles, which can increase the coolant's thermal conductivity, are desirable in this application as nanofluids can have a higher heat transfer coefficient, thus making a compact arrangement possible. In addition, Nanofluids decrease the

temperature difference between the coolant and the heated surface, which in this case is usually a heat sink with microchannels through which the coolant flows.

*Transportation* – The automotive industry can reduce the complexity and thus lower the weight of the thermal management system by using nanofluids that can, in turn, increase thermal and fuel efficiency, which can be beneficial to the environment as well. The better thermal management system also allows engines to generate greater horsepower without increasing the cooling system's size. Since nanofluids have a higher boiling point, they can operate at higher temperatures and reject more heat from the existing cooling system. Nanofluids can also allow the radiator to be smaller and placed at any other location, thus allowing for a more aerodynamic design to be used.

*Nuclear systems* – There is a constant need to increase nuclear reactors' efficiency, safety, and power density. With nanofluids in the pressurised water reactors (PWRs), the critical heat flux is higher, increasing the power density without changing the current fuel assembly. Nanofluids can also be used for emergency core cooling systems (ECCs) of boiling water reactors and PWRs.

*Industrial cooling* – For the electric power industry in the US alone, Barreneche *et al.* (2020) mention that up to 30 trillion Btu per year could be saved by using nanofluid in their cooling cycles enough to power up to 150,000 homes for a year. This would also bring emission cut by millions of metric tons of carbon dioxide.

### 2.1.2 Nanofluid properties

Since nanoparticles are suspended in the base fluid, this changes fluid properties and may be determined as a function of the nanoparticle parameters such as size and volume concentration $\varphi$. There are numerous correlations in the literature to calculate mixtures properties, but they should be carefully selected as they may not be accurate to nanofluids applications. This section presents the correlations proven to be accurate for nanofluids to model each property.

An interfacial nanolayer is formed between the nanoparticle and the base fluid in nanofluids, as shown in Figure 2. The nanolayer is formed due to the fact that nanoparticles have a very high surface area to volume ratio and thus, posses a higher surface energy. Due to this surface energy, there is a tendency for nanoparticles to

agglomerate surrounding particles to minimise their excess surface energy which leads to the formation of nanolayer. According to Sharifpur *et al.* (2016), using the mixture model for nanofluid density calculation provides an overestimation and only worsens with an increase in particle concentration. For this reason, it was suggested by the authors that for particle concentrations of 1% vol. and beyond, the nanolayer must be taken into account for density calculation.

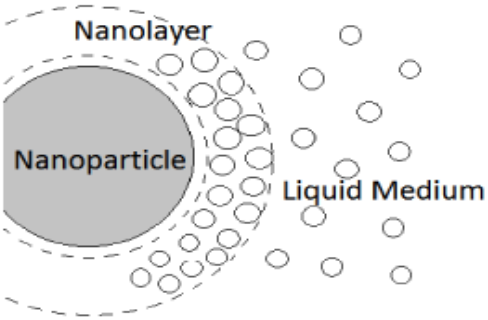


***Figure 2*** *Formation of nanolayer around nanoparticle and fluid interface (Simpson et al., 2018).*

For volume fractions greater than 1%, the effect of nanolayer needs to be considered. The nanofluid density after adjustment for nanolayer thickness $\rho_{nf}$ can be determined according to Sharifpur *et al.* (2016) as:

$$\rho_{nf} = \frac{\rho_1}{(1-\varphi) + \varphi(r_p + t_v)^3 / {r_p}^3} \quad (1)$$

Where

$$\rho_1 = \varphi\rho_p + (1-\varphi)\rho_f \quad (2)$$

$$t_v = -0.0002833{r_p}^2 + 0.0475 r_p - 0.1417 \quad (3)$$

Where $r_p$ stands for the average radius of the nanoparticle, $t_v$ represents nanolayer thickness, $\rho_1$ is the density of nanofluid before adjusting for nanolayer thickness and $\rho_f$ and $\rho_p$ are the density of the base fluid and the nanoparticle, respectively. The specific nanofluid heat capacity $Cp_{nf}$ at fixed pressure can be expressed as:

$$Cp_{nf} = \frac{(1-\varphi)\rho_f Cp_f + \varphi\rho_p Cp_p}{\rho_{nf}} \quad (4)$$

The viscosity of the nanofluid $\mu_{nf}$ can be determined according to Corcione (2010) as:

$$\frac{\mu_{nf}}{\mu_f} = \frac{1}{1 - 34.87(d_p/d_f)^{-0.3}\varphi^{1.03}} \quad (5)$$

Where $d_p$ is the nanoparticle diameter and $d_f$ represents the equivalent diameter of the base fluid molecule:

$$d_f = \left[\frac{6M}{N\pi\rho_f}\right]^{\frac{1}{3}} \quad (6)$$

Where $N$ Is the Avogadro's constant, $M$ represents the base fluid's molecular weight, and the base fluid density is evaluated at 293 K. For water, $d_f = 0.3x10^{-10}\ m$.

The surface tension of the mixture can be calculated according to Meissner and Michaels (1949) as:

$$\frac{\sigma_f - \sigma_{nf}}{\sigma_f} = -7.773x10^{-3}\ln\left(\frac{\varphi}{7.673x10^{-7}} + 1\right) \quad (7)$$

Where $\sigma_f$ and $\sigma_{nf}$ are the surface tension of the base fluid and nanofluid, respectively.

The thermal conductivity for the nanofluid $k_{nf}$ can be determined by using the Maxwell model for spherical nanoparticles for *less than 1% volume fraction*:

$$\frac{k_{nf}}{k_f} = \frac{k_p + 2k_f - 2\varphi(k_f - k_p)}{k_p + 2k_f + \varphi(k_f - k_p)} \quad (8)$$

A more accurate model should be used for a volume fraction greater than 1%. For CuO/water and $Al_2O_3$/water nanofluids, for example, a more accurate model is available by Khanafer and Vafai (2011) as:

$$\frac{k_{nf}}{k_f} = 1 + 1.0112\varphi + 2.4375\varphi\left(\frac{47x10^{-9}}{d_p}\right) - 0.0248\varphi\left(\frac{k_p}{0.613}\right) \quad (9)$$

Where $k_f$ and $k_p$ are the thermal conductivity of the base fluid and nanoparticle, respectively.

### 2.1.3 Effect of different parameters on nanofluid property

The enhancement in thermal conductivity is believed to be the most important for nanofluids as this is the property that theoretically dictates the fluid's heat transfer capabilities. Thus, it is worthwhile to look at it in further detail. The nanofluid's thermal conductivity and other properties may be influenced by the base fluid, particle

concentration, size, shape and material, additives and their concentrations, and other parameters. The acidity of the nanofluid also plays an important role.

#### 2.1.3.1 Thermal conductivity

Agarwal *et al.* (2016) showed that using water as base fluid leads to the highest thermal conductivity ratio followed by EG and engine oil when used with CuO nanoparticles, and the ratio increased linearly with volume fraction. In contrast, Wang *et al.* (1999) used $Al_2O_3$ and CuO particles with different base fluids such as engine oil, vacuum pump, ethylene glycol, and water and showed that when the base fluid was ethylene glycol, the greatest thermal conductivity ratio was achieved.

Alawi *et al.* (2018) compared different particle shapes for nanofluids. They found that spherical nanoparticles lead to higher thermal conductivity for $Al_2O_3$, CuO, and ZnO in water, followed by cylindrical bricks, blades, and platelets. However, $SiO_2$/water showed the lowest thermal conductivity with spherical shaped particles. Xie *et al.* (2002) determined the thermal conductivity of spherical and cylindrical SiC nanoparticles in water and EG and found that nanofluids with cylindrical-shaped particles had a higher thermal conductivity. Murshed *et al.* (2005) experimented using rod-shaped and spherical $TiO_2$ nanoparticles in water (5% vol.) and concluded that nanofluid with rod-shaped particles showed a higher thermal conductivity.

From their experiment, Das *et al.* (2003) concluded that the thermal conductivity of $Al_2O_3$/water and CuO/water at 1% and 4% vol. Increases almost linearly with temperature, whereas Sharifpur *et al.* (2017) showed that α-$Al_2O_3$-glycerol nanofluids showed no temperature dependency. Li and Peterson (2006) also investigated $Al_2O_3$/water and CuO/water's thermal conductivity and found that the thermal conductivity ratio increases with temperature and concentration.

Lee *et al.* (1999) also noted that although $Al_2O_3$ particles have a higher thermal conductivity as a material, CuO-based nanofluid showed a higher improvement in thermal conductivity. The authors mentioned that the cluster formation of $Al_2O_3$ in the base fluid was the reason for this behaviour. The results of Alawi *et al.* (2018) show that $Al_2O_3$ in the water had the highest thermal conductivity, followed by CuO, ZnO, and $SiO_2$.

Lee *et al.* (1999) found that the thermal conductivity ratio of CuO and $Al_2O_3$ in both EG and water increases linearly with volume fraction and drops exponentially with an increase in particle size. They found that the Maxwell model was inaccurate in predicting the influence of particle diameter on the thermal conductivity at 0.03% vol. concentration. Chopkar *et al.* (2008) studied the influence of particle size on thermal conductivity and found that when the nanoparticle's size decreases, the nanofluid's thermal conductivity rises.

Sonawane *et al.* (2015) investigated the influence of sonication time on enhancing the thermal conductivity of $TiO_2$ in EG, paraffin oil, and water. They showed that the thermal conductivity enhancement increases until 60 min and from this point onwards, it starts decreasing. They stated that this was due to an increase in Brownian motion and intermolecular interactions, leading to the clustering of nanoparticles, so the heat transfer and conductivity drops.

Wang and Li (2009) showed that the thermal conductivity ratio increases with pH and peaks at 7.5 and 9.5 for $Al_2O_3$/water and CuO/water, respectively, and then decreases from that point onwards. Regarding shear rates, the viscosity of water-based nanofluids is constant, which indicates that it is a Newtonian fluid.

#### 2.1.3.2 Viscosity

Adio *et al.* (2013), who investigated viscosity using γ-$Al_2O_3$-Glycerol Nanofluids, found that the apparent viscosity decreased with temperature. In contrast, the relative viscosity increases with temperature until 50 °C and then starts decreasing rapidly. Similarly, Sahoo *et al.* (2009) experimented with $Al_2O_3$/EG/water nanofluid and showed that the viscosity decreases exponentially with an increase in temperature at all tested concentrations. It is worth noting that conventional fluids show the same behaviour where the viscosity also decreases with temperature. In another experiment, Sundar *et al.* (2012) studied the effect of temperature up to 50 °C at different particle concentrations of $Fe_3O_2$/EG/water and reported an exponential decrease in viscosity with an increase in temperature.

In another research, Adio *et al.* (2016) concluded that as the ultrasonic energy increases, the viscosity of $Al_2O_3$-Glycerol decreases until an optimum point where the viscosity is at its minimum. They also showed that for nanofluids with a particle size of

20-30 nm, the viscosity decreases with an increase in sonication time until 6 hrs, from which point no further change is seen. However, for 80 and 100 nm particle sizes, the viscosity increased after 3 hours of sonication.

Chevalier *et al.* (2007) studied $SiO_2$/ethanol nanofluid's rheological behaviours (1.1%-7% vol) and reported that the viscosity increases with particle concentration. The same conclusion was drawn by Corcione (2011). Ji-Fen and Zhong-Yang (2009) also showed that the relative viscosity increases with concentration, where a higher increase is seen for smaller particle sizes.

Ji-Fei and Zhong-Yang (2009) investigated the viscosity of $SiO_2$/water and showed that the relative viscosity decreases exponentially with an increase in particle size at high concentrations. As the concentration decreases, the effect of increasing particle size on the viscosity decreases. Likewise, Nguyen *et al.* (2007) studied the effect of particle size on $Al_2O_3$/water nanofluid where 36 and 47 nm diameter particles were used. They found that at concentrations below 4% vol., no difference was seen in the viscosities, whereas, at higher concentrations, the nanofluid with bigger particle size had a higher viscosity. Some researchers show contradicting findings where the smaller particle size achieves a higher viscosity. In this case, the increase in viscosity was said to be due to an increase in surface area of solid-solid and solid-liquid interactions that increase the electro viscous effect in the nanofluid.

Ji-Fei and Zhong-Yang (2009) also studied the effect of pH on the viscosity. The viscosity was steady until around pH 5 where after that, viscosity spikes up from pH 5 to pH 6 depending on concentration and then starts to decrease gradually. However, with particle sizes larger than 20 nm, the pH had a negligible effect on the viscosity. Timofeeva *et al.* (2009) investigated the effect of pH on the viscosity of $Al_2O_3$ nanofluid. They found that the pH was independent of particle concentration except for when platelet particles were used where the pH increased with concentration. It was found that nanofluids with the lowest pH (bricks and blade-shaped) exhibited the lowest viscosity.

Sundar *et al.* (2012) investigated the effect of different EG/water concentrations on Fe3O2/EG/water viscosity. They concluded that as the EG concentration decreased, the viscosity of the nanofluid decreased. Wang *et al.* (1999) experimentally compared the viscosity of $Al_2O_3$ in two base fluids, namely water and EG. The viscosity was

increased by 20-30% when water was used as a base fluid and 40% when EG was used.

When it comes to particle shape, Timofeeva *et al.* (2009) concluded that elongated particles have higher viscosity at a given concentration. In contrast, spherical particles or spheroids with a low aspect ratio have a lower viscosity.

#### 2.1.3.3 Surface tension and density

Regarding surface tension, Bhuiyan *et al.* (2014) studied the effect of parameters on SiO2/methanol nanofluid's surface tension and found that there was a linear increase in surface tension as the particle concentration increases whereas the surface tension drops with a rise in temperature. They also found that surface tension enhancement compared to base fluid increases with temperature. $SiO_2$, $Al_2O_3$, and $TiO_2$ with water as base fluid were also studied, and a similar conclusion was drawn where $TiO_2$ showed the highest surface tension and $SiO_2$ showed the lowest surface tension. Their results showed that larger particles exhibit a higher surface tension.

Regarding density, Chavan and Pise (2019) carried out experimental investigations on the density of $SiO_2$, $Al_2O_3$ and $TiO_2$ in water and $SiO_2$/EG. Their findings show that an increase in temperature slightly reduces the relative density and that the relative density was higher for higher concentration nanofluids. Raja *et al.* (2018) experimented using Al, Cu, and Ag particles with different base fluids and found that EG had a slightly lower relative density than water but had a higher density than water due to the higher density of EG. They also noted that Ag nanofluids showed higher density enhancement than the rest.

#### 2.1.3.4 Specific heat

Chavan and Pise (2019) also showed that nanofluid's specific heat was less than their base fluid and decreases with increased concentration using the particles mentioned earlier. The nanofluids with Ag particles were found to have the smallest specific heat, and water-based nanofluids were found to have the smallest relative specific heat (most significant change in specific heat). Like most fluids, the specific heat of nanofluid also increases with temperature.

Raja *et al.* (2018) results indicate that specific heat decreases with concentration. The specific heat was lower than the base fluid for all base fluids and particle material combinations. Aluminium nanoparticles showed the lowest decrease in specific heat, followed by Cu and lastly Ag. Water-based nanofluids were shown to have the smallest decrease in specific heat, followed by EG and sodium-based nanofluids.

## 2.2 Pool boiling

Pool boiling is a two-phase technique that involves the immersion of a heating surface in a stagnant liquid, which causes the boiling of the liquid and a low-velocity motion of the liquid. Two types of pool boiling are considered: saturated pool boiling, Figure 3(a) and subcooled pool boiling, Figure 3(b).

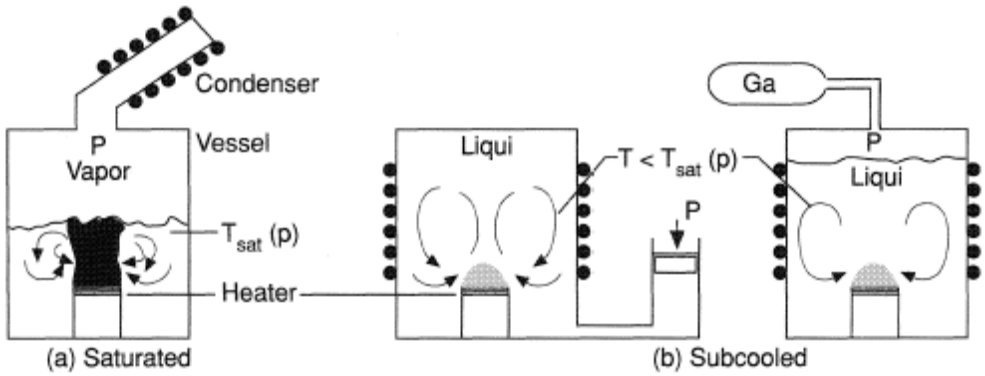


***Figure 3*** *Pool boiling techniques (Kenning, 2011).*

In saturated pool boiling, the fluid is kept at saturation temperature, which is dependent on the pressure. The vapour goes through the condenser, where it gets cooled back to liquid. The vessel's pressure depends on the cooling rate applied to the condenser, which can be controlled to vary the pressure and, thus, the saturation temperature. Pool boiling is also possible using subcooled liquid where the temperature away from the heater is lower than the saturation temperature (subcooled). The subcooled liquid makes it difficult for gas to escape, and thus heat sinks need to be used on the vessel wall to provide cooling (Kenning, 2011). The boiling starts when the heating surface temperature exceeds the pool's saturation temperature. There are various boiling regimes, as shown in Figure 4, where $\Delta T_{excess}$ is the difference in temperature between the heating surface and the saturation temperature. The boiling curve is unique to the liquid and the nature of the heating surface used.

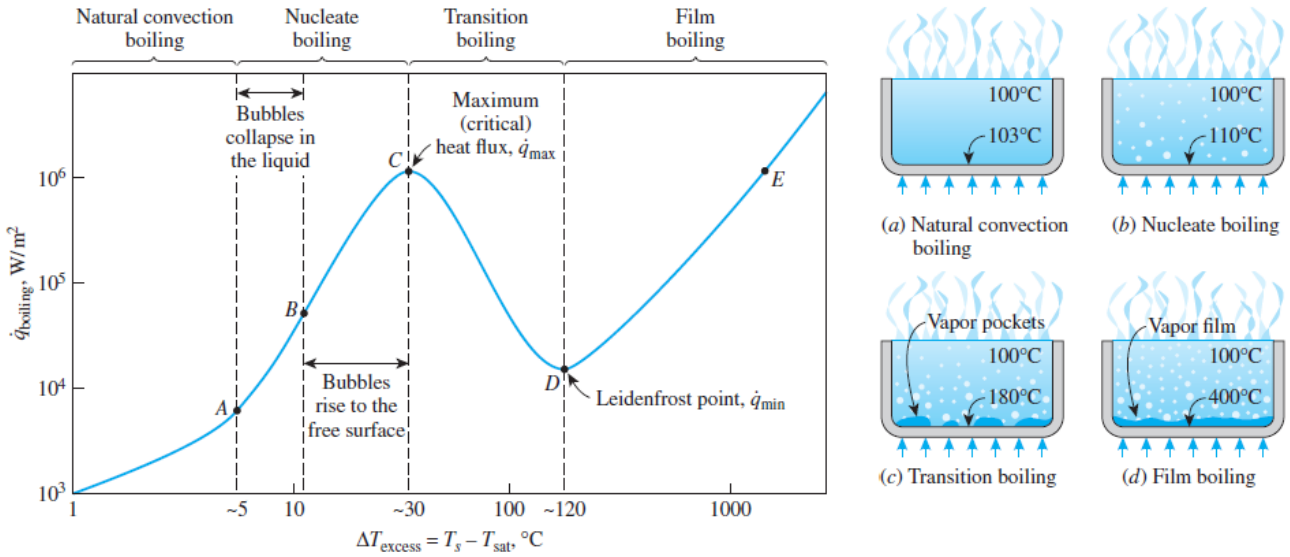


***Figure 4*** *Boiling curve (Ghajar & Cengel, 2015).*

This study's regime of interest is nucleate boiling, as this is where the heat flux achieves its maximum point called critical heat flux. In this regime, the number of nucleation sites increases as we move towards to critical flux point. In region A-B, isolated bubbles start forming on the heating surface but do not rise to the free surface. The rising of the bubbles causes agitation in the locality of the heater surface, which is why an increase is seen in the heat transfer coefficient and heat flux. The bubble formation and nucleation sites increase dramatically in region B-C, leading to a continuous vapor column. The bubbles now rise to the free surface, bursting and releasing vapor. As $\Delta T_{excess}$ increases during nucleate boiling, the rate of evaporation increases to the point where most of the heating surface is covered with bubbles, which makes it challenging for the surface to be wet by the liquid. So, the heat flux does not increase further and reaches the critical heat flux. In the transition regime, the heat flux starts to decrease. This is due to the vapor layer forming on the heating surface, which has a lower thermal conductivity than the liquid (Ghajar & Cengel, 2015). The heat flux in the nucleate boiling can be determined using the following formula by Rohsenow:

$$\dot{q}_{nucleate} = \mu_l h_{fg} \left[\frac{g(\rho_l - \rho_v)}{\sigma}\right]^{1/2} \left[\frac{c_{pl}(T_s - T_{sat})}{C_{sf} h_{fg} Pr_l^n}\right]^3 \quad (10)$$

Where $\dot{q}_{nucleate}$ is nucleate boiling heat flux, $\mu_l$ is the liquid viscosity, $h_{fg}$ represents enthalpy of vaporization, $\sigma$ is the surface tension of the liquid-vapor interface, $\rho_l$ represents liquid density, $g$ is the gravitational acceleration, $\rho_v$ represents vapor density, $c_{pl}$ is the specific heat of the liquid, $T_s$ is the heating surface temperature, $T_{sat}$ is the saturation temperature of the fluid, $C_{sf}$ is the experimental constant that is decided by the surface-fluid combination, $Pr_l$ is the liquid's Prandtl number, and $n$ is the experimental constant which is dependent on the fluid. All the properties are evaluated at $T_{sat.}$

According to Ghajar & Cengel (2015), the heat flux during nucleate boiling does not depend on the heating surface's geometry and orientation. However, the heat flux is significantly influenced by the surface condition. Therefore, the maximum or the critical heat flux may be determined using the equation by S.S Kutateladze as:

$$\dot{q}_{max} = C_{cr} h_{fg} [\sigma g \rho_v{}^2 (\rho_l - \rho_v)]^{1/4} \quad (11)$$

Where $C_{cr}$ depends on the heater geometry. The formulas listed so far are applicable for smooth surfaces only. Finned surfaces such as heat sinks are commonly attached to the processors using thermal paste, and thus the heating surface becomes the heat sink, which is submerged in the fluid, as shown in Figure 5. Often an auxiliary heater is also used if needed.

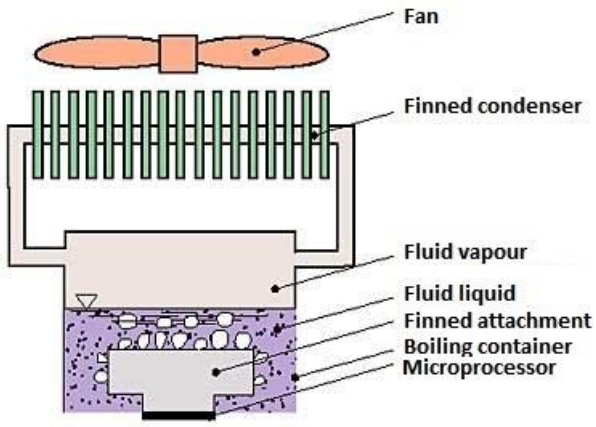


***Figure 5*** *Pool boiling set up for microprocessor cooling.*

There are two categories in which the pool boiling heat transfer enhancement methods may be classified, namely passive and active. The methods that fall into the active category use external power to achieve liquid rotation, surface rotation, mechanical

mixing, vibration, injection, suction, electrostatic, and magnetic field induction. In any case, the active methods have high costs and are unsuitable for applications requiring compact space. On the other hand, the methods that fall under the passive category do not require any external power but involve modifying fluid properties and the heat transfer surface, such as increasing surface roughness to promote more nucleation sites or increasing surface area by using fins or changing the shape and so on. (Bergles *et al.* 1979). Therefore, using nanofluids is a passive method since it changes the properties of the fluid.

## 2.3 Previous reviews on the use of nanofluids and boiling.

### 2.3.1 Experimental reviews

Numerous articles have been published on nanofluid pool boiling, where its effect on the critical heat flux (CHF) and the heat transfer coefficient (HTC) were investigated.

Ahmed and Hamed (2012) carried out a pool boiling experiment to understand the effect of particle deposition on heat transfer performance and to address the contradicting trends in HTC observed in the literature. They used a flat copper block and $Al_2O_3$/water with a 40-50 nm particle size at concentrations varying from 0.01% to 0.5% vol. They concluded that the uniformity and nanoparticle deposition rate depend on concentration, where deposition occurs at a lower rate for low concentration (0.01% vol), which enhanced the HTC. The enhancement at low concentrations could be mostly related to the increased thermal conductivity of the fluid rather than the effect of deposition. At higher concentrations, the HTC had degraded due to the deposition layer that decreased the nucleation sites and formed a layer of insulation. When the deposition rate was high, the layer was less uniform and left out areas of the heater uncoated and exposed, leading to HTC higher than expected when the deposited heater was used in pure water boiling.

Ayoobi *et al.* (2019) studied the effect of subcooled temperature at transient conditions ranging from 0°C (saturated) to 20°C using water and Al-Fe alloy heater wire under atmospheric pressure. The heating rate was increased linearly from 1s to 1000s. Their results show that as time progresses, the HTC increases since the heat flux increases. They also showed that as the degree of subcooled increases, the HTC increases up to 53.9% for 1s, and the CHF increases up to 436.7% for 1000s relative to saturation temperature. They concluded that the superheat temperature depends on the wire

material, rate of heat flux increase, and heat transfer mechanism. The temperature of the heater at CHF decreases with time for all subcooled temperatures.

Ayoobi *et al.* (2020) investigated the transient characteristics of $Fe_3O_4$/water ferrofluid pool boiling at 0.01% concentration and compared it to water using a Cr-Al-Fe wire heater. The fluid was at saturated temperature and atmospheric pressure. It was found that there was a decrease of CHF and wall superheat for both the ferrofluid and water, which lasted from 1 to 10 sec. and 1 to 100 sec., respectively. The CHF then increases from 10 to 5000 sec. for ferrofluid and 100 to 5000 sec. for pure water, where the ferrofluid showed a 160% increase in CHF compared to water. They concluded that the ferrofluid showed a higher HTC than water and the HTC increased with time. They mentioned that the boiling time affected the heat transfer characteristics because it influenced the amount of nanoparticle deposition on the heater surface. The bubble growth time and diameter were found to be smaller than for water, which increases wettability.

Bock *et al.* (2020) experimented on saturated pool boiling over roughened and nanostructured horizontal copper tubes using R-134a at 25 °C and 5 °C and R-245fa at 20°C. It was found that the nanostructured tube with a commercial nanocoating process (nanoFLUX) showed HTC that were up to 200% higher than that of the polished tube and outperformed other nanostructured tubes (Layer by layer and CuO) due to higher nucleation site density. The nanoFLUX surface had the highest HTC and CHF when boiling R-134a at 5 °C.

Chang and Bang (2005) experimented with pool boiling under atmospheric pressure containing 0.5%-4% vol. $Al_2O_3$/water nanofluid concentration on a smooth horizontal and vertical stainless-steel plate. The particles used ranged in size from 10-100 nm in diameter with an average of 47 nm. It was noted that nanofluids had a lower heat transfer performance than water, and it worsened as the particle concentration increased. The CHF, however, was increased by 32% for horizontal and 13% for vertical pool boiling. The roughness of the surface was also shown to increase with nanoparticle concentration, as seen in Figure 6. The HTC was discovered to be lower than that of pure water.

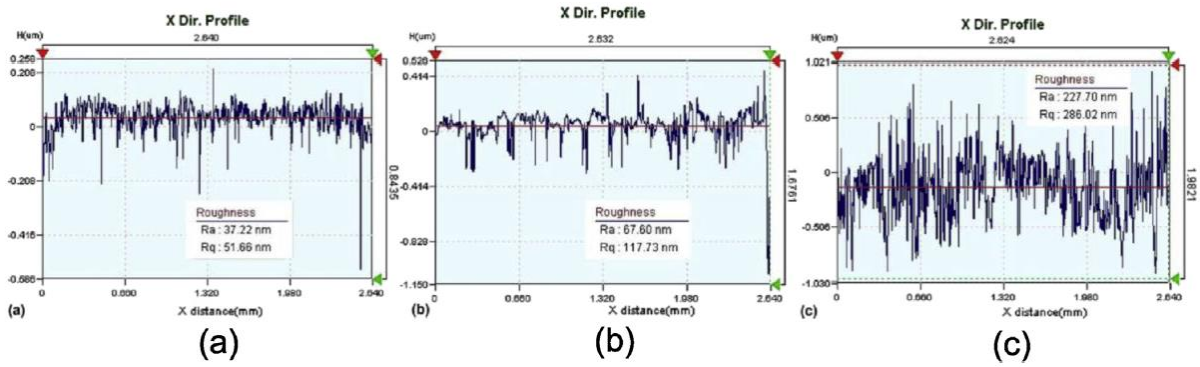


***Figure 6*** *Surface roughness (a) before test, (b) after test with 0.5% alumina and (c) 4% alumina.*

Chen *et al.* (2020) investigated the enhancement in pool boiling using interconnected microchannels with re-entrant cavities (IMRCs) to cool electronics with high power. Saturated and subcooled ($T_{sub}$= 20°C) water boiling was used at atmospheric pressure. They found that at both conditions, the re-entrant cavities and interconnected pores significantly enhanced the HTC up to 127% compared to smooth copper plates (SCPs) and up to 17% for interconnected microchannel net (IMNs), as shown in Figure 7. The IMRCs did not reach their CHF during the tests and achieved a heat flux of 1637 kW/m$^2$ at the maximum test range, which is already 36% higher than the CHF of SCPs. The IMRCs were said to have a high potential for high-powered electronics cooling in the industry.

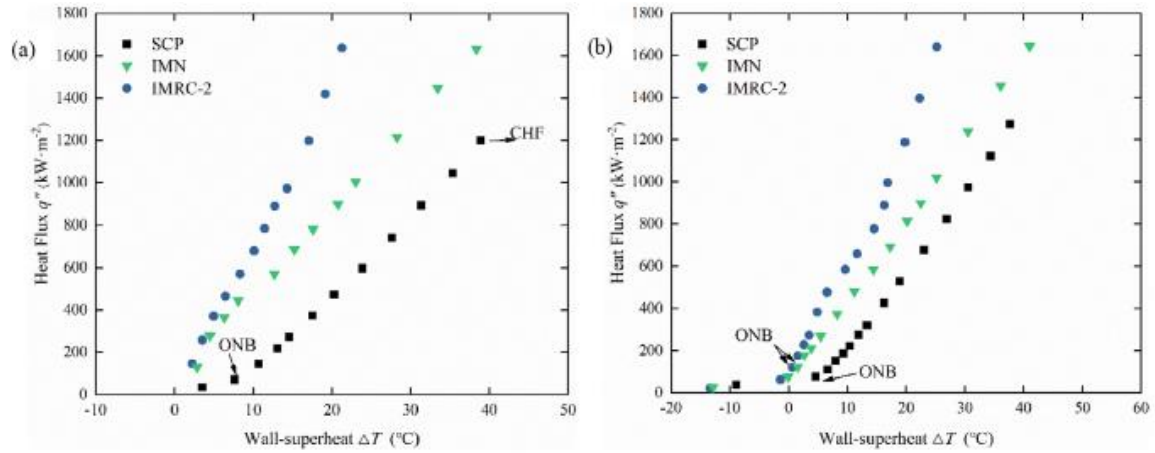


***Figure 7*** *Boiling curves for IMRC, IMN, and SCP in (a) Saturated boiling and (b) Subcooled boiling.*

Chopkar *et al.* (2008) examined the pool boiling heat transfer characteristics of $ZrO_2$/water with concentration varying from 0.005% to 0.15 vol% and a 20-25 nm particle size. A flat copper surface was used as a heater. They found that HTC enhancement was only seen at low particle concentrations and that any increase in

the concentration would decrease the HTC to a point where it was lower than that of pure water. This was because the surface roughness had been reduced. The authors also investigated the influence of surfactants and found that it increased the HTC in pure water, but when it was used with nanofluids, the HTC decreased significantly.

Coursey and Kim (2008) investigated surface wettability using $Al_2O_3$/water and $Al_2O_3$/ethanol of concentration from 0.026 g/L to 1.02 g/L and 0.001 g/L to 10 g/L, respectively, with a particle size of 45nm and used a copper block as the heater. They concluded that both the nanoparticle concentration and surface wettability significantly influenced the heat transfer performance. They observed that there was a degrading or no effect on the heat transfer capabilities of pool boiling at low concentrations, whereas concentrations greater than 0.05 wt% lead to a decent increase of about 37% in the CHF for $Al_2O_3$/water 25% for $Al_2O_3$/ethanol. They also concluded that adding nanoparticles in base fluid enhanced the surface wetting, which leads to an enhanced CHF only when particles covered the surface.

Das *et al.* (2008) concluded from their study that when the heater's surface roughness was around the same size as the nanoparticle diameter, the nucleation sites were decreased, leading to a deterioration in HTC. On the other hand, when the sizes were much different from each other, either an enhancement in HTC was observed due to the multiplication of nucleation sites, or a small deterioration was observed depending on the concentration.

Das and Putra (2003) used stainless steel (SS) cylindrical heater and reported that an increase in particle concentration for $Al_2O_3$/water decreased the HTC of the nanofluid. The cause for the decrease in HTC was reported to be the increased smoothness of the heater. They used concentrations from 0.1 to 4% vol and varied particle size from 20 to 50 nm.

Fan *et al.* (2020) studied the effect of surface roughness on the heat transfer capabilities of pool boiling by using different roughness values ranging from 0.045 µm to 1.35 µm. The experiment was carried out using water under atmospheric pressure and saturation temperature. It was concluded that the increase in surface roughness decreases bubble departure diameter, nucleation site density, and bubble departure frequency, which helps enhances HTC. They also mentioned that the nucleation site density increases with heat flux, which also enhances the HTC.

Feldmann and Luke (2008) conducted a pool boiling experiment for various base fluids at pressures and temperatures falling in the range from 0 to 50 bar and -50°C to 200°C, respectively, to understand the effect on surface tension. They reported that as the fluid pressure decreased, the surface tension increased. They also reported that the surface tension was halved by adding a surfactant. The bubble departure frequency and nucleation sites increase when the surface tension decreases and the bubble diameter decreases, which improves HTC.

Golubovic *et al.* (2009) conducted pool boiling experiments at atmospheric pressure and saturated temperature of 100°C using a horizontal NiCr wire heater. $Al_2O_3$/water and $BiO_2$/water nanofluids were used with a particle size of 22.6-46 nm and 38 nm, respectively, and concentrations from 0%-0.01 g/L. They found that with an increase in concentration, the contact angle decreased in which $Al_2O_3$/water showed a more significant decrease from 90° to as low as 33° compared to $BiO_2$/water, which decreased to as low as 56°. The authors suggested that the decrease in contact angle was the reason for the CHF increase. The particle size has a negligible effect on contact angle. The CHF increased with particle concentration until a certain point where any increase after that the CHF did not significantly change. $Al_2O_3$/water showed a maximum CHF increase of 50%, whereas $BiO_2$/water showed a CHF increment of up to 33%.

Gouda *et al.* (2018) conducted an experimental examination of the parameters of pool boiling heat transfer of copper microchannels with segmented fins (SF) and compared it to using uniform cross-section microchannel (UCS) and plane surface. SF and UCS surfaces are shown in Figure 8 where all surfaces were made from a copper block with the same footprint area. Water was used at saturation temperature and atmospheric pressure. They found that the SF surface has a contact angle of zero and better wettability characteristics and showed HTC values three times larger compared to the plane surface, whereas the UCS surface showed HTC values that were two times larger compared to the plane surface. In addition, the nucleation started earlier on the SF surface and had a higher nucleation density, better wetting, and better bubble growth and release mechanism than the other two surfaces.

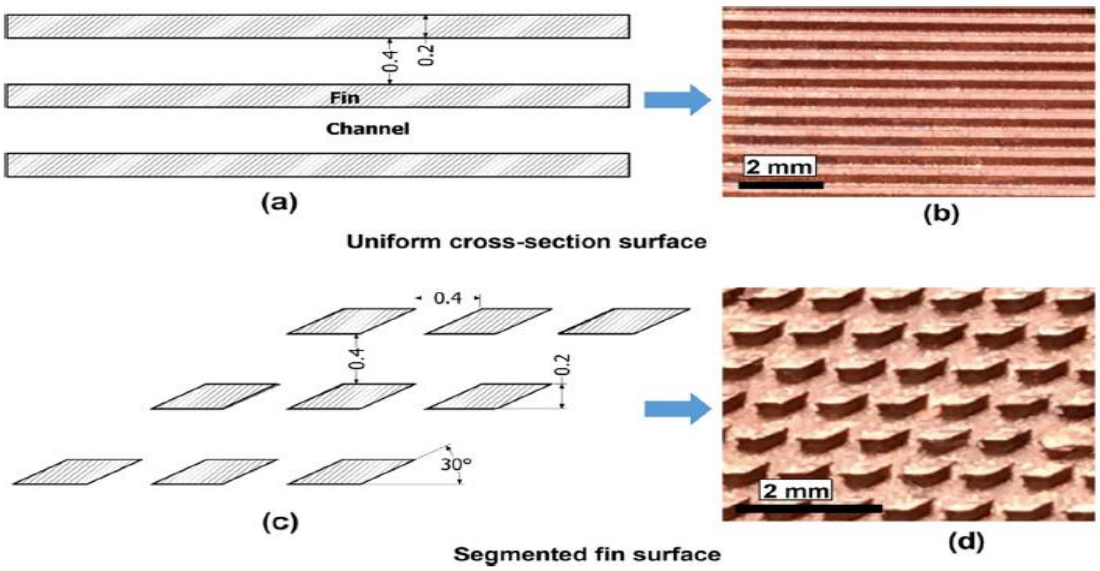


***Figure 8*** *Schematic and pictures of (a,b) UCS and (c,d) SF.*

Ham *et al.* (2017) experimentally investigated pool boiling characteristics of $Al_2O_3$/water nanofluid with 50 nm diameter size at different surface roughness (177.5 nm and 292 nm) and concentration (0-0.1% vol.). The saturation pressure was 3 kPa, and the heater was a copper bar. It was found that CHF increased up to 224.8% compared to water at low roughness, whereas it increased 138.5% for the high roughness. The nanoparticle deposition deteriorated the wettability, which caused the CHF to decrease. The contact angle decreased with an increase in concentration from 0 to 0.05 % vol and then increased until 0.1 % vol. at both roughness. It was concluded that HTC decreased with concentration due to increased deposition. It is worth noting that the surface with higher roughness showed a higher decrease in HTC. The authors mentioned that this was because the smoother surface's cavities had increased and were higher than the rougher surface.

Harish *et al.* (2011) performed an experimental investigation focused on the boiling heat transfer capabilities of $Al_2O_3$/water with 50 nm particle size and concentrations ranging from 0.5%-2% vol. to understand the effect of surface-particle interaction parameter (SPIP) which is a ratio calculated by dividing the heater surface roughness by the nanoparticle diameter. Two aluminium disks, one smooth and the other rough, were used. The roughness of the heater had been modified due to the nanoparticle deposition on the surface. The roughness was decided by the particle concentration and wall temperature that the heater was exposed to. For the smooth surface, an increase in concentration leads the wettability to decrease, whereas the wettability

increases for the rough surface. The HTC increased for the rough surface, whereas a maximum of 30% deterioration was seen for the smooth surface. They concluded that nanofluids' boiling characteristics depend on the surface roughness and particle size and their interactions that decide either plugging or splitting surface cavities. The SPIP is less than one if the surface cavity size is smaller than the nanoparticle diameter and greater than 1 if the cavity size is larger.

He *et al.* (2016) looked into the boiling heat transfer of ZnO/EG/water (95:5, 85:15, and 75:25 vol) at different particle concentrations from 5.25%-8.25% vol and used a Ni-Cr wire as the heater. They observed a generous improvement in CHF compared to each base fluid, while the HTC could only be improved when the concentration was less than 7.25% vol. The nanofluid HTC below this concentration was higher than base fluids and increased with a decrease in concentration. They mentioned that this improvement was due to particle deposition and a decrease in wettability.

Heris (2011) studied CuO/EG/water (60/40) at different low concentrations from 0.1% to 0.5% vol, saturation temperature, and atmospheric pressure. The author used a cylindrical cartridge heater and a particle size of 40nm. It was observed that the HTC increased significantly (up to 55%) when nanofluid was used, and the enhancement was more significant when the concentration was increased, as shown in Figure 9 and Figure 10. It was pointed out that since the size of the surface cavities was larger than the nanoparticles, the nanoparticles may deposit on the nucleation site and split the single site to increase nucleation sites.

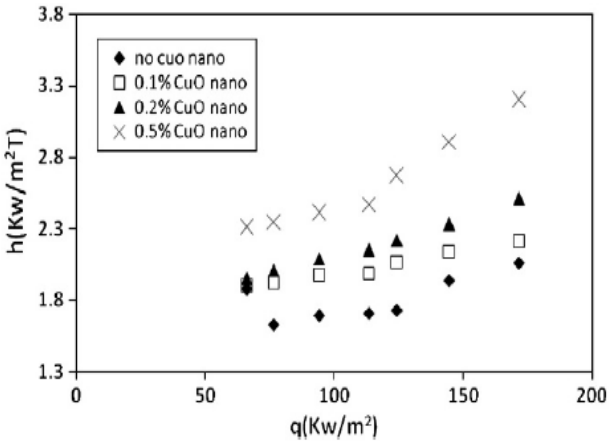


***Figure 9*** *HTC vs heat flux at different concentrations.*

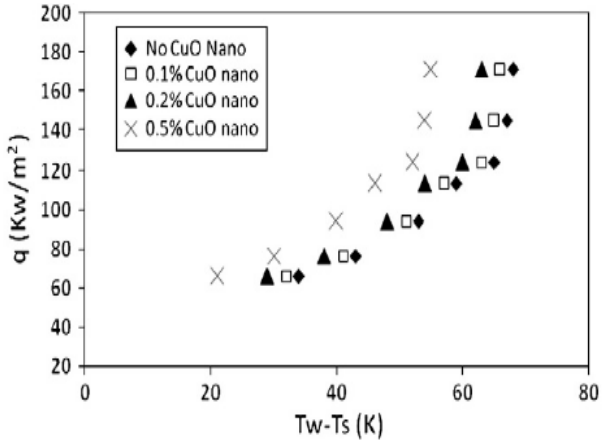


***Figure 10*** *HTC vs superheat at different concentrations.*

Huang *et al.* (2011) used $TiO_2$/water with particle size ranging from 110 to 220 nm with concentrations of 0.01%-1 wt% to study the effect on CHF at atmospheric pressure and saturation temperature using a nickel wire. They reported CHF enhancement of up to 83% and HTC deterioration when the nickel wire heater was coated in the nanoparticle layer. The contact angle, which decreased as the heat flux and particle concentration increased, was speculated to be the reason for increased surface wettability, which enhanced CHF. They mentioned that the effect of nanoparticles was due to the coating it creates and not the dispersion in the base fluid.

Jones *et al.* (2009) investigated how the nucleate pool boiling heat transfer depends on surface roughness. They experimented with two different fluids: FC-77 and water, which have different thermal properties and wetting characteristics. The experiment involved various surfaces from polished surfaces (average roughness of 0.027 µm to 0.038 µm) to surfaces that were electrical discharge machined (EDM) with an average surface roughness varying from 1.08 µm to 10 µm. They concluded that the two fluids demonstrated different trends with regards to HTC. While using the FC-77, the HTC continuously increased with surface roughness up to 210% compared to the polished surface. However, for water, surfaces with intermediate roughness had similar HTC, which was still higher than the smooth surface, and the roughest surface showed the highest HTC, which was 100% higher than the smooth surface, as shown in Figure 11.

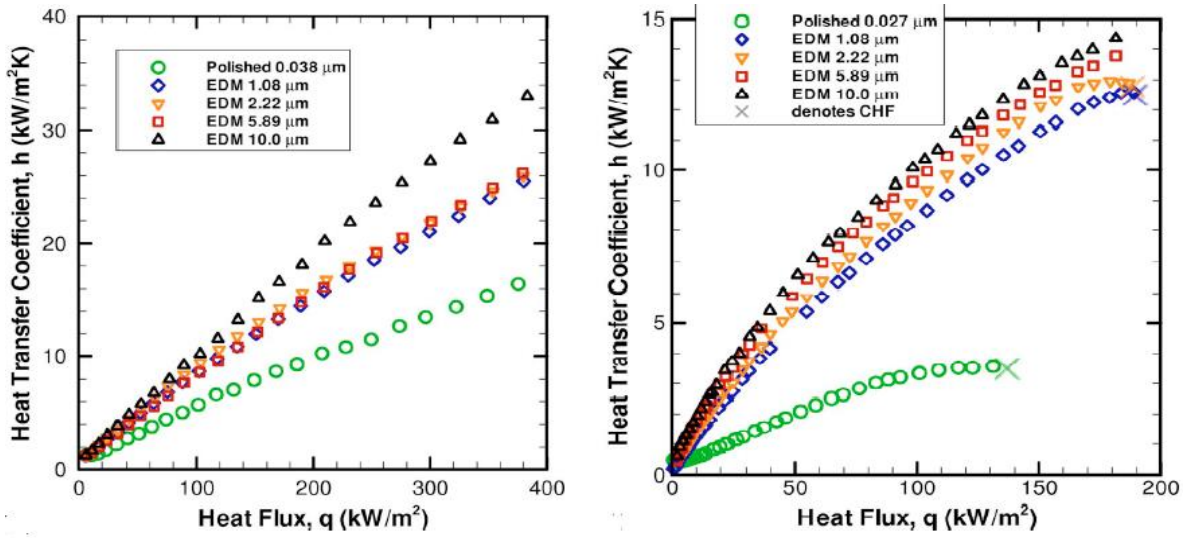


***Figure 11*** *HTC vs heat flux graph for water (left) and FC-77 (right) with different surface roughness.*

Kamel and Lezsovits (2020) studied the pool boiling heat transfer enhancement using $CeO_2$/water at varying concentrations of 0.001% to 0.04% vol with a particle size of 50 nm at atmospheric pressure and saturation temperature. A horizontal copper tube with a roughness of 115 nm was used. They reported that the HTC was up to 1.7 times higher for the nanofluids than pure water at 0.007% vol. It was mentioned that this enhancement was due to surface and bulk modifications due to nanofluids' use. They showed that increased surface roughness and thermal conductivity enhanced the boiling performance at dilute concentrations. The contact angle of pure water had decreased after the surface was coated in the nanoparticle layer compared to the original state. The surface roughness increases with concentration up to a point and then stays constant.

Kathiravan *et al.* (2009) studied the effect of adding 9 wt% surfactant on the heat transfer abilities of Cu/water during pool boiling with a particle size of 10nm and concentrations from 0.25% to 1 wt%. A horizontal stainless-steel tube heater with a 9 mm diameter was used as the heater with a surface roughness of 1.09 µm. They found that the nanofluids degrade the HTC with and without surfactants. As the concentration increases, the HTC decreases, while when a surfactant was added to water only, the HTC increases by 30% because of a reduction in surface tension. However, the CHF increases with concentration up to 49% higher than pure water when only nanofluids were used. The CHF increase was up to 59% when a surfactant was added, and the HTC was enhanced. They found that the heater's surface roughness had increased and that the CHF improvement was because of the deposition of nanoparticles on the heated surface.

Kathiravan *et al.* (2010) looked into the pool boiling characteristics of Cu/water nanofluid with 10nm particle size over a flat stainless-steel plate heater with a roughness of 167 nm to understand the effect of surfactant and particle concentration on the CHF. Concentrations of 0.25% to 1 wt% were used with and without 9 wt% surfactants under atmospheric pressure and saturation temperature. The results show that pure water has 80% higher CHF than pure water with surfactant. The CHF for the nanofluids without surfactant increased up to 48% with an increase in concentration and claimed that the deposition of naoparticles on the heated surface caused this increase. When a surfactant was used with nanofluid, the CHF increases up to 75%

but decreases with concentration. The roughness of the heater surface had decreased at the end the boiling experiment.

Khooshehchin *et al.* (2020) researched on pool boiling heat transfer optimization using ultrasonic waves irradiation (24 kHz) and the addition of CuO. They considered different particle sizes (20 to 60 nm), concentrations (0.025% to 0.125 wt%), heater tilt angle (up to 30°), and irradiation time (up to 21 min). A copper cylinder with a surface roughness of 840 nm was used as a heater. They found that as the inclination angle increased, the nucleation site density and the frequency of bubble production also increased, decreasing the departure diameter. However, HTC was highest at a tilt angle of 15° with a mean increase of 18.9%, whereas the angle of 30° had a mean increase of 3.1% compared to 0° (horizontal). They found a significant increase in HTC when nanoparticles were added. The HTC increased with a decrease in particle size. The nanoparticles increased the thermal conductivity of the fluid. Smaller the particle size and higher the concentration, the higher the thermal conductivity was. Their results showed that HTC increased with concentration. Waves with 60% of the device power (1.2 kW) had the highest HTC at high heat fluxes, while waves with 90% had the highest HTC at lower fluxes. It was found that the highest HTC enhancement was seen at 14 min duration of ultrasonic waves followed by 21 min and lastly 7 min. The ultrasonic waves also decreased particle deposition.

Kim (2014) carried out an experiment to understand the effect of surface roughness (0.22 μm to 2.32 μm) on pool boiling heat transfer in subcooled CuO/water with a concentration of 0.1% vol. and a particle size of 80 nm. A copper block was used as the heating surface. It was discovered that increasing the roughness had increased the boiling heat flux and thus the HTC for pure water. However, it was unclear what the effect of surface roughness was when nanofluid was used since the particle deposition on the heater surface had reduced the differences in surface roughness. It was noticed that the contact angle increased with roughness for both pure water and nanofluid. From the plots, it was noticed that the nanofluid had lower HTC compared to water.

Kim *et al.* (2007) investigated the surface wettability and CHF using $SiO_2$/water, $ZrO_2$/water, and $Al_2O_3$/water nanofluids while varying concentration from 0.001% to 0.1%vol. and particle sizes from 20-40 nm, 110-250 nm and 110-210 nm, respectively. A stainless-steel wire heater was used to boil a fluid under atmospheric pressure and at saturation temperature. It was discovered that the heater surface roughness increases about 20 times, which results in an area increment of up to 5 times the original area. Therefore, the contact angle decreases, which increases CHF and decreases HTC by forming a resistance. The CHF was enhanced using all nanofluids and up to 80% for $SiO_2$/water.

Kim *et al.* (2016) studied the effect of surface roughness on the pool boiling HTC and the CHF. They used saturated water as the working fluid and copper surfaces with various roughness values ranging from 0.041 µm to 2.36 µm. They found that the CHF increases almost by a factor of 2 at 2.36 µm as compared to when the surface roughness of 0.041 µm was used and mentioned that this enhancement was due to improved capillary wicking from surrounding liquid to the dry regions of the heater. The increase in surface roughness also increased the boiling HTC, as suggested in Figure 12, where the higher CHF can also be noted. They observed that the contact angle, as viewed in a parallel direction to the scratches, increased with roughness, whereas the contact angle, as viewed from the normal direction of the scratches, decreased. They also mentioned that their results agreed with the coefficient $C_{sf}$ that was used in the correlation of Rohsenow.

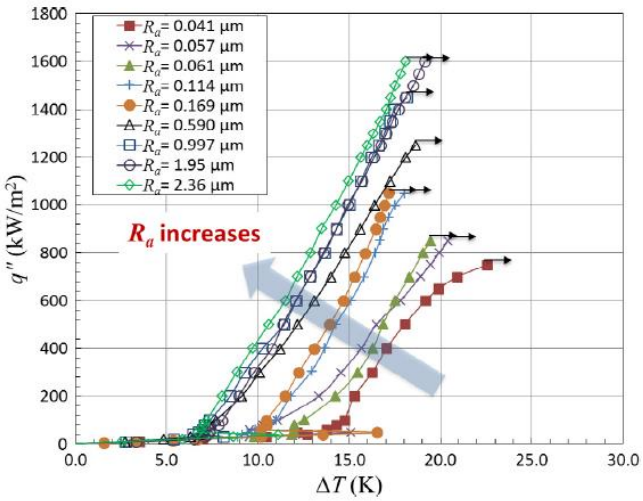


***Figure 12*** *Boiling curve at different surface roughness.*

Kim *et al.* (2006) investigated the effect of $Al_2O_3$/water and $TiO_2$/water on CHF enhancement in saturated boiling at 100°C by using thin heated NiCr and Ti wires and particle concentrations from 0.00001% to 0.1%vol. The $Al_2O_3$particles had a diameter of 47 nm, whereas $TiO_2$ particles were 85 nm in size. The CHF of $Al_2O_3$/water nanofluid increased up to 176% compared to base fluid and up to 200% for $TiO_2$/water nanofluid. They found that the improvement in CHF during nanofluid pool boiling was primarily due to the change of heater surface topography and microstructure caused by nanoparticle surface coating.

Kim *et al.* (2020) studied the pool boiling heat transfer using the microporous and bare copper plate in a confined space (gap) using pure saturated water at 1atm. The copper plate heater was oriented vertically. The length of the gap was varied from 0.5 mm to infinite (unconfined). For unconfined space, they reported typical pool boiling. As the gap length decreases for the bare surface, the HTC increased except for the gap length of 0.5 mm, where the HTC decreased compared to the 1 mm gap. The HTC for the microporous surface was independent of the gap length. They also noted that the HTC and CHF were much higher for microporous surfaces at unconfined spaces than bare surfaces. For both surfaces, the CHF decreased with a decrease in gap length.

Kshirsagar and Shrivastava (2018) looked into the pool boiling performance of $Al_2O_3$/water with concentrations varying from 0.3 %wt to 1.5 %wt and with an average particle size of 30 nm. They used a Ni-Cr wire with a roughness of 111 nm as the heating element. The CHF increased by 87%, and the HTC was also improved as compared to the base fluid. It was found that the surface roughness increased with concentration until 1.2 %wt after which it decreased. The HTC followed the same pattern as the surface roughness, where it increased up to 1.2 %wt and decreased again from this point onwards. The decrease in roughness was due to nanoparticles filling the microcavities formed over the heater surface.

Kwark *et al.* (2010) studied the pool boiling characteristics of Cu/water, $Al_2O_3$/water, and diamond/water with a particle size of 143 nm, 139 nm, and 86 nm, respectively with different low concentrations less than 1g/L using a plate copper heater at a pressure of 1 atm. They investigated the cause of nanoparticle layer coating formation along the heater surface and discovered that a thin nanoparticle layer forms on the heater's surface, which increases wetting and causes the increase of CHF. The

evaporation of the microlayer during boiling was the reason for the formation of a nanoparticle layer on the heater. They also found that as the particle concentration increased, the CHF increases up to 80% compared to pure water for all 3 nanofluids. Their results show that the thickness of the nanoparticle layer formed on the heater surface increases with boiling time, which causes a degradation in HTC by increasing thermal resistance. The CHF increased with the layer thickness up to a point beyond which no further CHF improvement was seen. No HTC degradation was seen for low concentrations (0.025g/l), but the HTC decreases with nanoparticle layer thickness at higher concentrations. The nanoparticle type was said to have a negligible effect on the nanofluid boiling.

Li *et al.* (2020) carried out a saturated pool boiling experiment using CuO/water with varying concentrations from 0.025% to 0.1 wt% and particle size of 45 nm on finned copper surfaces with different space between two fins, width, and height. They found that the surface with the smallest fins and highest space between fins had the smallest HTC, while the surface with the biggest fins and lowest space between fins had the highest HTC. The surface with greater space between the fins was observed to have larger bubbles, resulting in a poorer HTC. They concluded that the fins prevent fouling from forming on the surface, which leads to the enhancement of the HTC.

Liu *et al.* (2007) carried out nucleate boiling experiments using CuO/water nanofluid at different pressures from 7.4 to 100 kPa and varying concentrations from 0.1 wt% to 2 wt% with 30 nm diameter on a heated copper surface with micro grooves and without (smooth). It was found that the surface with microgrooves enhanced the heat transfer capabilities at atmospheric pressure while it had no effect at low pressures. At all test pressures, the HTC and CHF increased gradually as the concentration increased to 1.0 wt%, which was optimal. Any increase from this optimal concentration showed a decrease in HTC. Their results showed that increasing the pressure up to atmospheric resulted in higher HTC and CHF. They also concluded that the lower the pressure, the more significant the HTC and CHF enhancement was when nanoparticles were added.

Manetti *et al.* (2016) investigated the effect of surface roughness on the heat transfer performance of nanofluid pool boiling. They used a copper cylinder with different degrees of nanoparticle deposition to achieve different surface roughness. The experiment was conducted using $Al_2O_3$/water and $Fe_2O_3$/water with concentrations

varying from 0.029 g/L to 0.29 g/L, each with a particle of 10 nm. They observed that the nanoparticle deposition increased with heat flux, which increased the surface roughness and changed the surface wettability. It was concluded that the nanofluids decreased the contact angle and even more on nanocoated surfaces. The surface roughness, deposition thickness, and wettability increased with concentration. Independent of the surface roughness, HTC deterioration was observed at high concentrations because of increased deposition thickness, which increased the surface's thermal resistance.

Narayan *et al.* (2007) investigated the enhancement/deterioration of pool boiling heat transfer using alumina particles (47 and 150 nm) over vertical stainless-steel tubes with various surface roughness of 48, 98, and 524 nm and concentrations of 0.5-2 wt%. They noted that at a roughness of 524 nm (rough), the HTC increased up to 70%, whereas for the smooth surface with a roughness of 48 nm, the HTC deteriorated by 45% compared to base fluid (water). They observed that the ratio between the surface roughness and particle size could explain the differences in HTC outcomes. There was a decrease in the nucleation site density when surface roughness and the particle size were of the same order. When the roughness was significantly larger than the particle size, nucleation sites significantly increased. When the roughness was much smaller than the particle size, the performance is still better than when the ratio is near unity. This was because fewer nucleation sites were being clogged. Figure 13 shows the effect of this surface-particle interaction parameter (SPIP) on heat transfer improvements. They also noted that the HTC decreases as the concentration increases.

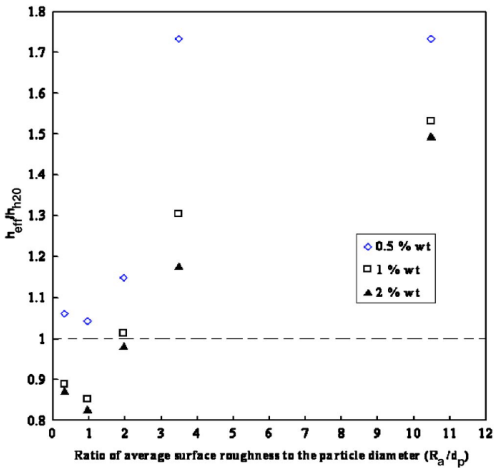


***Figure 13*** *Effect of SPIP on the HTC ratio.*

Nazari and Saedodin (2018) conducted a pool boiling experiment using an aluminium heated surface and $Al_2O_3$/water with varying concentration up to 0.1% vol and particle size of 47 nm at atmospheric pressure of 86 kPa and at saturation temperature to investigate the effect on the contact angle, CHF and surface roughness. They found that particle deposition changes the chemistry and morphological characteristics, such as the surface's wettability and roughness, affecting boiling characteristics. The deposition thickness and roughness increase with concentration. The wettability increased with deposition thickness and enhanced the CHF. They concluded that low concentrations have a negligible effect on CHF, whereas, for concentrations around 0.01% vol, CHF was improved up to 19 %, as depicted in Figure 14. The authors also reported that the contact angle decreases with an increase in concentration, as shown in Figure 15, which also enhances CHF. The HTC decreased due to surface deposition.

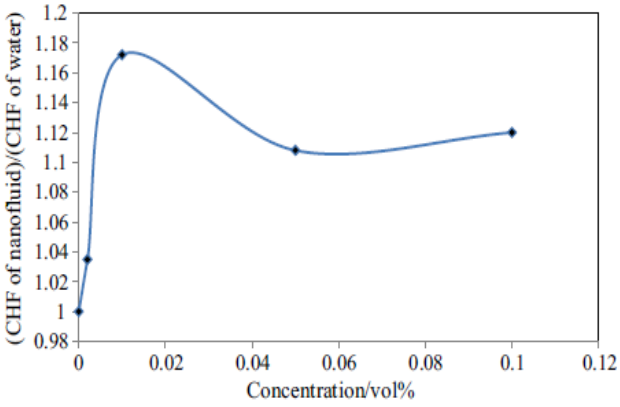


***Figure 14*** *CHF improvement vs concentration.*

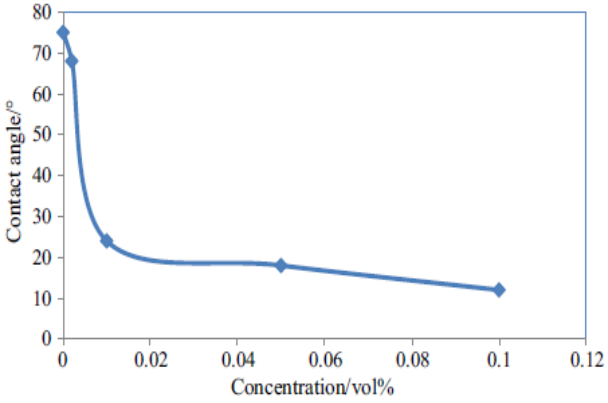


***Figure 15*** *Contact angle vs concentration.*

Ogbonnaya *et al.* (2019) reviewed how nanoparticle deposition affects the pool boiling heat transfer capabilities and the effect of deposition on the roughness of the surface. It was noted in their article that the initial surface roughness and nanoparticle deposition have an impact on the heat transfer during pool boiling. The size of the nanoparticle in relation to the original surface conditions determines whether the surface roughness increases or decreases. As the nanoparticles deposit on the surface pores, the surface roughness rises if the original surface roughness is smaller than the nanoparticle and decreases if the nanoparticle size is less than the initial surface roughness.

Okawa *et al.* (2012) experimented to understand the dependence of CHF, contact angle, and HTC on the boiling time of nanofluid pool boiling using $TiO_2$/water using varying concentrations from 0.000094% to 0.047% vol under saturation temperature and atmospheric pressure with a particle size of 21 nm. The heated surface was a copper block. They found that the CHF increased, and the contact angle decreased with time up to a point from which there was no further change for both. The CHF increased up to 91% and reported that this increase was due to modification of heater surface caused by nanoparticle layer. The time taken to reach maximum CHF decreases dramatically with increased concentration, taking 60 min for low and 1 min for high concentrations. At high concentrations, the HTC first decreases then increase gradually to a nearly constant value, greater than that of pure water, whereas, at low concentrations, no noticeable change was seen. The increase in HTC was due to the deposition, which created new nucleation sites.

Park *et al.* (2009) focused on nucleate pool boiling heat transfer of carbon nanotube (CNT)/water with varying concentrations from 0.0001% to 0.05% vol and CNT diameter of 10-20 nm. The heater used was a flat and smooth copper block. They reported that the CNT nanofluids had a lower HTC than pure water, but the CHF increased up to 200% at a concentration of 0.001% vol. A CNT layer formed on the heater surface, which increased thermal resistance and decreased nucleation sites and caused the HTC deterioration since bubble generation was decreased. The layer leads to a lower contact angle which dramatically increases the CHF.

Pham *et al.* (2012) investigated the pool boiling CHF of 0.05% $Al_2O_3$/water, 0.05% CNT/water with 10% boric acid, and 0.05% $Al_2O_3$ + 0.05% CNT both mixed in water under atmospheric pressure and 7 °C – 14 °C subcool. The heated surface was a stainless-steel plate used at different angles. They found that all nanofluids showed an enhancement in CHF when compared to pure water and that as the inclination angle increased, the CHF increased up to 122% for $Al_2O_3$/CNT/water nanofluid, followed by 108% for CNT/water and 33% for $Al_2O_3$/water. The highest decrease in contact angle was for $Al_2O_3$/water, followed by $Al_2O_3$/CNT/water. They also found that the surface roughness had increased and that the higher surface roughness leads to higher CHF. CNT/water did not form a layer but had a CHF higher than that of $Al_2O_3$/water, which did form a layer. Therefore, researchers concluded that the CHF

enhancement could not be explained only by looking at nanoparticle layer formation on the heater surface. No conclusion was drawn on the HTC.

Rejvani *et al.* (2019) investigated the heat transfer efficiency and optimal characteristics of $SiO_2$/water at concentrations from 0 to 1.5% vol. The particle used were spherical with a size of 20-30 nm. They concluded that for pipe flow, nanofluid was not recommended for both laminar and turbulent flows except when the temperature was higher than 30 °C, and concentration was lower than 1%. This was because the heat transfer enhancement due to an increase in thermal conductivity outweighs the unfavourable increase in pumping power at these conditions. Outside of the mentioned conditions, the increase in viscosity increases the pumping power and was not worth the increase in thermal conductivity. They also mentioned that the highest increase in thermal conductivity was seen at 35-40 °C.

Rostami *et al.* (2020) investigated the effect of magnetic fields on the HTC during boiling using NiO/water with concentrations of 0.005%-0.2% vol and particle size of 10-60 nm. They used a vertical copper cylinder as the heater. It was found that with no magnetic field, the HTC was enhanced only at 0.005% vol. concentration as compared to water and deteriorates with an increase in concentration. They also found that the magnetic field enhanced the HTC at 0.005% vol., but high magnetic field intensities deteriorated the HTC at high concentrations. A maximum HTC enhancement of 56.4% was noted when a magnetic field of 300 gauss was used with 0.005% vol. concentration as compared to water.

Sarafraz and Hormozi (2016) used aqueous multi-walled carbon nanotube nanofluid with concentrations of 0.1%-0.3 wt% and diameter of 10-20 nm to investigate its pool boiling heat transfer performance. A micro-finned and plain surface were considered. They found that modified surface enhanced the HTC and CHF by up to 77% and 95%, respectively, at 0.3 %wt compared to plain surface heaters. The modified surfaces hindered particle deposition and vapour layer formation, which increased its heat transfer capabilities.

Sheikhbahai *et al.* (2012) investigated pool boiling of $Fe_3O_4$/EG/water (50% vol. EG/50% vol. water) in an electric field with particle concentrations of 0.01%-0.1% vol., particle size smaller than 50 nm, atmospheric pressure, and saturated temperature were used. A horizontal NiCr wire was used as the heater. They found that the HTC

decreases, and CHF increases with particle concentration where the maximum CHF increment was near 100%. The researchers mentioned that CHF's increase was due to a porous layer that modified the heater surface and increased the wettability by decreasing the contact angle from 60° to 20°. Increased wettability delays the vapour film blanket and causes an increase in CHF. CHF enhancement was also seen when the heater wire previously used in nanofluid boiling was used to boil the pure base fluid. By applying an electric field, the HTC had increased in comparison to boiling without an electric field, whereas the CHF did not show any change.

Shoghl and Bahrami (2013) experimented using a stainless-steel rod heater to compare nanofluids' boiling performance at saturation temperature and atmospheric pressure with and without surfactant using ZnO/water and CuO/water at concentrations from 0.01% to 0.02 wt% of nanoparticle and 0.04 wt% surfactant. They showed that for pure water, as the surfactant concentration increased up to 0.02 wt%, the HTC increased. Using surfactants with a concentration higher than 0.02 wt% lead to bubble film formation on the heater surface, which reduced the HTC. When nanofluids were used without surfactant, the boiling performance decreased. This was because the heater's surface roughness decreased, which initially had a surface roughness greater than the nanoparticles' size. When surfactant was used with nanofluid, the HTC had improved. Maximum HTC was noted for 0.01 wt% CuO/water with 0.02 wt% surfactant.

Soltani *et al.* (2009) used a vertical stainless-steel cartridge heater to carry out experimental measurements on the boiling heat transfer characteristics of $SnO_2$/water and γ-$Al_2O_3$/water of varying concentrations from 0.5% to 3 wt% and 0.3% to 2 wt% with a particle size of 55 nm and 20-30 nm, respectively at atmospheric pressure. Their results show that HTC increases with an increase in particle concentration for γ-$Al_2O_3$/water up to 30% compared to the base fluid. For $SnO_2$/water, the HTC was lower than that of pure water at low concentration, while using concentration higher than 0.5 wt% shows a steady increase and enhancement of HTC up to 20%. It was concluded that the physical properties of the nanoparticles could be the cause of this contradiction.

Suriyawong and Wongwises (2010) experimented on pool boiling of $TiO_2$/water with particle diameter of 21 nm at various low concentrations from 0.00005%-0.01% vol. at

atmospheric pressure and saturation temperature. Horizontal copper and aluminium plates, each with a roughness of 0.2 µm and 4 µm, were used. For copper surface, the nanofluid concentration of 0.0001% vol. showed an increase in HTC compared to base fluid with an average increase of 15% with a roughness of 0.2µm and 4% with a surface roughness of 4µm. Conversely, higher concentrations showed a decrease in HTC. The HTC was always lower than pure water for aluminium surfaces in all conditions. However, the HTC, while using aluminium surface with water, was higher than when using a copper surface with water. The HTC was also generally higher for the roughness of 4 µm than 0.2 µm due to increased cavities and nucleation sites.

Trisaksri and Wongwises (2009) used $TiO_2$/R141b nanofluid with a particle size of 21 nm to examine the nucleate pool boiling heat transfer at different concentrations ranging from 0.01% to 0.05% vol., operating pressures of 400 kPa and 500 kPa and at respective saturated temperatures. A horizontal copper tube was used as the heated surface with a roughness of 314 nm. The HTC achieved while using nanofluid was always found to be lower than when base fluid was used, and as the $TiO_2$ concentration increased, the HTC decreased. In addition, they noted that HTC of pure R141b and the nanofluid increased with pressure and that effect of pressure on HTC was less at higher concentrations than at lower concentrations.

Vassallo *et al.* (2004) conducted a pool boiling heat transfer experiment using $SiO_2$/water and a horizontal NiCr heater wire with 0.4 mm diameter at atmospheric pressure and saturation temperature. Different particle sizes (15 nm, 50 nm, 3000 nm) were tested and used a fixed concentration of 0.5% vol. They noted that when using 15 nm and 50 nm particles, the wire failed to transition into film boiling and that using 50 nm particles achieved the highest heat flux, which was 3 times higher than pure water. They noted a nanoparticle layer formed on the heater surface, explaining the increase in maximum heat flux. They repeated the experiment on pure water using a rougher heater surface and found that the maximum heat flux had increased compared to the smoother surface in pure water. No visible HTC improvement was seen for any case.

Wen and Ding (2005) examined the pool boiling heat transfer of $\gamma$-$Al_2O_3$/water using a particle concentration of 1.25 wt% and particle size of 10-50 nm at atmospheric pressure and saturation temperature. The heater was a stainless-steel disk. They

concluded that the HTC increases with concentration up to 40%. However, the researchers did not report any deposition. They mentioned that controversies in heat transfer behaviour during pool boiling must be related to the behaviour and properties of the boiling surface, nanofluid, and their interactions.

Wen *et al.* (2011) investigated the effect of surface roughness on heat transfer of boiling nanofluids using $Al_2O_3$ particles with a 20-150 nm diameter and concentrations varying from 0.001%-0.1% vol. under saturation temperature and atmospheric pressure. Two brass plate heaters were used with a surface roughness of 420 nm (rough) and 25 nm (smooth). They mentioned that the boiling heat transfer depends on the relative size between the heater surface geometry and the particle suspended in the fluid and their interactions. The nanoparticle coating increased the surface roughness for the smooth surface, and the 200% HTC enhancement was reduced with concentration. In contrast, the surface roughness remained almost unchanged for the rough surface, and the concentration did not affect the boiling curve, which suggests that the modification of the heater surface was responsible for any enhancement or deterioration. They mention that the results were affected by the number of times the boiling surface was used in nanofluid boiling.

White *et al.* (2010) carried out experiments to understand the effect of nanoparticle layering on heat transfer during pool boiling. They used ZnO/water nanofluid with a particle size of 40 nm (2.3 vol%) and a horizontal stainless-steel plate as the heater surface. They found that with every test, the surface roughness of the heater increased. After each test with nanofluid, they used the same surface (uncleaned) and tested using pure water. It was found that the HTC increased significantly with every test using pure water after it was used with nanofluid due to increased surface roughness. For nanofluid, however, the HTC was enhanced in the first test (compared to base fluid) then decreases continuously after the first test when the surface was fully covered with a nanoparticle layer. This was said to be because the nanoparticle layer suppressed the transport of bubbles.

Witharana (2003) investigated the effect of heater surface roughness on the HTC of R-134a boiling at pressures varying from 3 to 5 bar using a wire heater. The results showed that the HTC increased with surface roughness and pressure up to 50% compared to a smooth surface.

Witharana (2003) also investigated boiling heat transfer using a copper plate as the heat transfer surface with a diameter of 100 mm. Au/water (0.0002 to 0.001 wt%) with particles size of 30 nm and ethylene glycol (EG)/water mixture was used with $SiO_2$ nanoparticles at 0.025 wt%. A higher concentration of Au particles showed a higher HTC of up to 21% than base fluid, whereas the HTC decreased for the $SiO_2$/water and $SiO_2$/EG nanofluid.

Yang and Liu (2011) studied pool boiling heat transfer at and below atmospheric pressure of traditional and functionalized $SiO_2$/water nanofluid, which, unlike traditional nanofluids, does not form a deposition layer on the heated surface or change surface characteristics. For this reason, there exists a comparable difference between them. The experiment consisted of a copper bar heater, a particle size of 30 nm, and concentrations of 0.5-2.5 wt%. They mentioned that functionalized nanofluid could increase the HTC to a small extent up to 27.3% compared to base fluid while not affecting CHF. In contrast, traditional nanofluid enhances CHF and deteriorates HTC. They found that the HTC for functionalized nanofluid was not very sensitive to pressure by showing that the HTC decreased by only 10% when the pressure was decreased from 103 kPa to 7.4 kPa. It was reported that functionalized nanoparticles can stay well dispersed after the nanofluid has been sitting still for 12 months, even at concentrations of 10 wt% without forming sediments.

Yang and Maa (1984) conducted saturated boiling experiments using a stainless-steel tube at room temperature and pressure. They found that heat transfer in pool boiling was enhanced using fluids with 0.05 µm to 1 µm alumina particles at a low concentration from 0.1-0.5 wt%. They noticed that the smaller particles and higher concentrations were better at enhancing the nucleate boiling heat transfer.

Yao *et al.* (2018) studied the influence of nanoparticle type and diameter on boiling heat transfer performance under various pressures. They used a smooth copper plate as the heater and boiled $SiO_2$/water, $Al_2O_3$/water, and $Al_2O_3$/$SiO_2$/water, each with a 0.01 wt% and two different average particle sizes of 50 and 30 nm. At a pressure of 101 kPa and while using a particle size of 50 nm, the $Al_2O_3$/water nanofluid showed the greatest improvement in HTC (up to 51.8%) compared to base fluid, followed by $Al_2O_3$/$SiO_2$/water (32.6%) and lastly $SiO_2$/water (18.3%). They also showed that for their experiment, the enhancement in HTC was higher when 50 nm particles were

used compared to 30 nm particles. They reasoned that the smaller particles have a higher collision frequency and thus a higher tendency of agglomeration at the same mass concentration.

You *et al.* (2003) investigated the pool boiling heat transfer on a copper plate heater using $Al_2O_3$/water. The concentration ranged from 0 g/L to 0.05 g/L at saturation temperature of 60°C. The authors reported a 200% increase in the CHF than using base fluid, whereas the HTC during nucleate boiling remained unchanged.

To summarise, the literature suggests that the improvement in heat transfer using nanofluids depends on different factors such as the shape, surface roughness, finishing, and the heater's material. It was also worth noting that $Al_2O_3$/water was the most used nanofluid in the literature and are predominantly found in spherical shapes although short rod shapes are also common as shown below. The shape of the nanoparticles do play a small role in the thermal conductivity of the nanofluid as mentioned by Alawi *et al. (2018)* but correlations that take into account the shape of the nanofluid are difficult to find. A general trend can be formed from the outcomes reported by different articles.

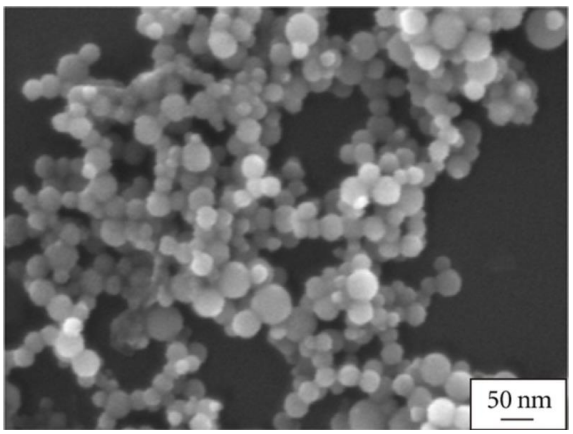


***Figure 16*** *Appearance of spherical shaped Al2O3 nanoparticles under microscope.*

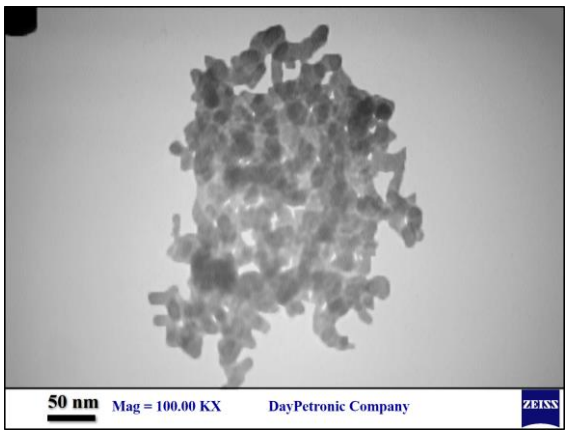


***Figure 17*** *Appearance of rod shaped Al2O3 nanoparticles under microscope.*

The heating surface's topography and microstructure get affected during nanofluid boiling, which significantly helps with CHF enhancement. In addition, deposition of the nanoparticle layer on the heating surface enhances its characteristics such as roughness and surface wettability, which dramatically improves the CHF.

The HTC was enhanced when the nanofluid's thermal conductivity increases since the heat transfer increases. The use of surfactants improves suspended particles' stability,

decreasing the agglomeration and deposition, which increases the HTC. Surfactants also help increase HTC by reducing the surface tension between the heating surface and the nanofluid, which increases the nucleation sites and decreases bubble diameter. As the fluid becomes more turbulent, the HTC increases as heat transfer by convection increases.

Depending on the concentration and boiling time, nanoparticles tend to accumulate on the test surface. The thin nanoparticle layer on the heating surface leads to an enhanced HTC at low concentrations as the thermal conductivity effect dominates the thermal blanketing effect of the nanoparticle layer, and the surface roughness increases. However, at high concentrations, nanoparticle deposition increases. As a result, the number of nucleation sites and bubble diameter is reduced, and additional thermal resistance is formed, leading to a deterioration of HTC. Depending on the original surface roughness and nanoparticle size, the nanoparticle layer can either increase or decrease the surface roughness. There is an increase in the surface roughness if the nanoparticle is larger than the surface roughness and decrease if it is smaller than the surface roughness. As the saturation pressure increases, the HTC enhancement increases and that smaller particle sizes are better at enhancing heat transfer than larger particles in general.

Following the evaporation of the microlayer, nanoparticles are deposited on the heated surface. If the particles deposit on cavities that are smaller than the particle size, the cavities are blocked and unable to form bubbles. In contrast, when the particle size is smaller than the cavities, the nucleation site is split, which promotes heat transfer. From Table 2, most of the authors reported the surface roughness to decrease when SPIP >> 1 and increase when SPIP is close to 1. However, Figure 13 suggests that HTC is improved when SPIP >> 1. This would mean that even though the surface becomes smoother when SPIP >> 1, the HTC still increases due to the increased number of nucleation sites from the splitting of cavities. It is also worth noting that for all the reviewed articles when HTC enhancement is reported, the roughness always shows an increase. However, when the HTC has deteriorated, the roughness does not always decrease.

The CHF is enhanced when the surface roughness increases since the effective contact area increases and because more liquid is trapped in the surface imperfections

preventing vapour layer formation. The increase in surface wettability also increases CHF since the nucleation site density is reduced due to a lower contact angle, and development of a vapour layer is avoided. When the fluid's capillarity increases, the CHF is enhanced since the wetting increases, which prevents dry regions under vapour bubbles.

When there is an increase in concentration, the thermal conductivity also increases, which helps enhance the heat transfer. However, it was proven that the viscosity also increases with concentration, which is undesirable in flow applications as it increases the power required to pump and increases pressure drop, which outweighs the benefits of higher thermal conductivity, as reported by Rejvani et al. (2019). A higher viscosity also decreases the Reynolds number, which, in turn, decreases the HTC.

### 2.3.2 Numerical review

Numerical studies have also been done to predict the HTC. They have been slowly gaining popularity since it is cost-effective, and a more comprehensive range of parameters can be varied easily. Fewer studies are available on pool boiling as compared to flow boiling. Since they use a similar concept, numerical flow boiling investigations were also included in this section.

Abadi *et al.* (2018) simulated pool boiling using 3D circular heated tubes with a roughness of 0.1 µm at different inclination angles in Fluent at atmospheric conditions. Water, FC-72, and ethanol were used at their respective saturation temperature. They used a two-phase Eulerian-Eulerian approach with RPI boiling model and realizable $k$-$\varepsilon$ model. It was found that water showed a higher HTC than the other two fluids and that as the inclination angle increases, the HTC decreases. They found a good agreement between the experimental and numerical data.

Ahmadpour *et al.* (2018) conducted a numerical investigation of pool boiling on a staggered tube bundle using water, R134a, R22, and ethanol as working fluids at different saturation temperatures. Two-phase Eulerian-Eulerian with RPI boiling model and realizable $k$-$\varepsilon$ model was used. They found that as the saturation temperature and pressure increase, the HTC increases. A more significant increase was seen for water as compared to the rest of the fluids. The HTC increased along with the tube bundle

when the heat flux was lower than 60 kW/m$^2$ for water and 30 kW/m$^2$ for the rest of the fluids. They noticed that the HTC increased with heat flux and remained constant after it increased past a certain threshold. It was found that ethanol had a better thermal performance than water. Their model agreed with experimental data.

Akbari *et al.* (2011) compared single & two-phase models for the simulation of $Al_2O_3$/water mixed convection heat transfer with 42 nm particle size and concentrations less than 2% vol. The single-phase and three distinct two-phase models (Eulerian, VOF, mixture) were compared against experimental data. The geometry consisted of a horizontal 4.5 mm diameter and 0.97 m long tube with uniform heat flux applied at the solid-liquid interface. The single-phase model (liquid) uses nanofluids' effective properties evaluated using appropriate correlations, whereas the two-phase models use both liquid and nanoparticles. For two-phase models, the Eulerian-Lagrangian and Eulerian-Eulerian approach was recommended for low and high particle concentrations. They found that the two-phase models were more accurate than the single phase. They concluded that all three two-phase models had almost the same accuracy for the given problem and that VOF was the least computationally expensive model to use.

Azari *et al.* (2014) carried out flow boiling experiments and 3D simulations focusing on the HTC of a laminar flow in a cylindrical copper tube using $Al_2O_3$/water nanofluid with concentrations of 0.03-2.5% vol. and particle size of 40 nm. They used three models: variable physical properties with single-phase (VP-SP), constant physical properties with single-phase (CP-SP), and two-phase discrete particle model. The comparison against experimental data showed that the two-phase model had a higher level of accuracy than the single-phase model. They reported an increase in HTC and increasing enhancement with Reynolds number.

Behroyan *et al.* (2018) investigated the effect of subcooled flow boiling of Cu/water and $Al_2O_3$/water at concentrations of 0.5%-2% vol. considering the change in surface wettability due to particle deposition on the heater wall using user defined functions (UDFs). The non-uniform particle distribution was also modelled. A 2D axisymmetric vertical cylindrical tube was used with Eulerian-Eulerian two-phase (nanofluid/vapour) and Eulerian-Lagrangian three-phase (water/vapour/nanoparticles) models and was compared against experimental data. The k-ε turbulence and heat partitioning models

were used, and a UDF was used for nucleate site density and bubble departure diameter. They found that CuO/water nanofluid had an HTC 2% higher than $Al_2O_3$/water. Both nanofluids showed an HTC lower than the base fluid. As the concentration increased, the HTC decreased such that at high concentrations (2% vol), the HTC decreased by 7% for Cu and 5% for $Al_2O_3$. The Eulerian-Lagrangian model predicted a higher HTC degradation than the Eulerian-Eulerian model. The models were validated against Chen's correlation, where the Eulerian-Lagrangian model showed 6% error and the Eulerian-Eulerian model showed 12% error. In their simulation, Ishii and Zuber's model was used for drag force. Lift force was by Tomiyama, wall lubrication force by Antal *et al.,* and turbulent dispersion force by Kurul and Podowski. The characteristic time for bubble induced turbulence was by Troshko and Hassan, and bubble induced turbulence and turbulent viscosity by Sato *et al.* The nucleation density and bubble departure diameter were by Li *et al.,* which was appropriate for nanofluids and bubble departure frequency by Cole.

Çiftçi and Sözen (2020) numerically and experimentally investigated the condensation and pool boiling heat transfer enhancement by using $SiO_2$/DCM and h-BN/dichloromethane (DCM) nanofluids at their respective saturation temperature and different concentrations from 0.5% to 1.5% vol. with a particle size of 50nm and 15-35nm, respectively. Their experimental and 2D numerical model is shown in Figure 18. They used a VOF multiphase model with k-ε RNG, enhanced wall treatment, and thermal effects selected. The authors reported improved heat transfer capabilities for both nanofluids when compared to the base fluid that as the particle concentration increased, the HTC increased for $SiO_2$/DCM up to 20%. In contrast, for h-BN/DCM, the maximum enhancement of 27% was seen at 1% vol concentration. The simulation results were consistent with the experimental results.

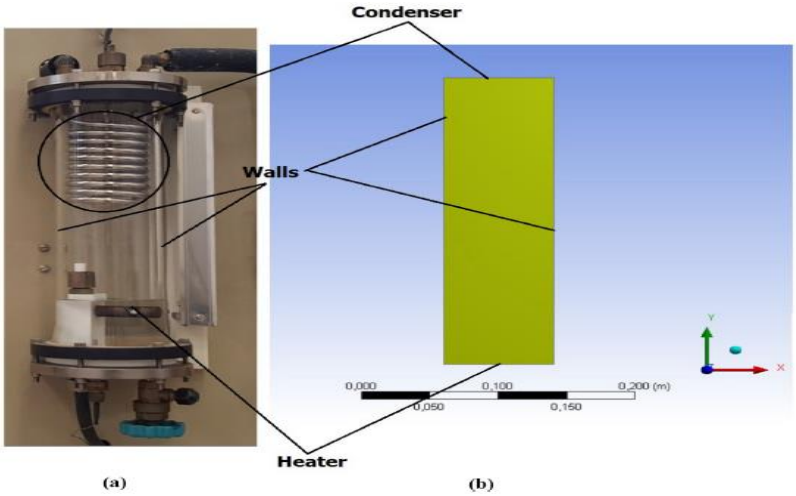


***Figure 18*** *(a) Experimental setup and (b) 2D model.*

Filho *et al.* (2016) used a two-phase Eulerian RPI boiling model to predict characteristics of subcooled flow boiling of pure water. A vertical stainless-steel tube with heated walls was modelled as 2D in ANSYS Fluent. The saturation pressure was varied (3.0, 4.5, and 1.5 MPa). They compared vapour volume fraction, bulk liquid temperature, and wall temperature to experimental data, where the model was found to have promising accuracy. The interfacial HTC was modelled according to Ranz and Marshall, whereas the bubble departure diameter was modelled according to Tolubinski and Kostanchuk. The drag force was by Ishii and Zuber, lift force by Tomiyama, wall lubrication force by Antal *et al.*, turbulence dispersion force by Lopez, and the virtual mass coefficient was given as 0.5.

Gobinath *et al.* (2018) numerically modelled sub-cooled pool boiling of $Al_2O_3$/water with a particle size of 46 nm and concentration of 0.02% vol. using single-phase steady 2D pressured-based implicit solver in ANSYS Fluent using different heater conditions. They used translational and rotational Peclet numbers, thermophoretic parameters, and time-scale equations for diffusion to analyze small particle motion due to diffusion/advection nano-scale heat transfer. They noticed that as the heat increased, the movement of the particle near the heater decreased and that the Peclet number had an important influence on the motion of nanoparticles in heat diffusion.

Gupta *et al.* (2019) examined the role of nanofluids in enhancing heat transfer capabilities. They used a horizontal stainless-steel rod as the heater that was submerged in pure water and $Al_2O_3$/water with varying concentration from 0.001% to 0.05% vol. They used a 2D transient Eulerian two-phase model to determine the HTC

at sub-atmospheric and atmospheric pressures. The HTC using nanofluid was found to be higher than when water was used. In addition, they noticed an increment in the HTC with an increase in heat flux, pressure, and particle concentration. Finally, they validated their model against experimental data and showed a maximum deviation of 9%.

Ham and Cho (2016) studied the effect of the size of nanoparticle (25-75 nm) and volume fraction (0.025%-0.1% vol.) on $Al_2O_3$/water pool boiling using the heat flux partitioning model. The results showed that the nanofluid had a lower HTC but higher CHF and surface wettability than base fluid. The increase in particle size and volume fraction had the effect of worsening the HTC. They also noticed that the bubble diameter increased, whereas bubble departure frequency and contact angle decreased with increased nanofluid concentration. The size of the nanoparticle had a negligible effect on the contact angle. The surface wettability also increased with an increase in particle diameter and concentration.

Hsu *et al.* (2017) looked into how the boiling curve was affected by the surface wettability using a VOF model and different contact angles from 5° up to 180° in ANSYS Fluent. Saturated water with a smooth horizontal surface as the heater was used at atmospheric conditions. They showed that, in general, the CHF decreases as the contact angle increases, whereas no clear conclusion was drawn for the effect on HTC. Their model was compared to other numerical and experimental work and showed good agreement.

Jiansheng *et al.* (2019) carried out a numerical investigation of the pool boiling of saturated water at atmospheric conditions on different heater geometries, including a plain surface and a surface with 36 hemispheres at multiple orientations. They found that the surface with hemisphere showed a better heat transfer performance than the plain surface, where the surface with a downward-facing hemisphere showed the highest HTC and the lowest CHF since it was easier to form a vapour blanket. Their simulation consisted of a 3D transient Eulerian with $k$-$\varepsilon$ model and specified a contact angle of 60°. The model was successfully validated and used drag force by Ishii.

Kamel *et al.* (2019) simulated the pool boiling of $SiO_2$/water (0.01% vol.) with the use of a two-phase Eulerian model with RPI boiling model. Using a UDF for nucleation site density and bubble departure diameter, they modelled the surface modification during

pool boiling. They showed that a bubble waiting time coefficient, $C_{wt}$, of 1 (standard) led to inaccurate results and thus suggested a correlation (Eq. 12) which, after using, showed good agreements with experimental data of pure water pool boiling. The $C_{wt}$ correlation in their study varied with superheat temperature and was specific for 0.01% vol. and in a separate study by same authors, it was shown that $C_{wt}$ varied with particle concentration. A steady-state simulation was used, and they mentioned that the results from steady-state and transient simulations had negligible differences. It was found that the nanofluid had a lower HTC than pure water. They used the *k-ε* turbulence model, Ishii model for drag, turbulent dispersion by Lopez, heat transfer coefficient by Ranz and Marshall.

$$C_{wt} = 0.1 + 2.5\left[1 - e^{-\left(\frac{T_w - T_{sat}}{22.442}\right)^{5.9}}\right] \quad (12)$$

Kim *et al.* (2017) used a two-phase VOF model to simulate pool boiling of $Al_2O_3$/water (2 – 4 % vol.), and pure water at different superheat temperatures ranging from 5 K to 20 K. Their simulated results showed an agreement for the shape and size of the bubbles with the experimental measurements. They found that the mean heat flux and the mean void fraction increase with wall superheat. The HTC increases slightly when the nanoparticle concentration increases due to higher thermal conductivity.

Krepper and Egorov (2007) carried out a sub-cooled water boiling simulation using a 2D domain at different mass flow, heat flux, and pressure conditions. They used a two-phase Eulerian, heat flux partitioning, and SST models. They reported expected results at medium heat fluxes but reported inconsistent results at higher heat flux and pressure. In their simulation, Ishii and Zuber's model was used for drag, lift force by Tomiyama, Antal *et al.* for wall lubrication, and turbulence dispersion by Burns.

Li *et al.* (2014) simulated nucleate pool boiling of $SiO_2$/water at concentrations of 0-0.1% vol. using a two-fluid model. They accounted for enhancement in the wettability of the surface due to deposition of nanoparticles by developing new correlations for bubble departure parameters. It was mentioned that in dilute nanofluids, the improved fluid properties that were caused by the addition of nanoparticles have little to no effect on the heat transfer, whereas the improvement in surface wettability was an essential factor. They suggest that the model's accuracy needs to be further improved by

considering the change in surface morphology due to the depositions. The correlation that they suggested for nucleation site density is given as $n = 1.206x10^4(1 - cos\theta)\Delta T_{sup}^{2.06}$ and showed better accuracy than other correlations. They mentioned that none of the correlations for bubble departure diameter found in the literature could predict correctly. The effect of bubble departure diameter was almost negligible. By comparing their model to experimental data, they concluded that the model's accuracy had increased by considering the effect of improved wettability but was still not satisfactorily accurate. They used bubble departure frequency by Cole, and Fritz, and Tolubinsky-Konstanchuk correlation for bubble departure diameter.

Li *et al.* (2011) created and validated the Eulerian multiphase flow boiling model to predict CHF using CFD solver ANSYS-Fluent. R113 was used, which flows through an annulus and a rectangular duct modelled in 2D and 3D, respectively. They concluded that the wall, liquid, and vapour fraction results were practically independent of which turbulence model is used. However, only the SST k-ω turbulence model could correctly predict the temperature distribution along the axis. Although many numerical studies have proven the enhancement of CHF, there have been some inconsistencies regarding HTC.

LiLi *et al.* (2012) performed a 3D numerical simulation of two-phase (vapour-liquid) water flow and boiling heat transfer in a horizontal steel tube using a multiphase model in Fluent. They used the *k- ε turbulence model* and added a UDF for the mass and energy source terms that De Schepper *et al.* (2009) presented to simulate the boiling phenomenon. The liquid temperature was at saturation temperature at 0-gauge pressure. They found that HTC increased with wall temperature and flow velocity. However, the authors did not show the validity of the model.

Lotfi *et al.* (2010) compared single-phase, two-phase mixture and the Eulerian model to determine the forced convection heat transfer of $Al_2O_3$/water on a horizontal tube with concentrations of 2%-7% vol. and 42 nm particle diameter. The *k- ε* turbulence model was used, and a comparison was done against the data collected from an experiment. They concluded that the mixture model was more accurate than the other two for this application. They then varied the concentration to understand its effect on the HTC and found that as the concentration increased, the HTC increased.

Mahdavi *et al.* (2018) investigated the deposition of 38 nm $Al_2O_3$ particles on a 20 mm diameter horizontal cylinder during pool boiling with water as the base fluid in two-phase (Eulerian-Eulerian) and three-phase (Eulerian-Lagrangian) frames. The selected turbulence model was k-ε realizable with wall y+ less than 1. The concentrations used were from 0%-4% vol. They used a 2D model and accounted for the roughness and nanoparticle deposition modifications by implementing UDFs for bubble departure diameter and nucleation site density. They found that as the nanoparticle concentration increased and the heat flux decreased, the deposition increased, and the HTC decreased compared to the base fluid. The bubble departure diameter increased, while the nucleation site density decreased with an increase in particle concentration. Nanoparticle deposition showed a more pronounced effect on the decrease of nucleation site density than the bubble departure diameter. In their simulation, Grace's model was used for drag, lift force by Tomiyama, Antal *et al.* for wall lubrication, turbulence dispersion by Burns, virtual mass force, according to Drew and Lahey. Heat transfer between phases was modelled using Ranz and Marshall, nucleation site density by Benjamin and Balakrishnan, and bubble departure diameter by Golorin *et al.* The last two models were mentioned to be appropriate for nanofluids.

Mohammed *et al.* (2018) investigated the effect of nanoparticle concentration on flow boiling in a 3D rectangular copper tube at saturation temperature of 309 K via CFD (ANSYS Fluent V.15) using mixture multiphase model. Still, the volume of fluid (VOF) model was also used to show vapour behaviour. Four phases were used: $ZnBr_2$/acetone, liquid, vapour acetone, and solid $ZnBr_2$ nanoparticles. They implemented UDF codes for energy and mass source terms due to evaporation as defined by Lee's model in 1980. The *k-ε* model was used, which was suitable for boiling since there was a presence of turbulence. A transient Reynolds Averaged Navier Stokes solver (RANS) with a time step of 0.005 sec. was used to run the simulation. They noticed that an increase in the nanoparticle concentration from zero to 1% vol. increased the HTC and the vapour volume fraction. The authors mentioned that the enhanced heat transfer was caused by the improved thermal conductivity of the fluid. The model was validated against experimental results and was in good agreement.

Naghibzadeh *et al.* (2020) compared the different interphase momentum exchange models in the Eulerian two-phase model to simulate and predict subcooled flow boiling

parameters in heated vertical tubes. After simulating 65 different cases, they concluded that the accuracy depends on the combination of interaction force models. They concluded that for their study, a combination of the Ishii model for drag, Antal *et al.* model for wall lubrication, Moraga and Saffman model for lift, turbulent interaction of Troshko-Hassan and DeBertodano for turbulent dispersion showed the best performance. They mentioned that the lift and wall lubrication forces had an insignificant effect on the results for most working conditions.

Renb and Zhoua (2020) studied the nucleate pool boiling outside a vertical tube under different pressures up to 10 kPa and liquid subcooling of up to 20 K using a 2D Eulerian-Eulerian VOF two-phase model. The effect of liquid height and tube length on the heat transfer have been investigated. A UDF was used to introduce the mass source term according to the Lee model to implement the phase change model. The researchers found that as the pressure and liquid subcooling increased, the wall superheat decreased, which increased the HTC. The vertical tube needed a higher heat flux to onset nucleate boiling as compared to the horizontal surface. The liquid height showed little to no effect on the heat transfer capabilities, whereas an increase in the tube length led to a decrease of HTC since large bubbles were forming on the tube wall.

Sato and Niceno (2018) conducted a numerical simulation of film and nucleate boiling using interface tracking method via CFD using a horizontal copper plate with heat flux from $50\ kW/m^2$ to $1500\ kW/m^2$ and concluded that the temperature and HTC obtained from the computation showed a good correlation with experimental work and that the CFD approach could be used for predictions.

Shetty *et al.* (2017) developed a numerical model for flow boiling of $Al_2O_3$/water inside a vertical axisymmetric steel tube using the two-phase Eulerian model, *k-ε* turbulence model and RPI boiling model in ANSYS Fluent. Concentration was varied from 0.001% 0.1% vol. and the inlet pressure, temperature, mass flow rate and heat flux were also varied. They found that the RPI model predicted the vapour volume fraction with good accuracy. The HTC for inlet velocity of 2.5 m/s was also predicted with decent accuracy compared to the experimental data. However, for 2 m/s and 1.5 m/s, the HTC was over predicted. They mentioned that the overprediction was that the assumption of taking inlet temperature for HTC calculation was not accurate. The HTC

deterioration was seen when nanofluids were used as compared to when water was used. In their simulation, additional terms were added to the k-ε model to account for bubble stirring and dissipation. They used Schiller and Naumann's model for drag force, Morega for lift force, Simonin for turbulent drift force. Nucleation density correlation used was by Lemmert and Chawla, departure frequency by Cole, bubble departure diameter by Tolubinsky and Kostanchuk.

Simon *et al.* (2010) used the Eulerian multiphase model with *k-ε* turbulence model to predict refrigerant nucleate boiling in heat exchangers. They used the Ishii and Chawla model for drag force, lift coefficient of 0.25 for lift force, Antal *et al.* for wall lubrication force, Kurul and Podowski for turbulent dispersion, and Sato for turbulent viscosity. Nucleation density correlation used was by Lemmert and Chawla, nucleation frequency by Cole, bubble departure diameter by Unal, Nusselt number by Ranz and Marshall, and the bubble diameter by Zeitoum and Shoukri. They concluded that the model was adequate to simulate nucleate boiling by validating it against experimental data. However, they mentioned that the diameter of the bubble needs to be modelled using a transport equation instead.

Soleimani *et al.* (2020) performed a thermal analysis of a heat sink with microchannels cooled by flow boiling of $Al_2O_3$/HFE-7100 nanofluid with concentrations of 1%-4% vol. and a particle size of 36nm. They used a VOF 2-phase model and neglected the deposition effect during boiling. The HTC was enhanced up to only 3% at the highest concentration compared to when only the base fluid was used. They reported 96% and 94% accuracy when temperature and HTC were compared to experimental data.

Wua *et al.* (2007) simulated in Fluent the two-phase flow boiling of R-141B in horizontal serpentine tubes using transient Eulerian multiphase model at a time step of 1-5 sec. The authors mentioned that this model was suitable since it handles coupling between phases and provides modelling for turbulence and interphase drag laws. They used k-ε realizable turbulence model with near-wall turbulence modelling for enhanced wall function treatment and used UDF source terms to model phase change heat and mass transfer, for which Lee's model was used. Ranz and Marshall's model was used to calculate the HTC between the two phases, and Schiller and Naumann's model was used for the drag coefficient. The pressure was 101.3 kPa, and at a saturation temperature of 308 K. They investigated different mass flow rates and heat fluxes.

They found that the vapour void fraction decreases as the mass flux increases at the exit. Their simulation results were shown to have good accuracy when compared to the experimental results.

To conclude, valuable information was obtained from the numerical studies in terms of the models used by different authors. The choice of models in this study were decided from the reviewed numerical studies, their reported accuracy and relevancy to present study. It can be noticed that most studies used 2D two-phase Eulerian-Eulerian *k-ε* realizable models and all reported good accuracy. It was also learnt steady state and transient simulations provide similar results. It was worth noting that, as found by Kamel *etl al.* (2019), the bubble waiting time coefficient is a function of multiple parameters such as superheat temperature and volume concentration. The RPI model was used extensively and was proven to be accurate for predicting vapour volume fraction by Shetty *et al.* (2017). The authors commonly used the following models: Ishii for drag force although Grace was also accurately used, Tomiyama for lift force, Antal-et-al for wall lubrication, Burns and Lopez for turbulent dispersion, Drew and Lahey for virtual mass force, Cole for departure frequency, and Ranz Marshall for interfacial heat transfer coefficient. Since the accuracy using these models was proven by various authors in literature, they were also implemented in this study as discussed in section 3.

### 2.3.3 Mathematical model

Researchers have developed some models that relate the surface roughness to the HTC. Gorenflo *et al.* (1993) present a correlation that relates the HTC to the surface roughness for pure fluids:

$$\frac{h}{h_o} = C * F(Pr) * \left(\frac{q}{q_o}\right)^n, \qquad C = \left(\frac{Ra}{Ra_o}\right)^{0.133}, \qquad Ra_o = 0.4\mu\text{m}, \tag{13}$$

$$q_o = 20\ \text{kW/m}^2, \qquad h_o = 5600\ \text{W/m}^2\text{K (water)}$$

Where $q_o, h_o\ and\ Ra_o$ are the fixed reference heat flux, specific heat transfer coefficient, and reference roughness value, respectively, according to the VDI Heat Atlas (Gorenflo *et al*., 1993). F(Pr) is the pressure correction factor calculated as:

$$For\ water\text{:}\ F(Pr) = 1.73Pr^{0.27} + \left(6.1 + \frac{0.68}{1-Pr}\right)Pr^2, \qquad n = 0.9 - 0.3Pr^{0.15} \tag{14}$$

$$Other\ fluids:\ F(Pr) = 1.2Pr^{0.27} + \left(2.5 + \frac{1}{1-Pr}\right)Pr, \qquad n = 0.9 - 0.3Pr^{0.3} \tag{15}$$

Where $Pr$ is the reduced pressure. The correlation can be simplified by assuming a constant heat flux and pressure, and thus, the nanofluid to base fluid HTC ratio can be written as:

$$\frac{h_{nf}}{h_{bf}} = \frac{C_{nf}}{C_{bf}} = \left(\frac{Ra_{new}}{Ra_{og}}\right)^{0.133} \tag{16}$$

Where $h_{nf}$ and $h_{bf}$ are the nanofluid and base fluid HTC, respectively and $Ra_{new}$ and $Ra_{og}$ are the new modified surface roughness after nanoparticle addition and original surface roughness, respectively.

Similarly, by assuming constant superheat temperature and given that n = 0.77 for atmospheric conditions (water), the correlation can be simplified to:

$$\frac{h_{nf}}{h_{bf}} = \left(\frac{Ra_{new}}{Ra_{og}}\right)^{0.57} \tag{17}$$

Equations 16 and 17 show that as the surface roughness increases, the HTC increases and have shown to predict the HTC enhancement with reasonable accuracy when tested using data from previously selected literature.

Nikman *et al.* (2014) derived a correlation based on data from previous literature by using bisquare least square fitting method. The equation predicts the modified surface roughness given the original surface roughness and nanoparticle size and is given as follows:

$$Ra_{new} = 1.73 * \frac{Ra_{og}}{{d_p}^{0.122}} \tag{18}$$

Therefore, by substituting equation 18 into equations 16 and 17, the enhancement in heat transfer coefficient can be directly related to the particle size:

$$Constant\ heat\ flux: \qquad \frac{h_{nf}}{h_{bf}} = \left(\frac{1.73}{{d_p}^{0.122}}\right)^{0.133} \tag{19}$$

$$Constant\ superheat: \qquad \frac{h_{nf}}{h_{bf}} = \left(\frac{1.73}{{d_p}^{0.122}}\right)^{0.57} \tag{20}$$

These equations show that surface roughness and thus HTC increases for all nanoparticle sizes below 90 nm regardless of the surface roughness. However, since the equation does not consider the relative size of the nanoparticle and surface roughness, its accuracy can be questioned.

## 2.4 Summary of the reviewed literature

By noting the outcomes of the reviewed studies, it is evident that there are some contradicting findings. This is because the outcomes depend significantly on how the experiment was set up, the conditions, and the parameters used. Table 1 summarises the effects of different parameters to help better understand their general effects on the outcome. Table 2 and Table 3 summarise experimental and numerical studies, respectively.

**Table 1.** Summary of the effect of parameters on CHF and HTC.

| ***Parameter*** | ***CHF*** | ***HTC*** | ***Cause*** |
|---|---|---|---|
| Higher heat flux | - | Increases | Nucleation site density increases, contact angle decreases |
| Higher concentration | Increases | Increases/ Decreases | Increase at low concentration due to enhanced thermal conductivity and higher deposition surface roughness. Decreases at high concentrations due to the increase in deposition thickness lead to higher thermal resistance, which counters the enhancement of surface roughness. Contact angle decreases |
| Higher thermal conductivity | - | Increases | Heat conduction increases |
| Higher suspension stability | - | Increases | Agglomeration decreases |
| Higher surface tension | - | Decreases | Bubble frequency and nucleation site density decreases, bubble diameter increases |
| Higher bubble diameter | - | Decreases | Nucleation site density decreases |
| Higher bubble frequency | - | Increases/ Decreases | Increases microlayer evaporation and thus increases deposition, either increasing or decreasing HTC. |
| Higher nucleation site density | - | Increases | Increases turbulence and thus the convection heat transfer |

| *Parameter* | *CHF* | *HTC* | *Cause* |
|---|---|---|---|
| Higher surface roughness | Increases | Increases | Higher nucleation site density. Increases contact area. Liquid traps in pores and prevents vapour layer from forming |
| Higher surface-particle interaction parameter (SPIP) | - | Increases if away from 1. Decreases if near 1 | Nucleation sites are multiplied when particles sit on the sites. The porous structure becomes blocked, leading to fewer nucleation sites |
| Higher deposition thickness | Increases | Decreases | At higher concentrations, Thermal resistance increases and outweighs surface roughness improvement. Higher wettability is due to a decrease in contact angle, which decreases nucleation sites. Thickness increases with boiling time |
| Higher pressure | - | Increases | Surface tension decreases |
| Higher wettability | Increases | Decreases | Delays vapour film blanket, decreases contact angle which decreases nucleation sites |
| Higher particle diameter | - | Decreases | Thermal conductivity enhancement decreases. Finer particles have a higher enhancement due to a larger surface area. |

**Table 2.** Summary of previous experimental research involving nanofluids pool boiling.

| *Reference/year* | *Heater type* | *Nanofluid* | *Particle size (nm)* | *Concentration* | *Initial roughness (nm) & [SPIP]* | *Operating pressure* | *HTC* | *CHF* |
|---|---|---|---|---|---|---|---|---|
| Ahmed and Hamed (2012) | Flat copper block | $Al_2O_3$/water | 40-50 | 0.01-0.5% vol. | 50 [1-1.25] | Atm | Enhanced at 0.01% vol. deteriorated at higher % (Roughness increased) | - |
| Ayoobia *et al.* (2020) | Cr-Al-Fe wire | $Fe_3O_4$/water | <100 | 0.01% vol. | - | Atm | Enhanced | +160% |
| Chang and bang (2005) | Stainless steel plate | $Al_2O_3$/water | 47 | 0.5-4% vol. | 37.2 [0.79] | Atm | Deteriorated (Roughness increased) | +32% |

| *Reference/year* | *Heater type* | *Nanofluid* | *Particle size (nm)* | *Concentration* | *Initial roughness (nm) & [SPIP]* | *Operating pressure* | *HTC* | *CHF* |
|---|---|---|---|---|---|---|---|---|
| Chopkar *et al.* (2008) | Copper plate | $ZrO_2$/water | 20-25 | 0.005-0.15% vol. | 642 [25.68-32.1] | Atm | Enhanced at low conc. Deteriorated at high conc. (Roughness decreased) | - |
| Coursey and Kim (2008) | Copper block | $Al_2O_3$/water<br>$Al_2O_3$/water | 45 | 0.026-1.02 g/L<br>0.001-10 g/L | - | Atm | No change | +37%<br>+25% |
| Das and Putra (2003) | Stainless steel tube | $Al_2O_3$/water | 20-50 | 0.1-4% vol. | 420, 1150 [8.4-21, 23-57.5] | Atm | Deteriorated (Roughness decreased). | - |
| Golubovic *et al.* (2009) | NiCr wire | $Al_2O_3$/water<br>$BiO_2$/water | 22.6-46<br>38 | All 0-0.01 g/L | - | 101.3 kPa | - | +50%<br>+33% |
| Ham *et al* (2017) | Copper bar | $Al_2O_3$/water | 50 | 0.001-0.1% vol. | 117.5, 292.8 [2.35, 5.85] | 3 kPa | Deteriorated (Roughness increased) | +225 |
| Harish *et al.* (2011) | Aluminum disk | $Al_2O_3$/water | 50 | 0.5-2% vol. | 53, 308 [1.06, 6.16] | Atm | -30% for smooth. (Roughness decreased) Enhanced for rough surface. (Roughness increased) | - |
| He *et al.* (2016) | NiCr wire | ZnO/EG/ water | - | 5.25-8.25% vol. | - | Atm | Enhanced | Enhanced |
| Heris (2011) | Cartridge heater (Cylinder) | CuO/EG/ water | 40 | 0.1-0.5% vol. | 1000 [25] | Atm | +55% | - |
| Huang *et al.* (2011) | Nickel wire | $TiO_2$/water | 110-220 | 0.01-1 wt% | - | Atm | Deteriorated | 83% |
| Kamel and Lezsovits (2020) | Copper tube | $CeO_2$/water | 50 | 0.001-0.04% vol. | 115 [2.3] | Atm | +70% At 0.007% vol. (Roughness increased) | - |
| Kathiravan *et al.* (2009) | Stainless steel tube | Cu/water | 10 | 0.25-1 wt% | 1090 [109] | Atm | Deteriorated (Roughness decreased) | +59% |
| Kathiravan *et al.* (2010) | Stainless steel plate | Cu/water<br>Cu/SDS/ water | 10<br>10 | 0.25-1 wt%<br>0.25-1 wt%/9 wt% | 167 [16.7] | Atm | Deteriorated (Roughness decreased) | +48%<br>+75% |

| ***Reference/year*** | ***Heater type*** | ***Nanofluid*** | ***Particle size (nm)*** | ***Concentration*** | ***Initial roughness (nm) & [SPIP]*** | ***Operating pressure*** | ***HTC*** | ***CHF*** |
|---|---|---|---|---|---|---|---|---|
| Khooshehchin *et al.* (2020) | Copper cylinder | CuO/water | 20-60 | 0.025-0.125 wt% | 840 [14-42] | Atm | Enhanced | - |
| Kim (2014) | Copper block | CuO/water | 80 | 0.1% vol | 220, 1340, 2320 [2.75, 16.75, 29] | Atm | Deterioration | - |
| Kim *et al.* (2006) | NiCr & Ti wires | $Al_2O_3$/water<br>$TiO_2$/water | 47<br>85 | All 0.00001-0.1% vol. | - | 101.3 kPa | - | +176%<br>+200% |
| Kim *et al.* (2007) | Stainless steel wire | $Al_2O_3$/water<br>$ZrO_2$/water<br>$SiO_2$/water | 110-210<br>110-250<br>20-40 | All 0.001-0.1% vol. | 100 [0.47-5] | Atm | Deteriorated (Roughness increased) | +52%<br>+75%<br>+80% |
| Kshirsagar and Shrivstava (2018) | NiCr wire | $Al_2O_3$/water | 30 | 0.3-1.5 wt% | 111 [3.7] | Atm | Enhanced (Roughness increased) | +87% |
| Kwark *et al.* (2010) | Coppper plate | $Al_2O_3$/water<br>CuO/water<br>Diamond/water | 139<br>143<br>86 | All 0.001-1 g/L | - | 19.9 kPa and Atm | Deteriorated | All +80% |
| Li *et al.* (2020) | Finned copper | CuO/water | 45 | 0.025-0.1 wt% | - | Atm | Enhanced with a decrease in fin spacing | - |
| Liu *et al.* (2007) | Micro grooved Copper | CuO/water | 30 | 0.1-2 wt% | - | 7.4-100 kPa | Enhanced at low conc. Deteriorated at high conc. | +200% |
| Manetti *et al. (2016)* | Copper cylinder | $Al_2O_3$/water<br>$Fe_2O_3$/water | 10 | 0.029-0.29 g/L | 50, 230 [5, 23] | Atm | Enhancement at low conc. for smooth surf. (Roughness increased) | - |
| Narayan *et al.* (2007) | Vertical SS tubes | $Al_2O_3$/water | 47-150 | 0.5-2 wt% | 48, 98, 524 [0.32-11.1] | Atm | +70% for SPIP >1, -45% for SPIP <1 | - |
| Nazari and Saedodin (2018) | Aluminium rod | $Al_2O_3$/water | 47 | 0.002-0.1% vol. | 147 [3.12] | 86 kPa | Deteriorated | +19% |
| Okawa *et al.* (2012) | Copper block | $TiO_2$/water | 21 | 0.000094-0.047% vol. | - | Atm | Deteriorated initially then enhanced | +91% |

| *Reference/year* | *Heater type* | *Nanofluid* | *Particle size (nm)* | *Concentration* | *Initial roughness (nm) & [SPIP]* | *Operating pressure* | *HTC* | *CHF* |
|---|---|---|---|---|---|---|---|---|
| Park *et al.* (2009) | Flat copper block | CNT/water | 10-20 | 0.0001-0.05% vol. | - | Atm | Deteriorated | +200% |
| Pham *et al.* (2012) | Stainless steel plate | $Al_2O_3$/water CNT/BA/water $Al_2O_3$/CNT/water | - | 0.05% Vol. 0.05%/10% Vol. 0.05%/0.05% Vol. | 54 | Atm | - | +33% +108% +122% |
| Rostami *et al.* (2020) | Copper cylinder | NiO/water | 10-60 | 0.005-0.2% vol. | 330 [5.5-33] | Atm | +56.4 % with magnetic field | - |
| Sarafraz & Hormozi (2016) | Copper Micro-finned and plain surface | Multi-walled carbon nanotube/ water | 10-20 | 0.1-0.3 wt% | - | Atm | +77% compared to plain surface | +95% compared to plain surface |
| Sheikhbahai *et al.* (2012) | NiCr wire | $Fe_3O_4$/EG/ water | <50 | 0.01-0.1% vol. | - | Atm | Deteriorated | +100% |
| Shoghl and Bahrami (2013) | Stainless steel rod | ZnO/water CuO/water | <150 | All 0.01-0.02 wt% | 150 [>1] | Atm | Enhanced with surfactant. Deteriorated without. (Roughness decreased) | - |
| Soltani *et al.* (2009) | Stainless steel block | γ-$Al_2O_3$/water $SnO_2$/water | 20-30 55 | 0.3-2 wt% 0.5-3 wt% | - | Atm | +30% +20% | - |
| Suriyawong and Wongwises (2010) | Copper plate Aluminium plate | $TiO_2$/water | 21 | 0.00005-0.01% vol. | 200, 4000 each [9.52-190] | Atm | +15% Deteriorated | - |
| Trisaksri and Wongwises (2009) | Copper tube | $TiO_2$/R-141b | 21 | 0.01-0.05% vol | 3140 [149.5] | 400-500 kPa | Deteriorated | - |
| Vassallo *et al.* (2004) | NiCr wire | $SiO_2$/water | 15-3000 | 0.5% vol. | - | 101.3 kPa | No change | +200% |
| Wen and Ding (2005) | Stainless steel disk | $Al_2O_3$/water | 10-50 | 1.25 wt% | - | Atm | +40% (no deposition) | - |

| *Reference/year* | *Heater type* | *Nanofluid* | *Particle size (nm)* | *Concentration* | *Initial roughness (nm) & [SPIP]* | *Operating pressure* | *HTC* | *CHF* |
|---|---|---|---|---|---|---|---|---|
| Wen *et al.* (2011) | Brass plate | $Al_2O_3$/water | 20-150 | 0.001-0.1% vol. | 25, 420 [0.16-1.25, 2.8-21] | Atm | +200% for smooth plate (Roughness increased) no change for rough surface (Roughness unchanged) | - |
| White *et al.* (2010) | Stainless steel plate | ZnO/water | 40 | 2.3% vol. | 60 [1.5] | Atm | For NF decreases and for water increases with roughness (Roughness increased) | - |
| Witharana (2003) | Copper plate | Au/water $SiO_2$-EG/water | 30 | 0.0002-0.001 wt% 0.025 wt% | - | Atm | +21% Deteriorated | - |
| Yang and Liu (2011) | Copper bar | $SiO_2$/water | 30 | 0.5-2.5 wt% | 35.1 [1.17] | 103-7.4 kPa | +27.3% (No deposition) | No change |
| Yao *et al.* (2018) | Copper plate | $SiO_2$/water $Al_2O_3$/water $SiO_2/Al_2O_3$/ water | 30-50 | 0.01 wt% | - | 101 kPa | +51.8% +32.6% +18.3% | +41.9% +22.1% +7.9% |
| You *et al.* (2003) | Copper plate | $Al_2O_3$/water | - | 0-0.05 g/L | - | 19.9 kPa | No change | +200% |

**Table 3.** Summary of previous numerical research involving nanofluids.

| ***Reference /year*** | ***Geometry*** | ***Nanofluid*** | ***Model*** | ***Concentration*** | ***Type of boiling*** | ***Findings*** |
|---|---|---|---|---|---|---|
| Akbari *et al.* (2011) | Horizontal tube | $Al_2O_3$/water 42 nm | 2-phase VOF, Eulerian, mixture. 1-phase | <2% vol. | Flow | All 3 models have similar accuracy. Eulerian-Eulerian is recommended for high concentration. |
| Azari *et al.* (2014) | Copper cylindrical tube | $Al_2O_3$/water 40 nm | 3D 1-phase 3D 2-phase with DPM | 0.03-2.5% vol. | Flow | HTC was enhanced. 2-phase DPM model was more accurate. |
| Behroyan *et al.* (2018) | Vertical cylindrical tube | $Al_2O_3$/water CuO/water | 2D, *k- ε* HFP Euler-Euler 2-phase, Euler-Lagrang. 3-phase | 0.5-2% vol. | Flow | HTC deteriorated. The Euler-Lagrangian 3-phase model was more accurate |
| Çiftçi and Sözen (2020) | Horizontal copper cylinder | $SiO_2$/DCM 50nm h-BN/DCM 15-35 nm | 2D VOF multiphase *k- ε RNG* | 0.5-1.5% vol. | Pool | HTC enhanced by 20% ($SiO_2$/DCM) and 27% (h-BN/DCM) |
| Gobinath *et al.* (2018) | Horizontal copper cylinder | $Al_2O_3$/water | 2D 1-phase | 0.02% vol | Pool | Their results were underpredicted but had reasonable accuracy. |
| Gupta *et al.* (2019) | Horizontal Stainless-steel rod | $Al_2O_3$/water | 2D Eulerian 2-phase | 0.001-0.05% vol. | Pool | HTC was enhanced and increased with pressure, heat flux and concentration. |
| Ham and Cho (2016) | Flat plate | $Al_2O_3$/water 25-75nm | HFP 2-phase | 0.025-0.1% vol. | Pool | HTC deteriorated but CHF enhanced. |
| Kamel *et al.* (2019) | Flat plate | $SiO_2$/water | 2D 2-phase HFP Eulerian, *k- ε* | 0.01% vol. | Pool | HTC deteriorated. |
| Kim *et al.* (2017) | Vertical plate | $Al_2O_3$/water | VOF 2-phase | 2-4% vol. | Pool | HTC enhanced with concentration |
| Li *et al.* (2014) | Flat plate | $SiO_2$/water | 2-phase HFP Eulerian | 0-0.1% vol. | Pool | HTC deteriorated. They suggest modelling change in surface morphology due to deposition |
| Lofti *et al.* (2010) | Horizontal tube | $Al_2O_3$/water 42 nm | 2-phase mixture, Eulerian. *k- ε* | 2-7% vol. | Flow | Mixture model was more accurate. HTC increased with concentration. |

| *Reference /year* | *Geometry* | *Nanofluid* | *Model* | *Concentration* | *Type of boiling* | *Findings* |
|---|---|---|---|---|---|---|
| Mahdavi *et al.* (2018) | Horizontal cylinder | $Al_2O_3$/water 38 nm | 2D 2-phase Euler-Euler, 3-phase Euler-Lagrang *k- ε* realizable | 0-4% vol. | Pool | HTC deteriorated. Particle deposition is dependent on concentration. and heat flux |
| Mohammed *et al.* (2018) | Copper rectangular tube | $ZnBr_2$/water | 3D Mixture 4-phase *k- ε* | 0-1% vol. | Flow | HTC and vapour fraction increased with concentration. Model was validated. |
| Shetty *et al.* (2017) | Vertical steel tube | $Al_2O_3$/water | 2-phase Eulerian RPI *k- ε* | 0.001-0.1% vol. | Flow | HTC deteriorated. The RPI model predicted vap. vol frac. accurately. |
| Soleimani *et al.* (2020) | Micro-channel heat sink | $Al_2O_3$/HFE-7100 | 2-phase VOF | 1-4% vol. | Flow | HTC enhanced up to 3%. 96% accuracy (temperature) |

# 3 METHOD OF SOLVING

The models used during the simulation are provided in detail in this section. The choice of the models were motivated at the end of section 2.3.2.

## 3.1 Eulerian-Eulerian two-phase model

Given the nature of pool boiling, the numerical investigation needs to be carried out for a multiphase and transient case under the effect of gravity. The Eulerian-Eulerian modelling framework was adopted so that each phase is treated as a continuum. The Eulerian-Eulerian model was proven to have a good accuracy while at the same time not being as computationally expensive as other models such as Eulearian-Lagrangian. The governing equations can be written according to ANSYS (2017) as follows for the conservation of mass in the general form:

$$\frac{\partial}{\partial t}\left(\alpha_q \rho_q\right) + \nabla \cdot \left(\alpha_q \rho_q \vec{v}_q\right) = \sum_{p=1}^{n}\left(\dot{m}_{pq} - \dot{m}_{qp}\right) + S_q \qquad (21)$$

Where $\alpha_q, \vec{v}_q, \dot{m}_{pq}, \dot{m}_{qp}\ and\ S_q$ are the volume fraction of phase $q$, the velocity of phase $q$, the mass transfer between phases $p$ and $q$, mass transfer between phases $q$ and

$p$, and the source term, respectively. $q$ and $p$ can be replaced with the liquid (subscript $l$) or vapour (subscript $v$) phase.

The momentum equation can also be expressed using the volume fraction:

$$\frac{\partial}{\partial t}(\alpha_q \rho_q \vec{v}_q) + \nabla \cdot (\alpha_q \rho_q \vec{v}_q \vec{v}_q) = -\alpha_q \nabla \mathrm{p} + \nabla \cdot \bar{\bar{\tau}}_q + \alpha_q \rho_q \vec{g} + \sum_{p=1}^{n} (\vec{R}_{pq} + \dot{m}_{pq} \vec{v}_{pq} - \dot{m}_{qp} \vec{v}_{qp}) + (\vec{F}_{drag,q} + \vec{F}_{lift,q} + \vec{F}_{wl,q} + \vec{F}_{vm,q} + \vec{F}_{td,q}) \quad (22)$$

Where $\vec{F}_{drag}$ denotes the drag force, $\vec{F}_{lift,q}$ is the lift force, $\vec{F}_{wl,q}$ is the lubricant force of wall, $\vec{F}_{vm,q}$ is the virtual mass force, $\vec{F}_{td,q}$ is the turbulent dispersion force, $\vec{v}_{pq}$ is the interphase velocity, $\vec{R}_{pq}$ is the interaction force between the phases, and $\bar{\bar{\tau}}_q$ is the stress-strain tensor of phase $q$ given as:

$$\bar{\bar{\tau}}_q = \alpha_q \mu_q \left(\nabla \vec{v}_q + \nabla \vec{v}_q{}^T\right) + \alpha_q \left(\lambda_q - \frac{2}{3}\mu_q\right) \cdot \nabla \vec{v}_q \bar{\bar{I}} \quad (23)$$

Where $\lambda_q$ and $\mu_q$ are the bulk and shear viscosity of phase $q$, respectively and $\bar{\bar{I}}$ is the unit tensor.

The energy equation is as follows:

$$\frac{\partial}{\partial t}(\alpha_q \rho_q h_q) + \nabla(\alpha_q \rho_q \vec{u}_q h_q) = -\alpha_q \frac{dp_q}{dt} + \bar{\bar{\tau}}_q \cdot \nabla \cdot \vec{u}_q - \nabla \cdot \vec{q}_q + S_q + \sum_{p=1}^{n} (Q_{pq} + \dot{m}_{pq} h_{pq} - \dot{m}_{qp} h_{qp}) \quad (24)$$

Where $h_q$ represents the specific enthalpy for phase $q$, $\vec{q}_q$ denotes the heat flux, $S_q$ is the source term, $h_{pq}$ stands for the interphase enthalpy and, $Q_{pq}$ is the heat transfer rate between phase $p$ and $q$ calculated as:

$$Q_{pq} = h_i A_i (T_p - T_q) \quad (25)$$

Where $h_i$, $T$ are the interfacial heat transfer and fluid temperature, respectively and $A_i$ is the interfacial area given as:

$$A_i = \frac{6\alpha_v(1-\alpha_v)}{d_v} \tag{26}$$

Where $d_v$ is calculated based on Sauter mean diameter:

$$\frac{d_v}{\sqrt{\sigma/g\Delta\rho}} = \frac{0.0683\left(\rho_l/\rho_g\right)^{1.326}}{Re^{0.324}\left(Ja + \left(\frac{149.2\left(\rho_l/\rho_g\right)^{1.326}}{Bo^{0.487}Re^{1.6}}\right)\right)} \tag{27}$$

Where *Re, Bo,* and *Ja* are the Reynolds, boiling, and Jakob numbers, respectively.

## 3.2 Interfacial force

The drag force is used with the Grace coefficient that is present in ANSYS:

$$\vec{F}_{drag,q} = \frac{A_i C_D Re \mu_k}{8 d_v}|V_i - V_v|(V_i - V_v) \tag{28}$$

$$C_D = max\left[C_{Dsphere}, min\left(C_{Dcap}, C_{Dellipse}\right)\right]$$

$$C_{Dellipse} = \frac{4gd_l(\rho_k - \rho_l)}{3{U_t}^2\rho_l}, \qquad C_{Dcap} = \frac{8}{3}, \qquad C_{Dsphere} = \begin{cases} \frac{24}{Re} & Re \le 0.01 \\ \frac{24(1+0.15Re^{0.687})}{Re} & Re \ge 0.01 \end{cases}$$

$$Re = \frac{\rho_k d_l}{\mu_k}|V_i - V_v|, \qquad U_t = \frac{\mu_k {M_O}^{-0.149}}{\rho_k d_v}(J - 0.857), \qquad H = \frac{4}{3}E_O {M_O}^{-0.149}\left(\frac{\mu_k}{0.0009}\right)^{-0.14}$$

$$J = \begin{cases} 0.94H^{0.757} & 2 \le H \le 59.3 \\ 3.42H^{0.441} & H \ge 59.3 \end{cases}, \qquad E_O = \frac{g(\rho_l - \rho_v){d_v}^2}{\sigma}, \qquad A_i = \frac{6\alpha_v(1-\alpha_v)}{d_v}$$

In this equation, $E_O$ and $M_O$ are the Eötvös number and Morton number, respectively.

The lift force is used with the Tomiyama coefficient present in ANSYS:

$$\vec{F}_{lift,q} = C_L\alpha_k\rho_k(V_l - V_k)\mathrm{x}(\nabla \mathrm{x} V_k) \tag{29}$$

$$C_L = \begin{cases} min[0.288\,tanh(0.121Re), f(E_{Od})] & E_O < 4 \\ f(E_{Od}) = 0.00105{E_{Od}}^3 - 0.0159{E_{Od}}^2 - 0.0204E_{Od} + 0.474 & 4 < E_O < 10 \\ -0.29 & E_O > 10 \end{cases}$$

$$E_{Od} = \frac{g(\rho_k - \rho_l){d_l}^2}{\sigma}\left(1 + 0.163{E_O}^{0.757}\right)^{2/3}$$

The lubrication force of the wall is used with the Antal et al. coefficient present in ANSYS:

$$\vec{F}_{wl,q} = C_w \alpha_v \rho_k |V_i - V_v|^2 n_k$$
$$C_w = \max\left(0, \frac{C_{w1}}{d_l} + \frac{C_{w2}}{y_w}\right), C_{w1} = -0.01, C_{w2} = 0.05 \quad (30)$$

The virtual mass force model used is by (Drew & Lahey,1993):

$$\vec{F}_{vm,q} = 0.5\alpha_k \rho_k \left(\frac{DV_l}{Dt} - \frac{DV_v}{Dt}\right) \quad (31)$$

The turbulence dispersion force is used with burns-et-al coefficient present in ANSYS:

$$\vec{F}_{td,q} = \frac{C_D \mu_k^t}{\rho_k Sc_b}\left(\frac{\nabla\alpha_l}{\alpha_l} - \frac{\nabla\alpha_v}{\alpha_v}\right) \quad (1)$$

### 3.3 Turbulence modelling

*k-ε* realizable model has been used to model the turbulence for liquid and gas phase in previous studies and has been proven to provide accurate results, and for this reason, it will be used in the current study. The *k-ε* model is presented as:

$$\frac{\partial}{\partial t}(\alpha_q \rho_q k_q) + \nabla(\alpha_q \rho_q \vec{u}_q k_q) = \nabla \cdot \left(\frac{\alpha_q \mu_q}{\sigma_k} \nabla k_q\right) + \alpha_q \bar{\bar{\tau}}_q^T : \nabla \vec{u}_q - \alpha_q \rho_q \varepsilon_q + {S_q}_k^{int} \quad (32)$$

$$\frac{\partial}{\partial t}(\alpha_q \rho_q k_q) + \nabla(\alpha_q \rho_q \vec{u}_q \varepsilon_q) = \nabla \cdot \left(\frac{\alpha_q \mu_q}{\sigma_\varepsilon} \nabla \varepsilon_q\right) + \frac{\alpha_q \varepsilon_q}{k_q}\left(C_{\varepsilon 1} \bar{\bar{\tau}}_q^T : \nabla \vec{u}_q - C_{\varepsilon 2} \rho_q \varepsilon_q\right) + {S_q}_\varepsilon^{int} \quad (33)$$

Where $k$ and ε in above equations represent the turbulence kinetic energy and dissipation rate, respectively and the constants for the *k-ε* model are set according to

Behroyan *et al.* (2018) as $C_\mu = 0.09$, $C_{\varepsilon 1} = 1.44$, $C_{\varepsilon 2} = 1.92$, $\sigma_k = 1.0$ and $\sigma_\varepsilon = 1.3$. the terms $S_{l_k}^{int}$ and $S_{l_\varepsilon}^{int}$ are the source terms that account for the bubble induced turbulence given according to (W. Yao, 2004) as:

$$S_{l_k}^{int} = -(\vec{F}_{drag,l} + \vec{F}_{vm,l}) \cdot (\vec{u}_v - \vec{u}_l) \tag{34}$$

$$S_{l_\varepsilon}^{int} = C_{\varepsilon 3} \frac{S_{l_k}^{int}}{\tau_b}, \tau_b = \left[\frac{(d_v)^2}{\varepsilon_l}\right]^{1/3} \tag{35}$$

Where $C_{\varepsilon 3} = 0.45$ according to Behroyan *et al.* (2018).

### 3.4 Heat flux partitioning model

Even though nanoparticle deposition changes the heater surface's properties and morphology, it is believed that the heat transfer mechanism remains the same as that of a clean surface. Therefore, the RPI boiling model can still be used to model the boiling along the heater wall. In this model, which was proposed by Kurul and Podowski (1990), it is assumed that the total heat flux can be decomposed into three components which are: surface quenching heat flux $q_q$, convective heat flux $q_c$ and microlayer evaporation heat flux $q_e$.

$$\dot{q}_{wall} = \dot{q}_q + \dot{q}_c + \dot{q}_e \tag{36}$$

$\dot{q}_{wall}$ is used in determining the boiling or surface heat transfer coefficient $h_s$ given as:

$$h_s = \frac{\dot{q}_{wall}}{T_w - T_{sat}} \tag{37}$$

The surface quenching heat flux, which accounts for the transient conduction that occurs when the liquid contacts the heater surface, is given as:

$$\dot{q}_q = \frac{2C_{wt}}{\sqrt{\pi}} f A_q \sqrt{t_w \lambda_l \rho_l C_{p,l}} (T_w - T_l) \tag{38}$$

Where $C_{wt}$ is the bubble waiting time coefficient, $f$ is bubble departure frequency, $t_w$ is bubble waiting time, $\lambda_l$ is the thermal diffusivity $T_w$ is the temperature of the heater

surface, $T_l$ denotes the liquid temperature and $A_q$ is the fraction of heater surface area that is subject to quenching given according to Del Valle and Kenning (1985) as:

$$A_q = \min\left(1, N_w K_{DK} \frac{\pi d_b^2}{4}\right), \qquad K_{DK} = 4.8 \exp\left(-\frac{\rho_l C_{p,l}(T_{sat} - T_l)}{80 \rho_v h_{lg}}\right)$$

Where $N_w$ is the nucleation site density, $d_b$ is the bubble departure diameter, and $h_{lg}$ is the latent heat.

The heat flux arising from turbulent convection can be determined using the Stanton number:

$$\dot{q}_c = (1 - A_q) St \rho_l C_{p,l} u_l (T_w - T_l) \tag{39}$$

In which $u_l$ is the velocity of the adjacent liquid, and Stanton number is defined as:

$$St = \frac{Nu}{RePr} \tag{40}$$

Where $Nu$ and $Pr$ are the Nusselt's and the Prandtl number, respectively.

The evaporation heat flux which takes place during nucleate boiling is given as follows:

$$\dot{q}_e = \frac{\pi}{6} {d_b}^3 \rho_v f N_w h_{fg} \tag{41}$$

The nucleation site density by Lemmert and Chawla is expressed as follows:

$$N_w = [210(T_w - T_{sat})]^{1.805} \tag{42}$$

The bubble departure diameter, according to Kocamustafaogullari and Ishii, is written as:

$$d_b = 0.0012 \left(\frac{\rho_l - \rho_v}{\rho_v}\right)^{0.9} 0.0208\theta \sqrt{\frac{\sigma}{g(\rho_l - \rho_v)}} \tag{43}$$

However, since these expressions were developed to be applied to conventional fluids, it is not certain if they can also be applied to nanofluids. The pool boiling section discussed that the heat flux depends on the number of nucleation sites and bubble departure diameter and frequency, which are all dependent on the surface roughness.

The models provided in ANSYS to calculate the bubble departure diameter are by Tolubinski-Konstanchuk, Unal, and Kocamustafaogullari-Ishii, and the models for nucleation site density are by Lemmert Chawla and Kocamustafaogullari-Ishii. However, none of these models accounts for the surface roughness and nanoparticle size, as can be seen from the expressions in Eq. 43 and Eq. 44. Therefore, for nucleation site density $N_w$, the following model by Benjamin and Balakrishnan (1997) needs to be used when only base fluid is being used:

$$N_w = 218.8 Pr^{1.63} \gamma^{-1} Rn^{-0.4} (T_w - T_{sat})^3 \tag{44}$$

$$\gamma = \sqrt{\frac{k_p \rho_p Cp_p}{k_f \rho_f Cp_f}}, \qquad Rn = 14.5 - 4.5\left(\frac{R_a P}{\sigma_f}\right) + 0.4\left(\frac{R_a P}{\sigma_f}\right)^2$$

Where $P$ and $R_a$ are the system pressure and surface roughness, respectively. Moreover, when nanofluids are being used, the modified Benjamin and Balakrishnan (1997) model by Li *et al.* (2015) should be used:

$$N_w = 512 Pr^{1.63} \gamma^{-1} Rn^{-0.4} \theta^{*1.2} F \left(\frac{R_a}{d_p}\right)^{0.4} (T_w - T_{sat})^3 \tag{45}$$

$$\theta^* = \frac{1 - cos(\theta_{nf})}{1 - cos(\theta_{bf})}, \qquad F\left(\frac{R_a}{d_p}\right) = \begin{cases} 0.275\left(\frac{R_a}{d_p}\right)^{-1.2} & 0 < \frac{R_a}{d_p} < 1 \\ 0.275 + 0.791\left(\frac{R_a}{d_p} - 1\right)^{0.68} & \frac{R_a}{d_p} \geq 1 \end{cases}$$

Where $\theta_{bf}$ and $\theta_{nf}$ represent the angle of contact on the clean and nanolayer coated surface, respectively. The bubble departure diameter model $d_b$ by Golorin *et al.* (1978) is given as:

$$d_b = \frac{1.65 d^* \sigma_{nf}}{g(\rho_l - \rho_v)} + \left[\frac{15.6 \rho_l}{g(\rho_l - \rho_v)}\right]^{\frac{1}{3}} \left[\frac{\beta_d k_l (T_w - T_{sat})}{\rho_v h_{lv}}\right]^{2/3} \tag{46}$$

Where for water, $d^* = 6\,\mu m$ and $\beta_d = 6$. Cole (1960) present in ANSYS can use the bubble departure frequency model. These equations will be input to ANSYS as UDFs. The Cole expression may be used for bubble departure frequency:

$$f = \sqrt{\frac{4g(\rho_l - \rho_v)}{3d_b\rho_l}} \tag{47}$$

## 3.5 Interfacial mass

The mass transfer rate in Eq. 21 happens at two different regions, near the heater surface and in the bulk liquid. Therefore, the mass transfer rate near the heater surface was calculated as:

$$\dot{m}_{vl} = \frac{\dot{q}_e}{h_{lv} + Cp_l(T_{sat} - T_l)} \tag{48}$$

The mass transfer in the bulk liquid

$$\dot{m}_{lv} = \frac{\dot{q}_l + \dot{q}_v}{h_{lv}} \tag{49}$$

$$\dot{q}_l = \frac{k_l Nu_l}{d_b}(T_{sat} - T_l);\ \ \dot{q}_l = \frac{\alpha_v \rho_v Cp_v}{\delta_t}(T_{sat} - T_v)$$

Where time scale $\delta_t$ was set equal to 0.05 according to Minocha *et al.* (2016) and the Nusselt number $Nu_l$ on the heater surface was calculated using Ranz and Marshall correlation available in ANSYS Fluent as:

$$Nu_l = 2 + 0.6Re_l^{1/2}Pr_l^{1/3} \tag{50}$$

## 3.6 Solution and Assumptions

Numerical models considered in this study are created in 2D via Space Claim and meshed with quadrilateral cells where possible using the meshing tool available in ANSYS. For pressure-velocity coupling, a phase-coupled SIMPLE scheme was selected. Second-order upwind scheme was selected for pressure, energy, momentum, turbulent kinetic energy, and turbulent dissipation rate. The gradients were calculated using the least square cell-based method, whereas modified HRIC method was used for volume fraction. The simulation was considered converged when the scaled residuals reached a minimum of $10^{-4}$, and insignificant change was noted in the vapour volume fraction, heater temperature, and heat flux.

The default value for the courant number is 200, while for momentum and pressure, it is 0.75. In this study, the courant number was reduced to 10, whereas values of 0.55 and 0.25 were set for momentum and pressure relaxation. In addition, the relaxation factor for turbulent terms was set to 0.3, and for the rest, it was set to 0.6 except for energy which was left at the default of 1.

The solution was initialized with the liquid temperature at saturation temperature (373 K) and 0 vapour volume fraction.

The following assumptions hold:

- The simulations contain the turbulent flow and are transient.
- The properties of the liquid and gas are assumed to be constant.
- Nanofluid was modelled as liquid water with modified properties as listed in section 2.1.2.
- The Khanafer and Vafai (2011) model calculates nanofluid thermal conductivity.
- The nanoparticles do not influence the properties of water vapour.
- The saturation temperature of the nanofluid was the same as the bulk fluid.
- A time step of $10^{-3}$ was used with 20 iterations per time step.

## 3.7 Setup

- Multiphase

An inhomogeneous, Eulerian model was used with 2 Eulerian phases, nanofluid and water vapour. Boiling model was used for Eulerian Parameter with boiling model option set to RPI Boiling model and formulation set to implicit. The mass transfer mechanism was set as boiling at a saturation temperature of 100 °C. The force setup was selected according to interfacial force section with wall adhesion, surface tension modelling turned on, and heat transfer coefficient selected according to Ranz-Marshall. The bubble waiting time coefficient has been modified to correct the departure time between consecutive bubbles during nucleate boiling.

- Energy

Energy option was selected since heat transfer, and change in temperature was involved.

- Viscous model

the k-ε realizable model was used with enhanced wall functions and turbulence multiphase model as a mixture. The wall function requires the y+ to be less than 5; thus, the mesh was refined near the heater to achieve this.

- Materials

Water-liquid was chosen, and its properties are manually modified according to nanofluid properties section. Water-vapour was chosen for the steam and copper for the boundary conditions.

- Wall function

Wall function is needed to capture the gradients near the wall accurately. This was done by modifying the viscosity when calculating the wall shear stress. The wall shear stress, $\tau_w$, is given by:

$$\tau_w = -\rho v \frac{\partial U}{\partial y}_{y=0} \tag{51}$$

Where U is the velocity. But in CFD, the velocity profile is linear:

$$\tau_w = -\rho v_w \frac{U_p}{y_p}$$

Where $v_w$ is the modified viscosity, also known as effective wall viscosity and $U_p$ and $y_p$ are the incremental velocity and cell height, respectively. The real velocity profile can be said to be given as:

$$U^+ = f(y^+) = -\frac{U \rho u_t}{\tau_w} \tag{52}$$

Where $U^+$ is the non-dimensional velocity and $u_t$ is the friction velocity. Thus, the real wall shear stress is written as:

$$\tau_w = -\frac{U_p \rho u_t}{f(y^+)} \tag{53}$$

Hence, by rearranging Eq. 52 and Eq. 54, $v_w$ can be expressed as:

$$v_w = \frac{y_p u_t}{f(y^+)} = v\left(\frac{y^+}{f(y^+)}\right) \tag{54}$$

For enhanced wall function:

$$f(y^+) = e^{\Gamma} u^+_{lam} + e^{\frac{1}{\Gamma}} u^+_{turb} \qquad \Gamma = -\frac{0.01(y^+)^4}{1+5y^+} \tag{55}$$

Where $e^{\Gamma}$ and $e^{\frac{1}{\Gamma}}$ are blending functions. This means that the enhanced wall function blends between the laminar and turbulent solution, which allows it to be more accurate than the standard wall function in the buffer region of $5 \leq y^+ \leq 30$. It is worth noting that at $y^+$ of around 5, there is a large deviation of $v_w/v$ from what is predicted by direct numerical solution (DNS). Thus, it is best to keep $y^+ \leq 2$.

From this, the effective wall viscosity can be calculated and be used in the place of shear viscosity in Eq. 23.

# 4. VALIDATION OF NUMERICAL MODEL

In this section, the experiment done by Harish et al. (2011) is used to validate the model. A 2D domain is used for simplicity consisting of a flat horizontal plate heater. A quad mesh was used with finer mesh near the heating surface. A mesh sensitivity analysis was performed to understand the dependence of results on the mesh size. It was found that any mesh finer than 12000 elements showed insignificant changes in the results. Therefore, a mesh with 12000 elements was used to minimize computation time for the validation.

## 4.1. Geometry and boundary conditions

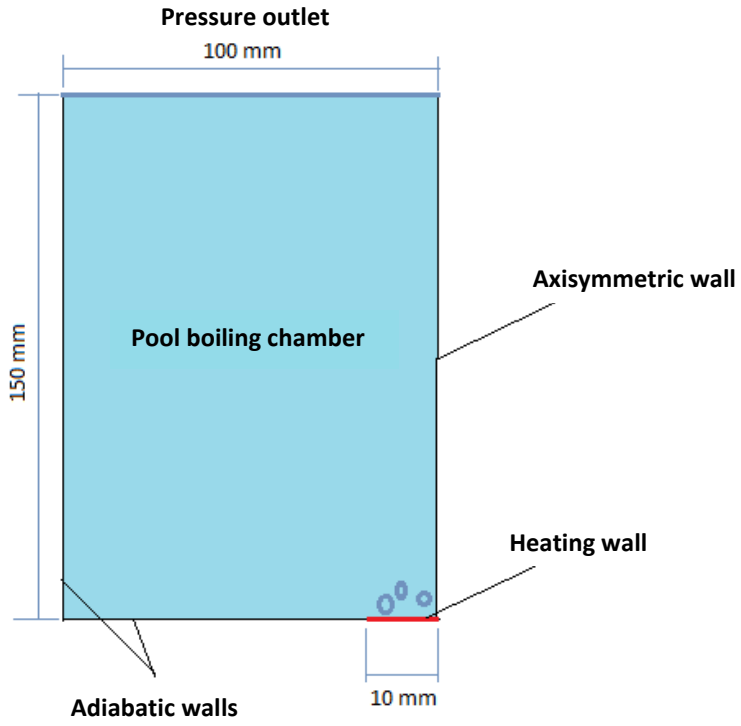


***Figure 19*** *Geometry and boundary condition used for validation.*

The pool boiling chamber used in Harish et al. (2011) was a 200 mm diameter glass cylinder, and the heating wall was a 20 mm diameter disk. For this reason, half of the domain can be simulated with an axisymmetric wall condition, as illustrated in Figure 19. Furthermore, the axisymmetric model appropriately reduces computation time since only half the grid will be solved. The boundary condition is as follows: the side walls are made adiabatic to represent well insulated walls, the top is a pressure outlet which represents being open to atmosphere, an axisymmetric wall condition is applied as shown, and the heated wall is given a temperature boundary condition.

The heating element used had a rating of 750 W connected to the heater plate and the walls were sufficiently insulated during their experiment using glass wool. The material of the disk was aluminium with an area of 314mm$^2$. Their T-type thermocouple was embedded in a hole that was 2 mm in depth. The nanofluid used by them was $Al_2O_3$/water and was boiled at saturation temperature. The height of the chamber was not given by the authors thus a height of 150mm was used and ensured that the output parameters were not influenced by the height of the chamber. It has been proven in many studies that an axisymmetric model closely mimics the results obtained from a

3D model while keeping computation time at a minimum. For this reason, the axisymmetric model was used to represent the 3D reality.

## 4.2. Validation results

The uncertainty in the heat flux as reported by the authors was ±4.74%. Figure 20 compares the results obtained from the simulation model against the experimental data. Since even with pure water, the nucleation site density is a function of surface roughness, the built-in functions in FLUENT such as Lemmert-Chawla cannot be used as they do not consider the surface roughness. Thus, Eq. 45 was used as UDF when calculating nucleation site density for pure fluids (0% vol.).

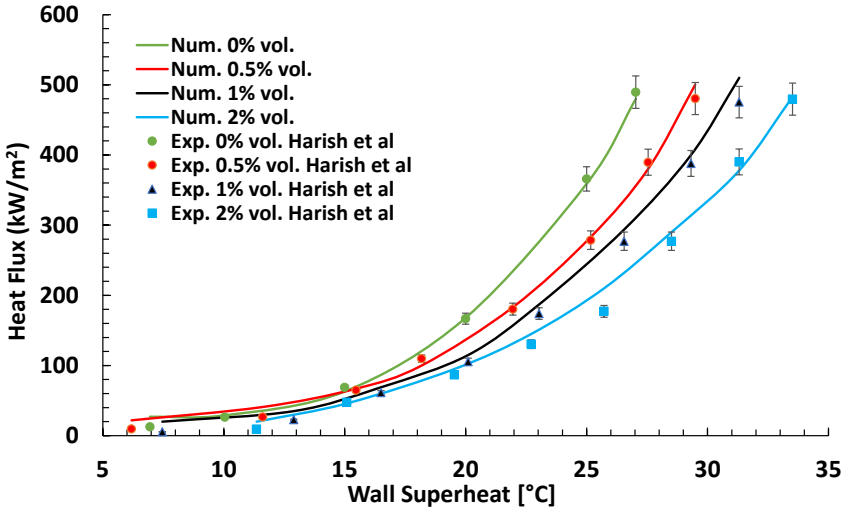


***Figure 20*** *Validation of the numerical model using different concentrations of $Al_2O_3$ /water nanofluid.*

As shown in Figure 20, there is a good correlation between the numerical and the experimental results. With the validation successfully completed, the model can confidently be used for further studies.

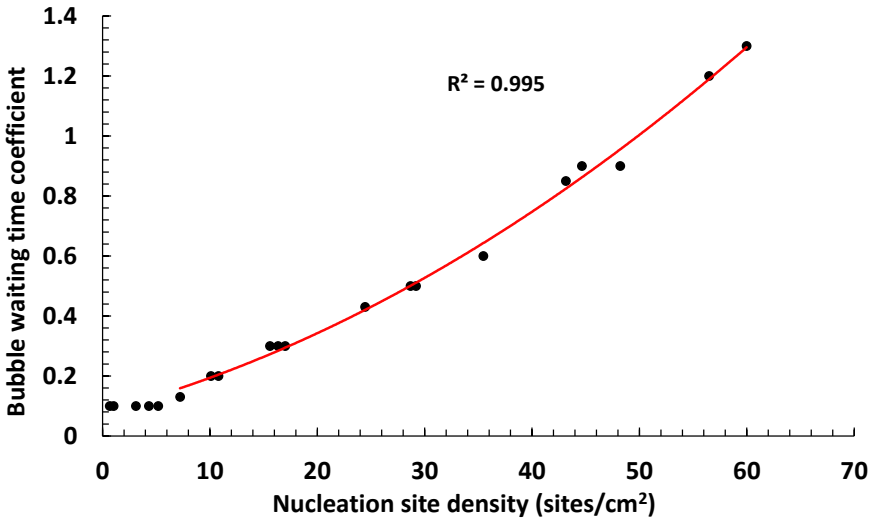


***Figure 21*** *Bubble waiting time coefficient vs nucleation site density.*

Figure 21 shows the bubble waiting time coefficient that was used at different nucleation site densities for nanofluid during validation. During validation study, the nucleation site density was calculated for each data point shown in Figure 20 and the respective bubble waiting time coefficient used to achieve the result was recorded and plotted in Figure 21. The red line then represents a fit for the correlation that was created in the present study as:

$$C_{wt} = 1.8382x10^{-4} * NSD^2 + 9.1398x10^{-3} * NSD + 8.684x10^{-2} \quad (56)$$

Where NSD is the nucleation site density in sites/cm$^2$. As default, this coefficient is set to 1 in Fluent and can be modified to correct the departure time between consecutive bubbles as also shown by. The bubble waiting time coefficient depends on various parameters such as surface roughness, fluid properties, and temperature of the liquid and the heating surface. All these parameters are incorporated into the nucleation site density in Eq. 46, and hence the bubble waiting time coefficient was plotted against it in Figure 21 so that the coefficient can be predicted for different cases.

A line of best fit was drawn for nucleation site density from 7 to 60 sites/cm$^{2,}$ which clearly shows a correlation between bubble waiting time coefficient and nucleation site density. A bubble waiting time coefficient of 0.1 was used when the nucleation site density was lower than 7 sites/cm$^2$ as this is the lowest value allowed by Fluent.

These bubble waiting time coefficients are for a horizontal disk heater, and it will be assumed that they are the same or similar for a heat sink. The assumption is

necessary since experimental data for nanofluid pool boiling with heat sink are difficult to find.

Since this study specifices a temperature boundary condition on the heater, there is enough information to accurately pre-calculate the nucleation site density from Eq. 46 for each case before starting the simulation. Thus, for the investigation in section 5, the bubble waiting time coefficient to be used for each case was calculated from Eq. 57 by first calculating the nucleation site density.

# 5. NUMERICAL INVESTIGATION

This section targets on investigating the coupled effect of surface roughness and particle size (SPIP) and the effect of nanoparticle concentration, type of base fluid, number of fins, and aspect ratio of fins on the heat transfer enhancement during pool boiling.

The contact angle on the clean surface is a function of the original surface roughness, while the contact angle on the nanocoated surface depends on both the concentration and original surface roughness, as shown by Harish et al. (2011). The contact angle is measured for specific roughness and concentration in experimental studies, which can be used for validation. However, in this investigation, a wider range of roughness and concentration will be considered, for which the contact angle measurements are unknown. Without the contact angles, the nucleation site density cannot be calculated.

One way to address this is to form a regression based on data from multiple experimental studies. For example, the following regression was derived to approximate the contact angle on the bare surface as a function of original surface roughness:

$$\theta_{bf} = 0.0002R_a^2 - 0.3256R_a + 115.9 \tag{58}$$

Where the surface roughness $R_a$ is in nanometres, valid from 50 nm to 700 nm, and the bare surface contact angle $\theta_{bf}$ is in degrees.

Similarly, a regression is derived to approximate the contact angle on the nanocoated surface $\theta_{nf}$:

$$\theta_{nf} = (333\varphi^2 - 15\varphi - 0.13)\theta_{bf} + \theta_{bf} \quad (59)$$

Using Eq. 58 and 59, the nucleation site density can now be calculated, and the coupled effect of surface roughness and particle size can be investigated.

## 5.1. Geometry and boundary conditions

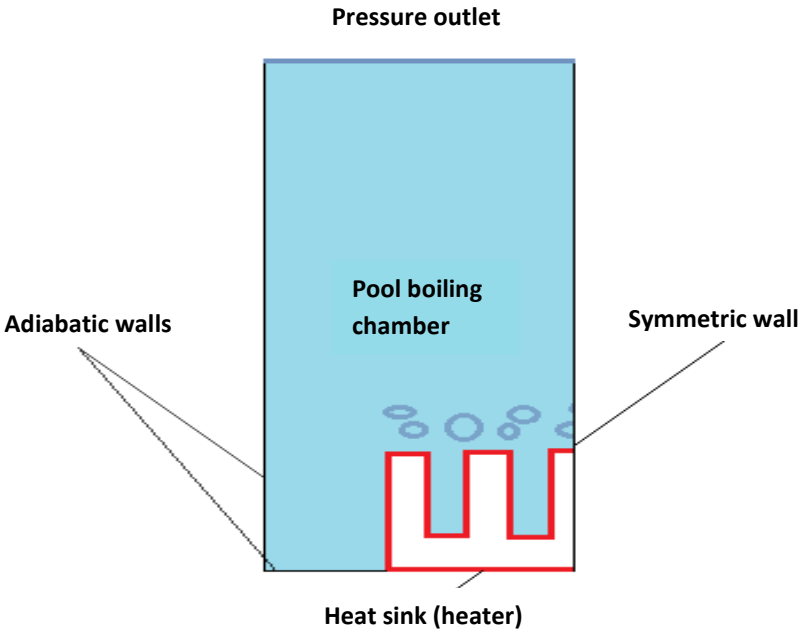


***Figure 22*** *Geometry and boundary condition used for investigation.*

Figure 22 shows the domain, geometry, and heated surface, which is the heat sink on a microprocessor. The boundary condition is as follows: the side walls are made adiabatic to represent well insulated walls, the top is a pressure outlet which represents being open to atmosphere, a symmetry wall condition is applied as shown, and the heat sink wall is given a temperature boundary condition. A symmetric boundary condition is also used to reduce computation time thanks to the symmetric geometry of the heatsink. The height and the width of the domain varies according to the aspect ratio and were selected by varying the distance of the pressure outlet and the side wall until the output parameters were not influence by the dimensions of the domain.

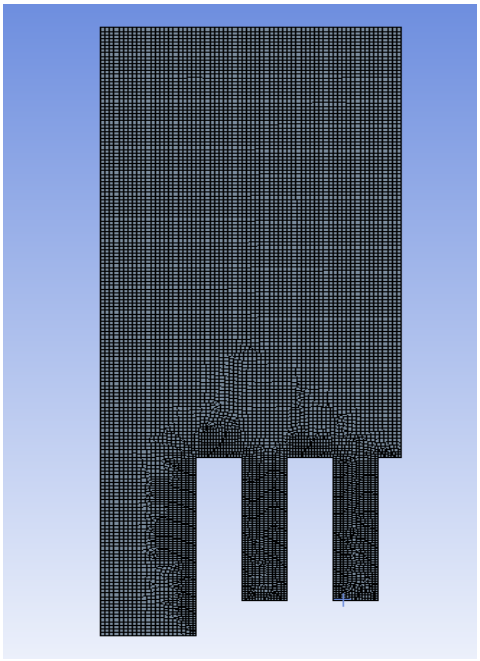

***Figure 23*** *Meshed study domain.*

As shown in Figure 23, the mesh was refined around the fins to achieve $y^+$ values less than 5 so that the enhanced wall function could be used. A mesh study was carried out to check the dependency of the results, such as surface heat flux and vapour fraction on the mesh size, as shown in Figure 24. Finally, a mesh with 11 186 elements was used as any mesh finer than this had less than 1% difference on the results, and any mesh finer led to divergence.

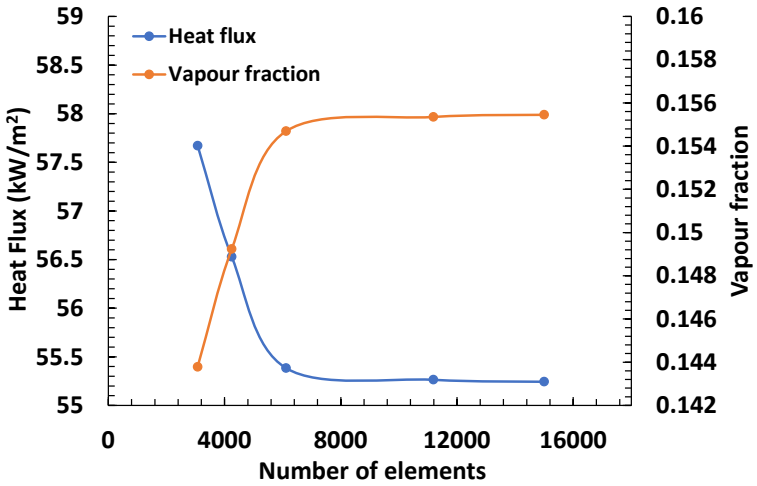


***Figure 24*** *Variation in critical parameters at different grid sizes.*

## 5.2. Effect of SPIP

The SPIP investigation was carried out using $Al_2O_3$/water at atmospheric pressure (101 kPa) and saturation temperature. The number of fins and fin aspect ratio was kept constant. SPIP ranging from 0.2 to 16 were considered (heat sink surface roughness range of 50nm to 700nm and particle diameter range of 43.75nm to 250nm). SPIP stands for surface-particle interaction parameter and defined as surface roughness divided by particle diameter. The values and the range of SPIP were first decided and incorporated in the numerical model by changing the $\frac{R_a}{d_p}$ value in Eq. 46. For instance, for SPIP 0.2, the $\frac{R_a}{d_p}$ term in Eq. 46 was replaced by 0.2.

Simulating pure water pool boiling using a heat sink will provide valuable information for comparison against nanofluid. Thus, pure water was also simulated using a surface roughness of 50nm.

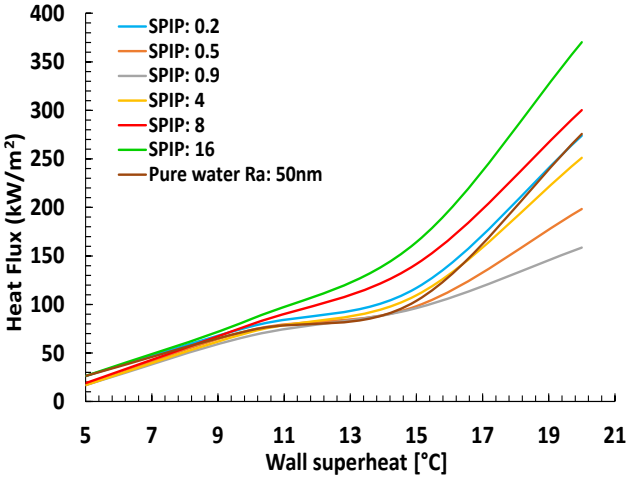


***Figure 25*** *Heat flux vs superheat at different SPIP, 2% vol.*

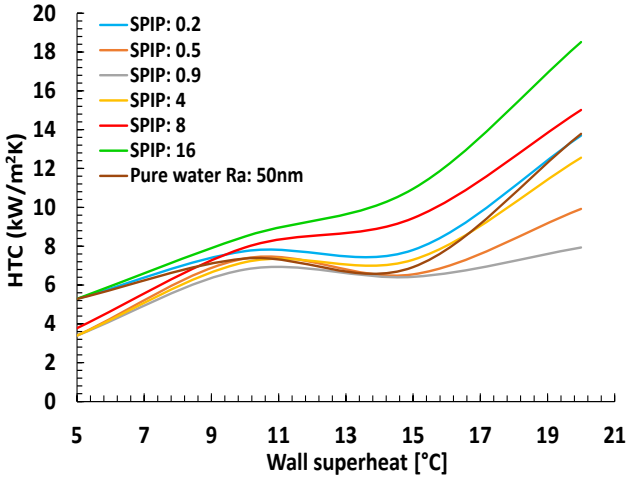


***Figure 26*** *HTC vs superheat at different SPIP, 2% vol.*

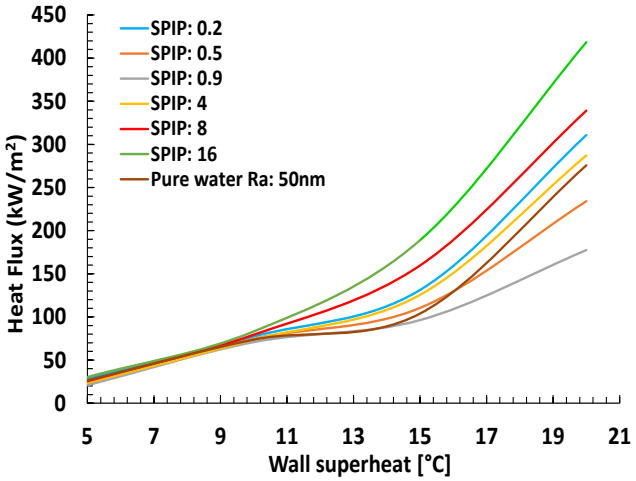


***Figure 27*** *HTC vs superheat at different SPIP, 1% vol.*

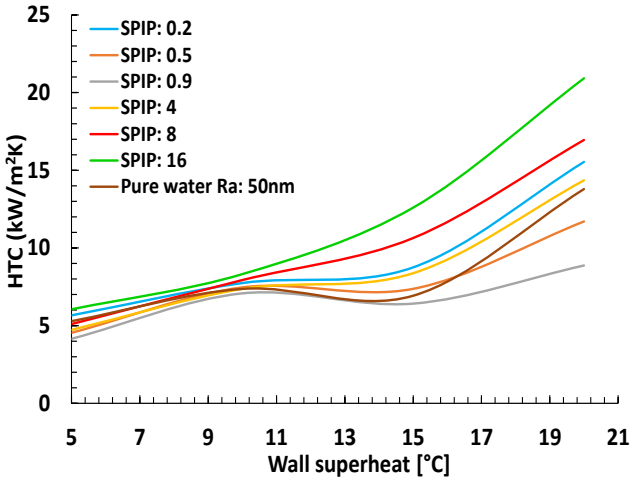


***Figure 28*** *HTC vs superheat at different SPIP, 1% vol.*

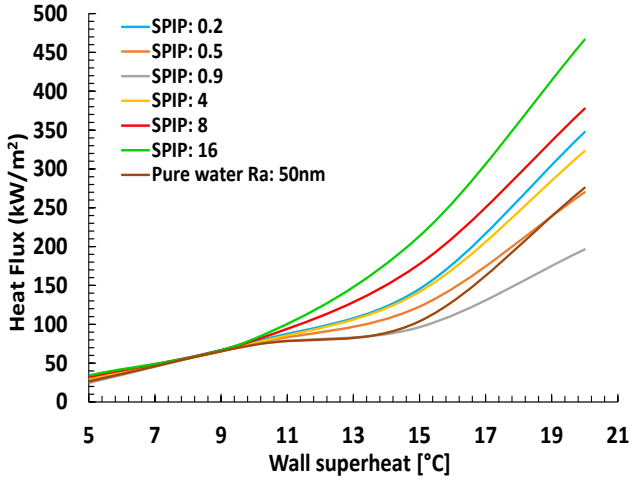


***Figure 29*** *HTC vs superheat at different SPIP, 0.5% vol.*

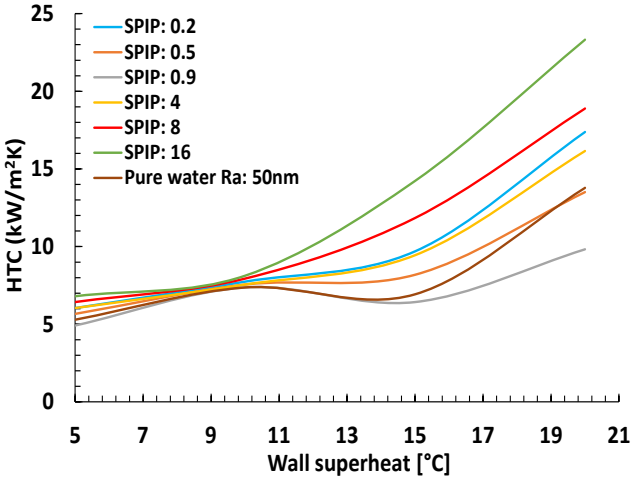


***Figure 30*** *HTC vs superheat at different SPIP, 0.5% vol.*

Figure 25 to Figure 30 compare the heat flux and HTC at different SPIP and concentrations. It is noticed that when the wall superheat is below 10°C, the variation in heat flux at different SPIP is not as pronounced as it is at higher superheat temperatures. What is common at all concentrations is that at higher superheats, the lowest heat flux (and thus lowest HTC) is achieved when the SPIP is 0.9 (closest to 1) and that the heat flux and HTC increase as SPIP moves away from 1. The highest heat flux is achieved at SPIP: 16 followed by SPIP: 8, 0.2, 4, 0.5 and lastly, SPIP: 0.9.

The reason why the heat flux is lower when SPIP is closer to 1 could be because the nanoparticles are of similar size to the surface cavities. When the particles deposit on the heater surface during boiling, they land on surface cavities where bubbles grow and clog them. Thus, reducing the nucleation site density and turbulence on the heater surface, and as a result, the HTC and heat flux decreases.

When the SPIP is higher than 1, the particles are smaller than the cavities. For this reason, the cavities cannot get clogged. Instead, when the particles land on the cavities, the same cavity is split into two or smaller cavities. This causes the nucleation site density to increase, which in turn increases the turbulence on the heater surface, and as a result, the HTC and heat flux increase. Conversely, when the SPIP is lower than 1, the particles are larger than the surface cavities and clog fewer cavities than when SPIP is near 1.

It is also evident from the figures that at 2% vol. concentration, HTC deterioration is noticed at SPIP 0.9, 0.5, and 4 compared to pure water. At 1% vol. concentration, HTC deterioration is seen at SPIP 0.9 and 0.5 compared to pure water, whereas at 0.5% vol. concentration, deterioration is only seen at SPIP 0.9.

The figures also show that although the heat flux increases with temperature for all cases, the HTC for pure water decreases from wall superheats of 10 to 15 °C. HTC deterioration at this wall superheat range is also seen for SPIP 0.9 at all concentrations, for SPIP 0.5 at 1% and 2% vol. concentration, and for SPIP 0.2 and 4 at 2% vol. concentration. This could be because although the nucleation site density increases with wall superheat temperature, it doesn't increase enough to counter the effect of increased vapour formation on the heater surface, and so the increase in heat flux as the superheat temperature increases from 10 to 15 °C is relatively low which then translates to a decrease in HTC.

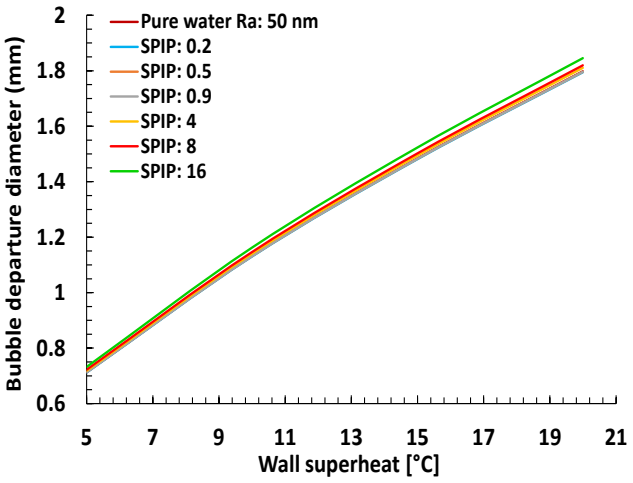


***Figure 31*** *BDD vs superheat at different SPIP, 2% vol.*

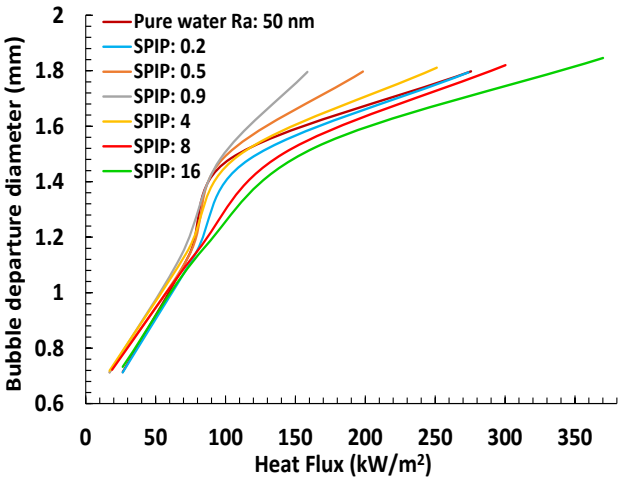


***Figure 32*** *BDD vs heat flux at different SPIP, 2% vol.*

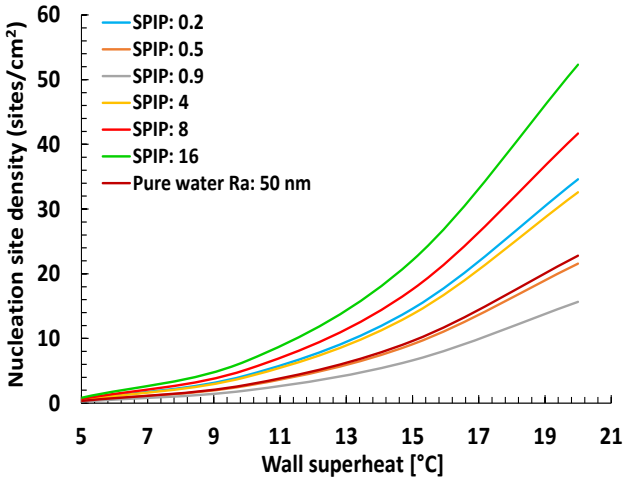


***Figure 33*** *NSD vs superheat at different SPIP, 2% vol.*

The bubble departure diameter was calculated using Eq. 47. This equation was imported into Fluent as UDF and returned calculated figures based on the values of parameters on the surface of the heater. Figure 31 shows that as the wall superheat increases, the bubble departure diameter also increases. It can be noticed that there is a very slight variation in departure diameter at different SPIPs. From this figure, it can be said that the bubble departure diameter is almost the same across different SPIP at a fixed superheat temperature.

For a better comparison, bubble departure diameter was plotted against heat flux (Figure 32), where the same SPIP order is seen again. At the same heat flux, the bubble departure diameter is smallest at SPIP 16 and greatest at SPIP 0.9. Smaller bubble departure diameter means that more bubbles can grow from the same area and thus have a higher nucleation site density, as shown in Figure 33.

Figure 33 compares the nucleation site density at different SPIP. From these figures, it can be confirmed that indeed the nucleation sites increase when SPIP is away from 1 and decrease when it is closer to 1. It can also be deduced that the highest nucleation site density is achieved at SPIP 16 followed by SPIP 8, 0.2, 4, 0.5, and lastly, SPIP 0.9. The same order was seen when comparing heat flux which proposes that heat flux greatly depends on the nucleation site density.

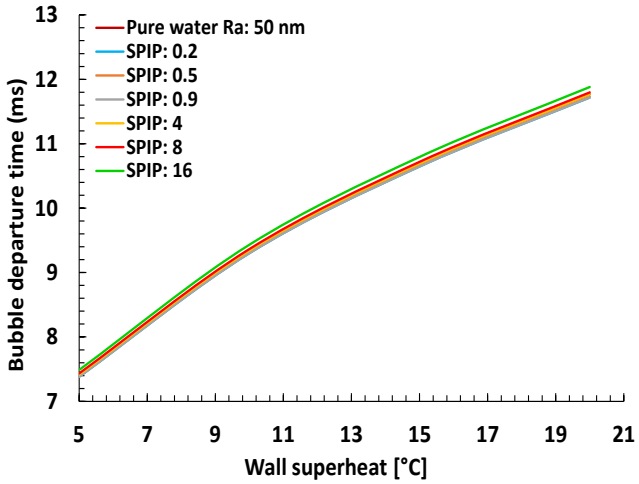


***Figure 34*** *BDT vs superheat at different SPIP, 2% vol.*

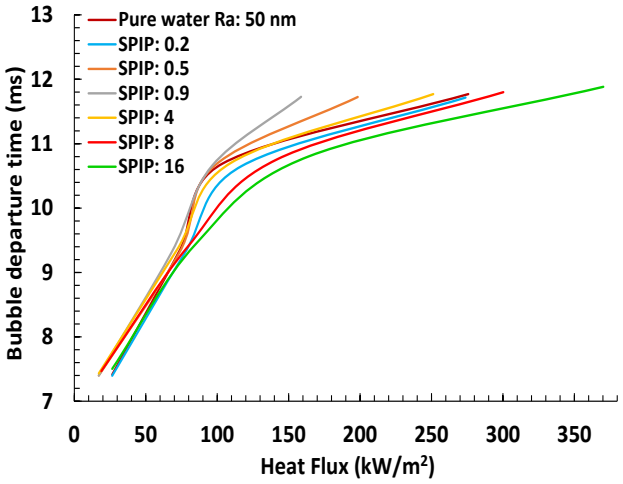


***Figure 35*** *BDT vs heat flux at different SPIP, 2% vol.*

Figure 34 and Figure 35 show the plot of bubble departure time, which is the time between two consecutive bubbles leaving the heated surface from the same nucleation site against wall superheat and heat flux, respectively and was calculated as the inverse of bubble departure frequency in Eq. 48. It can be immediately noticed that the departure time is almost equal at different SPIP at a constant superheat temperature. However, differences in bubble departure time are seen at different SPIP at a constant heat flux. For example, the lowest departure time is achieved at SPIP 16, and the highest is seen at SPIP 0.9.

This could be since SPIP 0.9 has the largest bubble departure diameter, they take longer to grow, leading to an increase in the interval between the two consecutives bubbles. Similarly, it was shown that SPIP 16 has the smallest bubble departure diameter. Hence, the bubbles take the shortest time to grow, leading to a smaller time difference between consecutive bubbles.

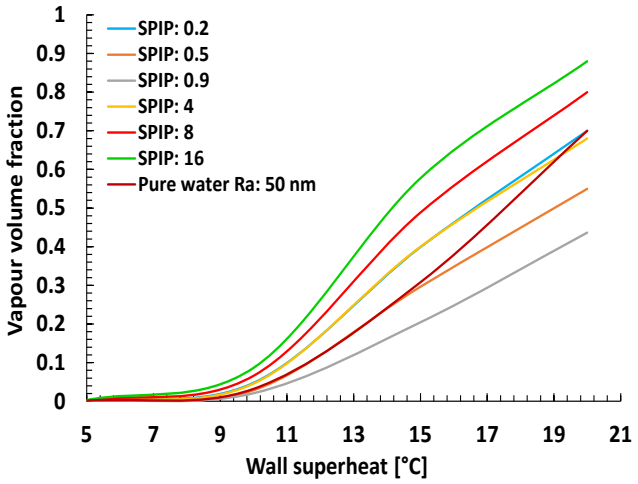


***Figure 36*** *Vapour fraction vs wall superheat, 2% vol.*

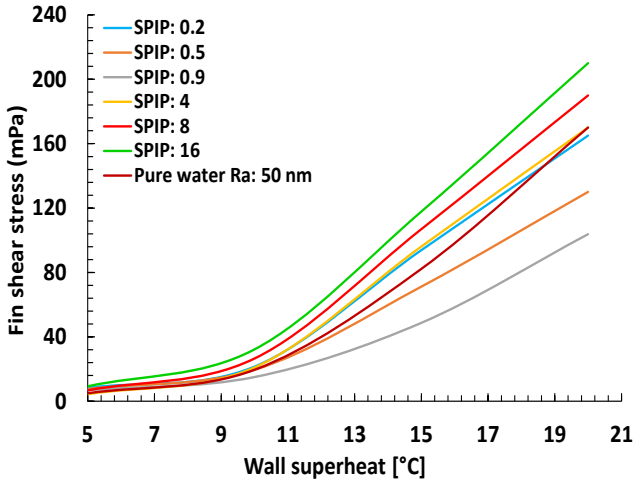


***Figure 37*** *Fin shear stress vs wall superheat, 2% vol.*

Regarding vapour volume fraction on the heater surface, it is the highest at SPIP 16 and the lowest at SPIP 0.9 (Figure 36). Again, this is because of the high heat flux. Since the heat flux is higher at SPIP 16, more heat is available to vaporize water faster, so more vapour is seen on the heater surface.

The liquid fin shear stress is also highest at SPIP 16 and lowest at SPIP 0.9 (Figure 37). At SPIP 16, the particle size is the smallest, leading to the nanofluid's highest viscosity. This could be one of the reasons why at SPIP 16, larger average liquid fin shear stress values are seen. It could also be that the high nucleation site density at SPIP 16 increases the turbulence on the heater surface. As a result, the liquid velocity gradient on the heater surface is higher, contributing to higher shear stress.

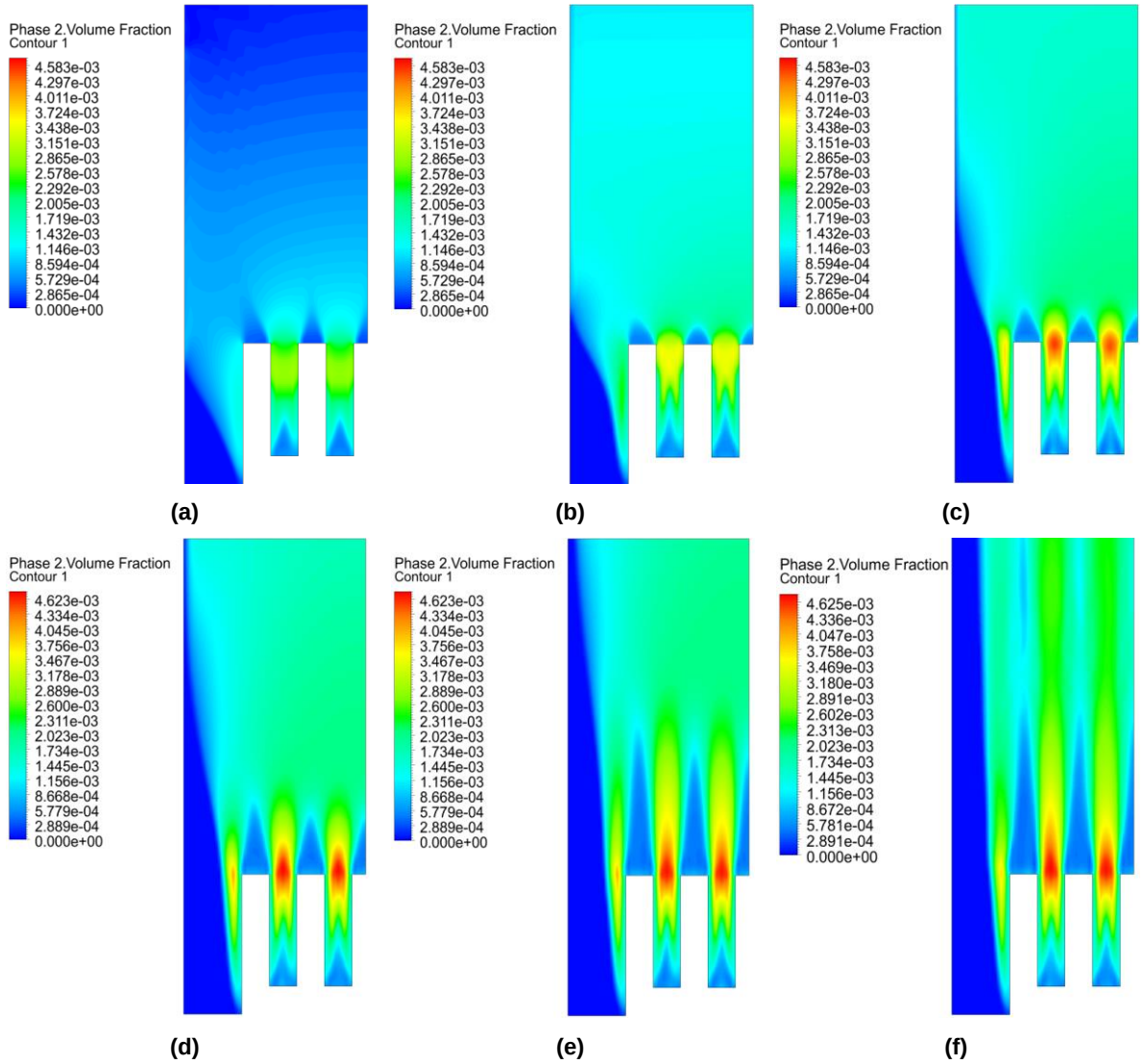


***Figure 38*** *Vapour fraction contours, fin aspect ratio 4 (a) 0.2 sec. (b) 0.6 sec. (c) 1.0 sec. (d) 1.5 sec. (e) 2.0 sec. (f) 2.5 sec.*

The vapour fraction contours are shown in Figure 38 at different times during the boiling process. Initially, and as expected, there is very little vapour formation, and as time progresses, the vapour fraction increases. It can be noticed that there is a triangular region over the top face of each fin where very little vapour is present. The triangular region only increases with time despite the fins' top faces being heated. There is also a smaller triangular region between two fins at the bottom where less vapour is seen. This region, however, does not increase with time. Interestingly, the highest vapour fraction is achieved at the region between the top faces of the two fins where the vertical section of the fin ends. This tells us that the vertical sections of the fins produce a larger amount of vapour as compared to horizontal sections of the fins.

## 5.3. Effect of concentration

This section investigates the effect of particle concentration on the total heat flux and compares it to using pure water. The concentration was varied from 0.5% vol. to 2% vol. The nanofluid used is $Al_2O_3$/water, and the fin aspect ratio and the number of fins were kept constant.

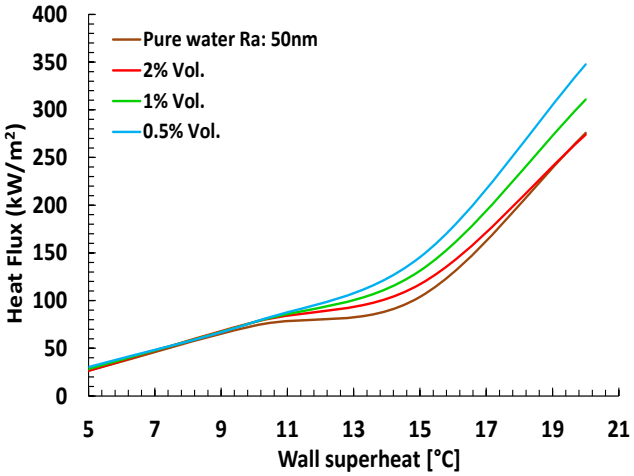


***Figure 39*** *Heat flux vs superheat at various concentrations, SPIP: 0.2.*

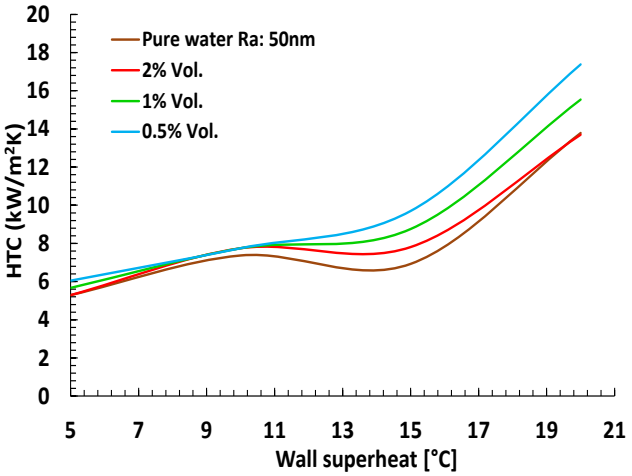


***Figure 40*** *HTC vs superheat at various concentrations, SPIP: 0.2.*

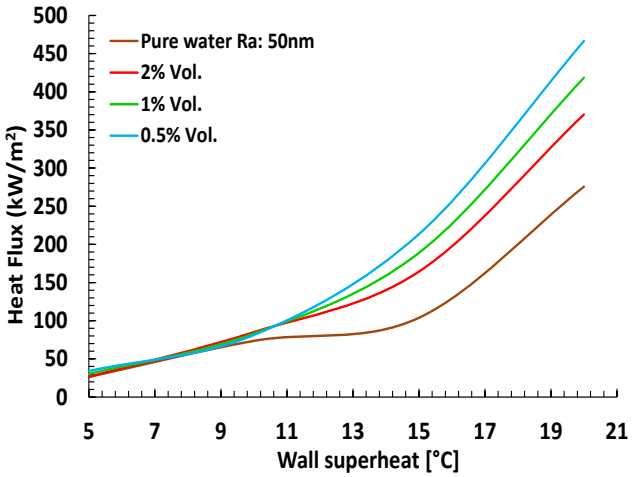


***Figure 41*** *Heat flux vs superheat at various concentrations, SPIP 16.*

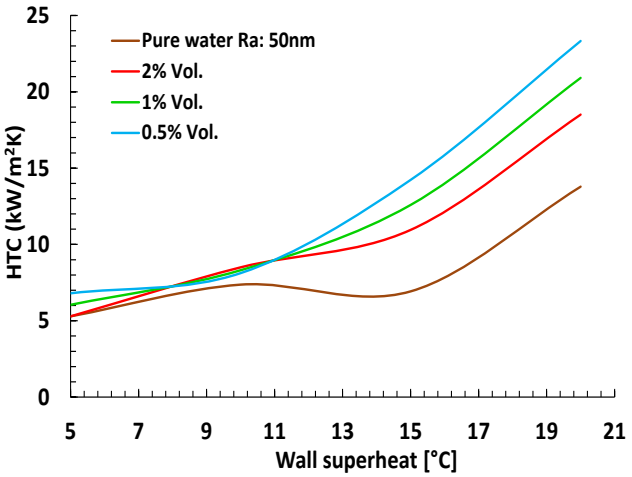


***Figure 42*** *HTC vs superheat at various concentrations, SPIP 16.*

From Figure 39 to Figure 42, it is evident that the heat flux and the HTC decrease as the concentration increases. This trend is observed at all SPIP. The reason could be that the particle deposition thickness increases with an increase in particle concentration, increasing the thermal resistance on the heater surface. This effect is incorporated in the nucleation site density equation (Eq. 46), and hence the behaviour is seen in the numerical model. In effect, there are two reasons for the decrease in HTC with an increase in concentration. One being due to the increase in thermal

resistance formed by the nanoparticle deposition layer where the heater is blanketed by the nanoparticle layer making it difficult for the liquid to come into contact with the heater to carry away the heat. The HTC deterioration due to deposition becomes more and more significant as the deposition thickness increases and could easily be the dominant cause for the HTC deterioration. According to Seong *et al.* (2014), the order of deposition coating is around 10 microns. The second reason being that as the concentration and deposition increases, the nucleation sites become covered and blocked.

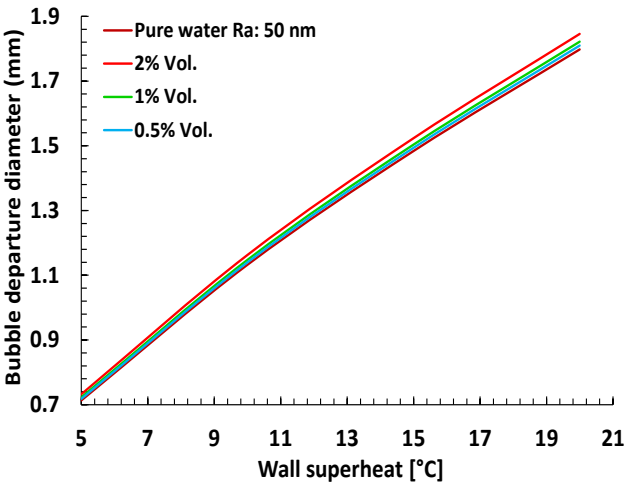


***Figure 43*** *BBD vs superheat at various concentrations, SPIP 16.*

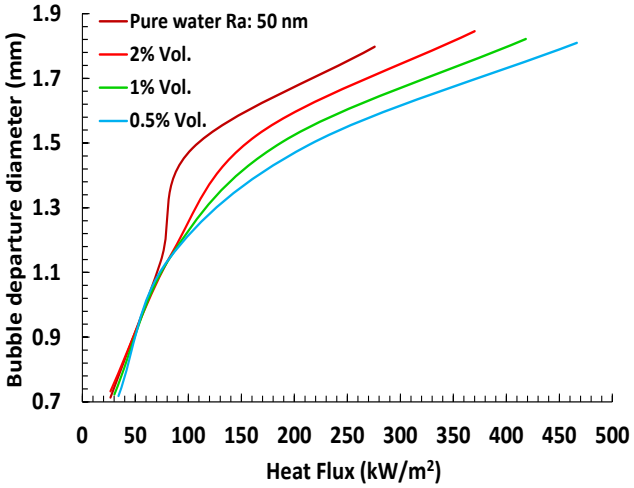


***Figure 44*** *BBD vs heat flux at various concentrations, SPIP 16.*

Figure 43 and Figure 44 compare the bubble departure diameter versus wall superheat and heat flux, respectively. Again, the variation in bubble departure diameter at different concentrations is very small at a fixed temperature. It is worth noting that pure water has the smallest bubble departure diameter at a fixed temperature compared to nanofluids, whereas if the comparison is made at a fixed heat flux, pure water has the highest bubble departure diameter.

The graphs suggest that as the temperature and heat flux increase, the bubble departure diameter also increases. Also, as the concentration increases, so does the bubble departure diameter. According to Eq. 47, the bubble departure diameter depends on the nanofluid density, surface tension, and thermal conductivity, which all increase as the nanoparticle concentration increases.

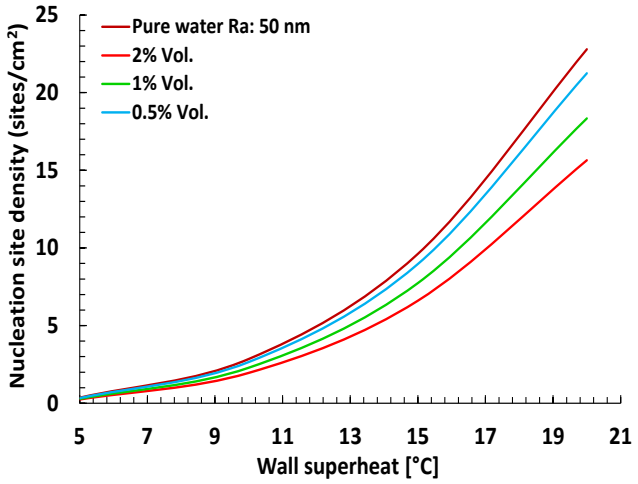


***Figure 45*** *NSD vs superheat at various concentrations, SPIP 0.9.*

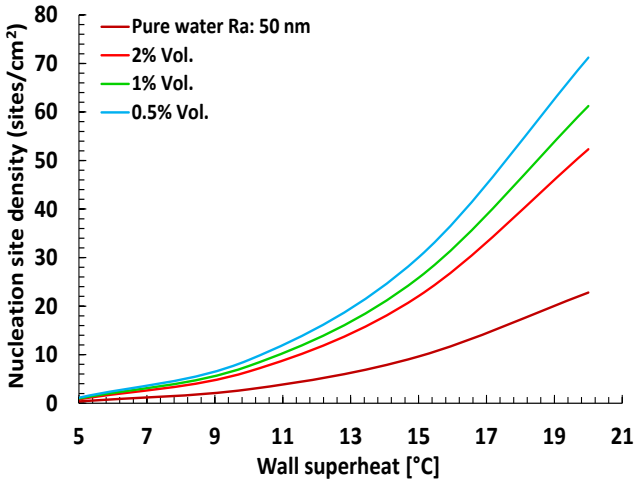


***Figure 46*** *NSD vs superheat at various concentrations, SPIP 16.*

Similarly, a comparison is shown for nucleation site density at different concentrations in Figure 45 and Figure 46 where the nucleation site density increases as the concentration decrease. This could be because the increased particle deposition covers up the surface cavities, reducing nucleation sites. Another reason could be that higher concentration leads to lower contact angle, and thus the wettability increases, which causes the nucleation site density to decrease. For this reason, although the thermal conductivity increases with concentration, the heat flux decreases. Once again, these effects are incorporated into Eq. 46 and thus also shown in the numerical model.

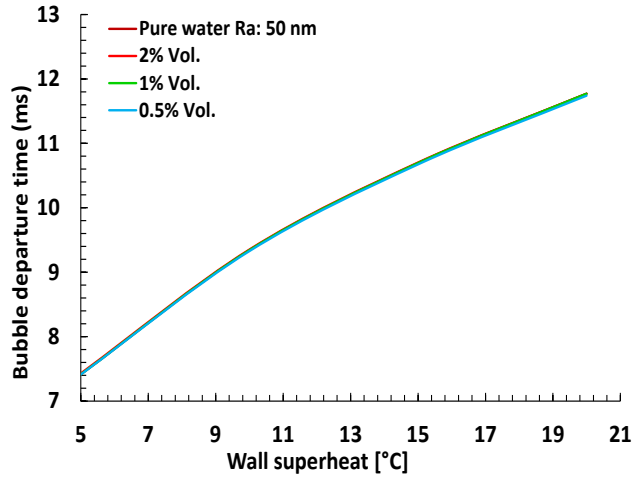


***Figure 47*** *BDT vs superheat at various concentrations, SPIP 4.*

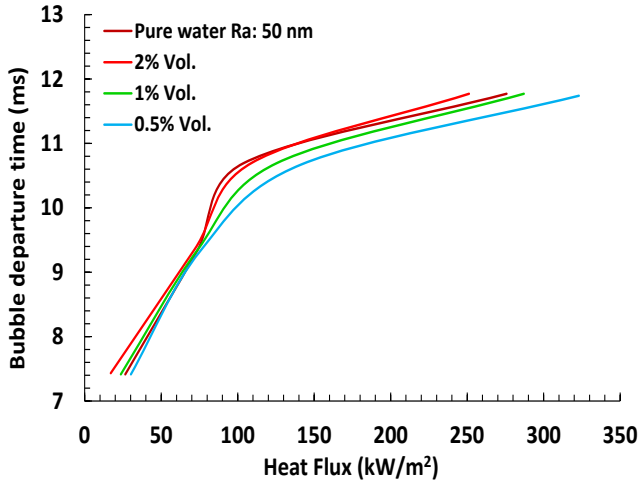


***Figure 48*** *BDT vs heat flux at various concentrations, SPIP 4.*

The bubble departure time at a constant superheat temperature is nearly identical at all concentrations (Figure 47), whereas, at a constant heat flux, the bubble departure time increases with concentration (Figure 48). This, again is due to the bubble

departure diameter. The bubble departure diameter increases with concentration and since larger bubbles take a longer time to grow and detach from the heated surface, the departure time is increased.

As the concentration increases and SPIP goes near 1, the nucleation site density decreases, suggesting that the lower the nucleation site density, the more enhanced the dip in HTC is at wall superheat of 10 to 15 °C. As mentioned in the previous section, this could be because the increase in nucleation site density at wall superheat of 10 to 15 °C is not high enough to counter the effect of increased vapour formation on the heater surface. Therefore, at lower concentrations and when SPIP is away from 1, the rate of increase in nucleation site density is much higher than when the concentration is high and SPIP is near 1. For this reason, the dip in HTC at wall superheat of 10 to 15 °C is not seen or is less pronounced in the former case.

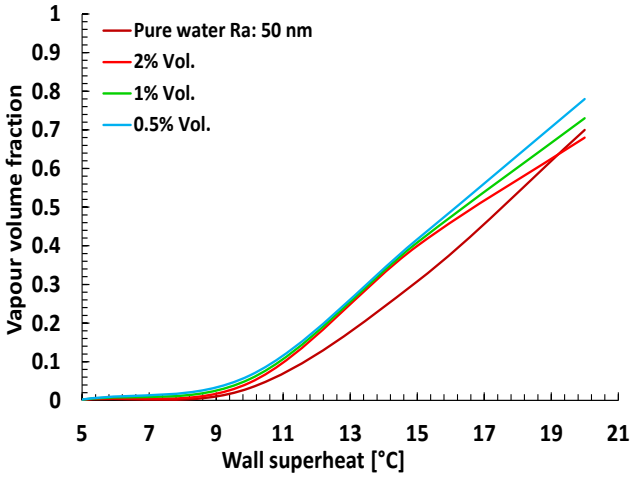


***Figure 49*** *Vapour fraction vs superheat at various concentrations, SPIP 4.*

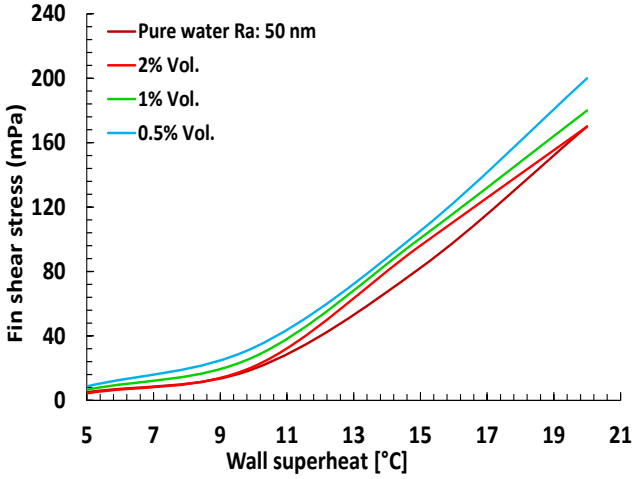


***Figure 50*** *Fin shear stress vs superheat at different concentrations, SPIP 4.*

The vapour volume fraction on the heater surface decreases as the concentration increases. This is because higher heat flux is achieved at lower concentrations, and due to a higher amount of heat being passed on to the liquid, a higher amount of vapour is produced. The fin shear stress also decreases as the concentration increases despite the viscosity increasing with concentration. This could mean that the surface liquid velocity gradient greatly increases as the concentration decreases. Nucleation site density also increases with a decrease in concentration, leading to more turbulence on the heater surface and could cause higher velocity gradients at the surface.

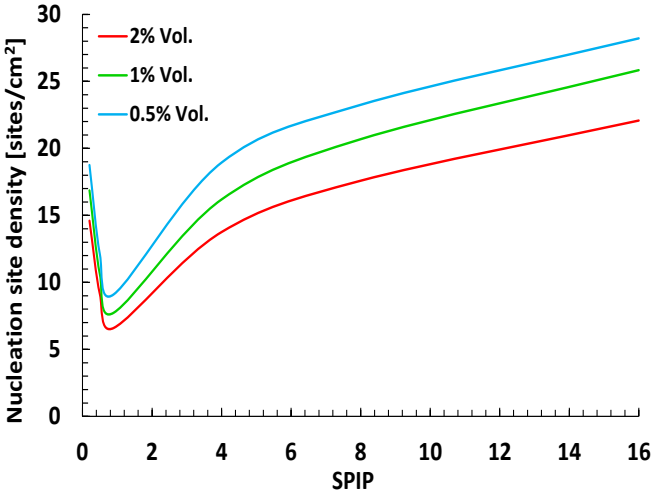


***Figure 51*** *NSD vs SPIP at different concentrations and 15 degrees superheat.*

From Figure 51, it can be seen that as the concentration increases, the nucleation site density decreases due to the cavities being covered. The decrease in nucleation sites may also indirectly account for the increased thermal resistance offered by the deposition. As expected, we can see that the nucleation site density drops to its minimum as it approaches SPIP 1 due to the clogging of nucleation sites and increases as it moves away from SPIP 1 due to multiplication of nucleation sites.

## 5.4. Effect of aspect ratio

The effect of the fin aspect ratio is investigated in this section. The aspect ratio is defined as the height divided by the width of the fin. Aspect ratios of 0.2, 0.6, 2 and 4 are considered with $Al_2O_3$/water as the nanofluid. The fin spacing, number of fins, and concentration were kept constant.

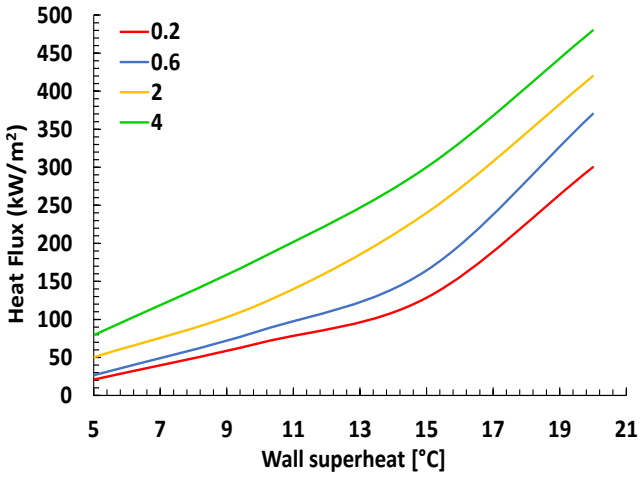


***Figure 52*** *Heat flux vs superheat at various aspect ratios, SPIP: 16.*

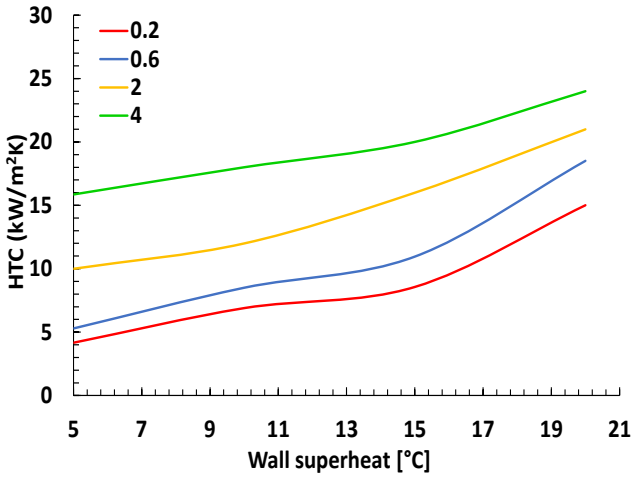


***Figure 53*** *HTC vs superheat at various aspect ratios, SPIP: 16.*

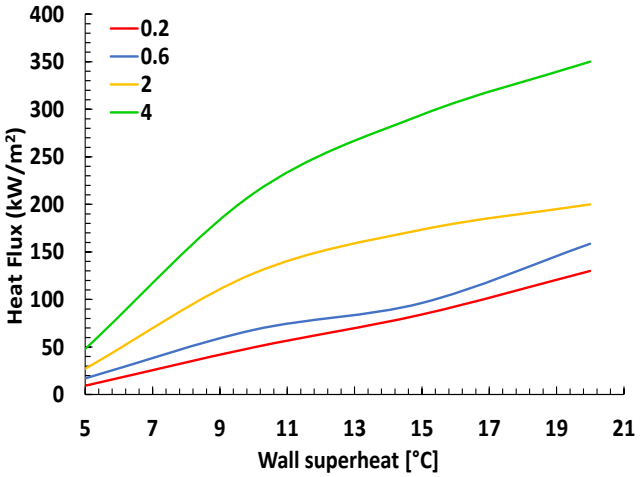


***Figure 54*** *Heat flux vs superheat at various aspect ratios, SPIP: 0.9.*

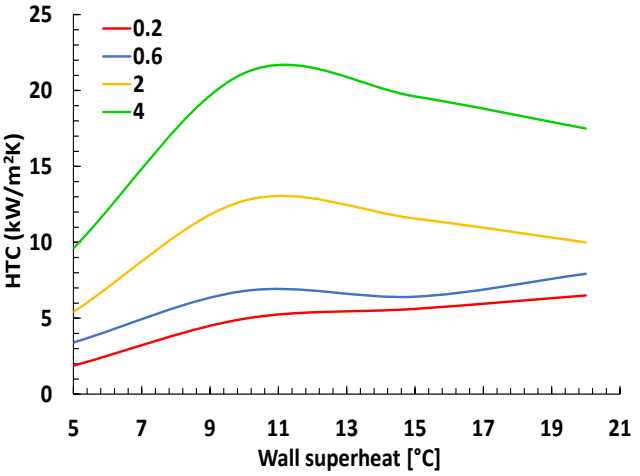


***Figure 55*** *HTC vs superheat at various aspect ratios, SPIP: 0.9.*

Figure 52 to Figure 55 compare the heat flux at different fin aspect ratios and SPIP. It is evident that fins with an aspect ratio of 4 show a higher HTC followed by a fin aspect ratio of 2, 0.6, and lastly 0.2. From this, it can be said that the higher the fin aspect ratio, the higher the HTC. This could be because when the aspect ratio increases, the fins become taller rather than wider, and when this happens, there is a bigger increase in total fin surface area. This increase in fin surface area means that there is a larger space to dissipate the same amount of heat, and thus cooler temperatures are achieved.

From Figure 55, it can also be seen that the dip in HTC is enhanced as the aspect ratio increases and that the dip is not present at the lowest aspect ratio of 0.2. Figure 56 may explain this because it shows that at higher aspect ratios, the gradient of the vapour curve is highest between wall superheat of 10 to 15 °C. This means that the

reason for the dip in HTC is due to the fact that vapour is being produced at a higher rate on the fin surface which prevents the liquid from coming into contact with the heated surface. At the same time, the nucleation site density remains the same for a fixed wall superheat across all fin aspect ratios, and thus the HTC decreases. It can also be noted from Figure 56 that at lower aspect ratios, the gradient of the vapour curve at wall superheat of 10 to 15 °C is either lower or same as the gradient at wall superheat of 15 to 20 °C, and for this reason, the dip in HTC is not seen.

Interestingly, when the fin aspect ratio is increased, the increase in heat flux also gets larger between consecutive aspect ratios. For instance, the increase in heat flux when the aspect ratio increases from 0.2 to 0.6 is smaller than when the aspect ratio increases from 0.6 to 2 and so on. This once again is due to the fins getting taller. When the fins get taller, they add twice as much of fin perimeter (from a 2D point of view) than when they get wider.

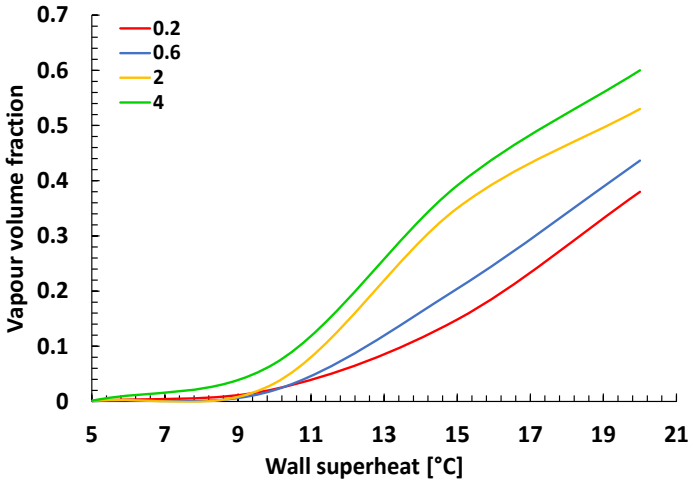


***Figure 56*** *Vapour fraction vs superheat at different aspect ratios, SPIP 0.9.*

When comparing the average surface vapour fraction, it can be noticed that higher aspect ratio fins have a higher amount of vapour on the heater surface. This is expected since higher aspect ratio fins were seen to have a higher heat flux. Another reason why surface vapour fraction increases with aspect ratio is that higher aspect ratio fins are taller and have a larger area between the fins where vapour can accumulate.

As mentioned previously, the fins' vertical faces produce the highest surface vapour fraction, whereas the horizontal faces have very little vapour on top of them. Since

higher aspect ratio fins have more vertical height, an increase in the average surface vapour fraction is expected.

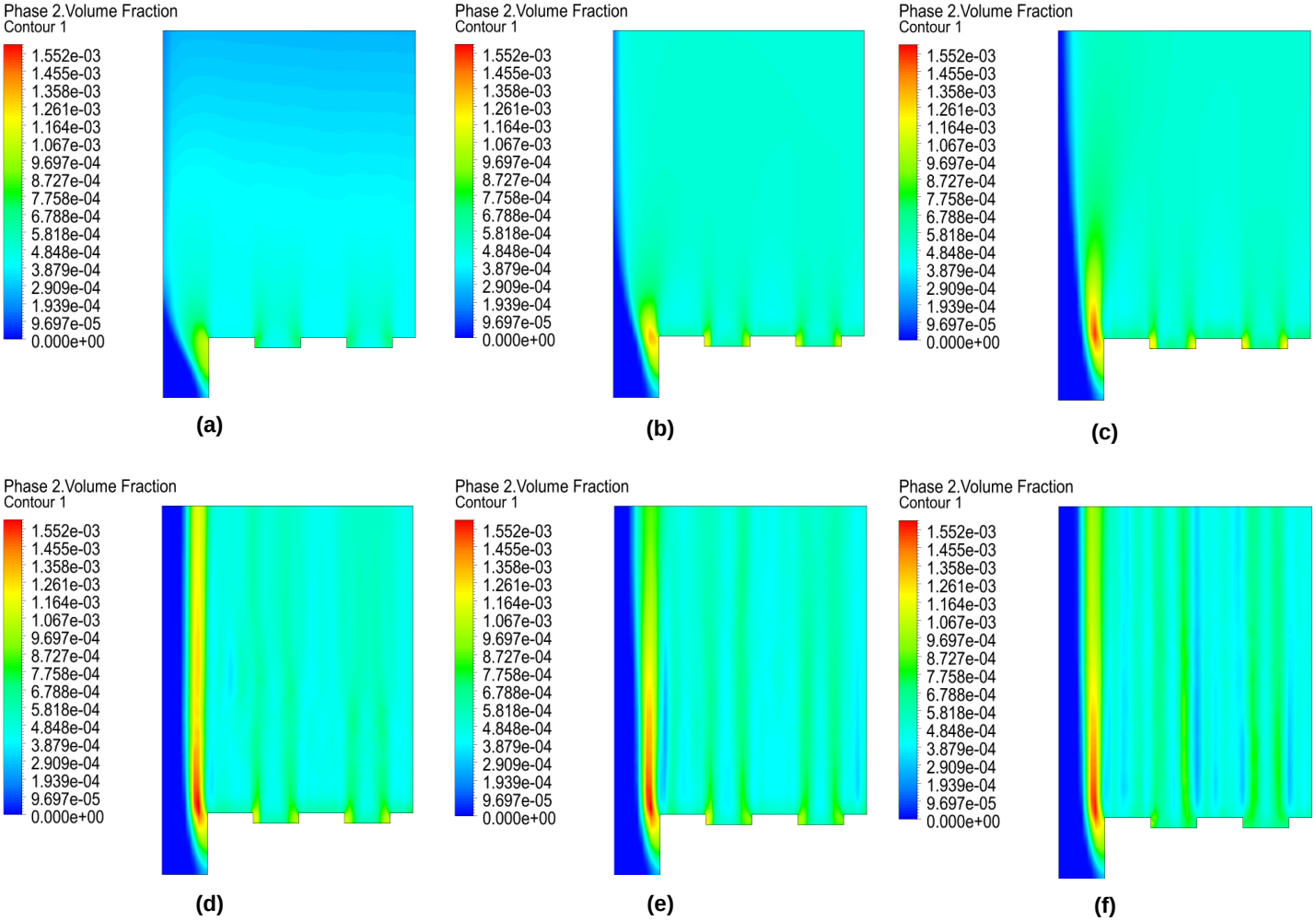


***Figure 57*** *Vapour fraction contours, fin aspect ratio 0.2 (a) 0.2 sec. (b) 0.6 sec. (c) 1.0 sec. (d) 1.5 sec. (e) 2.0 sec. (f) 2.5 sec.*

The vapour volume contour is shown for aspect ratios of 0.2 (Figure 57) and 4 (Figure 38). When the fin aspect ratio is 0.2, the highest vapour fraction is seen on the side of the heatsink, whereas for the fin aspect ratio of 4, it is seen in the region between two fins. It can also be noted that regardless of the aspect ratio, the top face of the fins has the least amount of vapour fraction. This is because the vertical section of the fins has a larger area and thus produces more vapour, which must first travel up the rest of the heated vertical section. It is interesting to note that at an aspect ratio of 0.2. However, the length of the vertical sections of the fins is shorter than the horizontal section. The vertical sections still have a higher vapour fraction on their surface.

## 5.5. Effect of number of fins

This section studies the effect of number of fins on the total heat flux and HTC. First, the number of fins is increased from 5, 9 and finally to 15. The aspect ratio, concentration, SPIP and fin spacing is kept constant during the investigation.

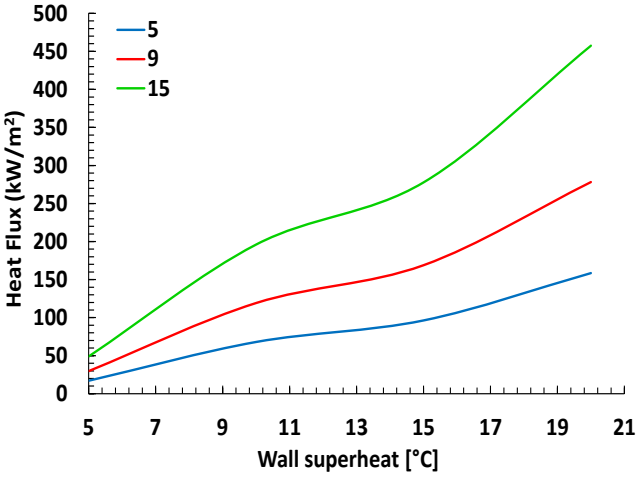


***Figure 58*** *Heat flux vs superheat at various fin numbers, SPIP: 0.9.*

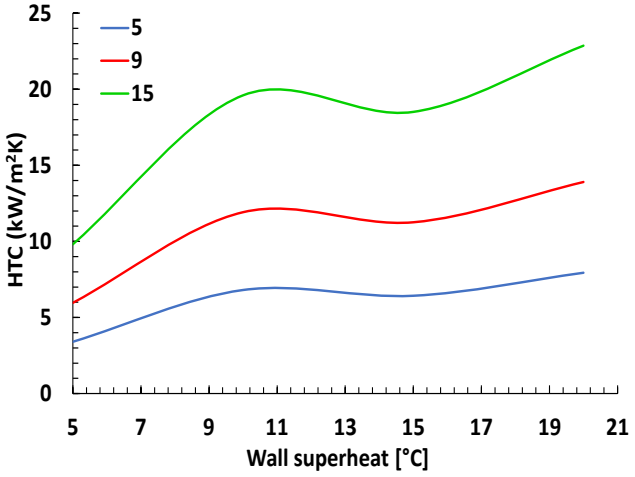


***Figure 59*** *HTC vs superheat at various aspect ratios, SPIP: 0.9.*

As the number of fins increases, the heat flux and the HTC increase, having more fins increases the heat transfer surface area, and thus cooler temperatures can be achieved when the same amount of heat is being transferred.

The vapour volume fraction and the fin shear stress at a given wall superheat are identical since the fin aspect ratio, and spacing remain the same. As a result, nucleation site density, bubble departure diameter, and departure time remain the same as these are temperature-dependent parameters. This means that the heat sink with a higher fin number has lower nucleation site density and bubble departure diameter since the surface temperature will be lower.

## 5.6. Effect of base fluid

In this section, different base fluids with $Al_2O_3$ particles are compared. The comparison is made between water and the refrigerants R141b, R134a, and R245fa, some of the commonly used base fluids for pool boiling application. The same bubble waiting time coefficients were used for all types of base fluids. The fin aspect ratio, the number of fins, and concentration were kept constant.

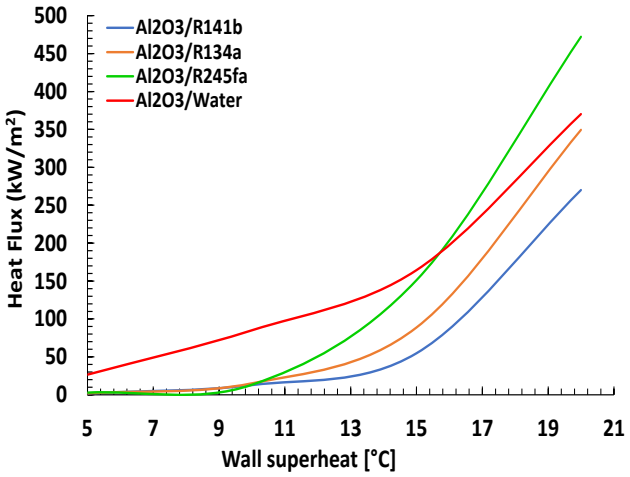


***Figure 60*** *Heat flux vs superheat using different base fluids, SPIP: 16.*

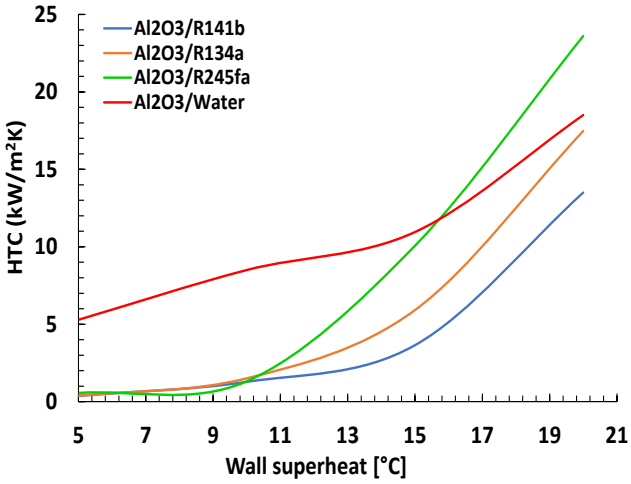


***Figure 61*** *HTC vs superheat using different base fluids, SPIP: 16.*

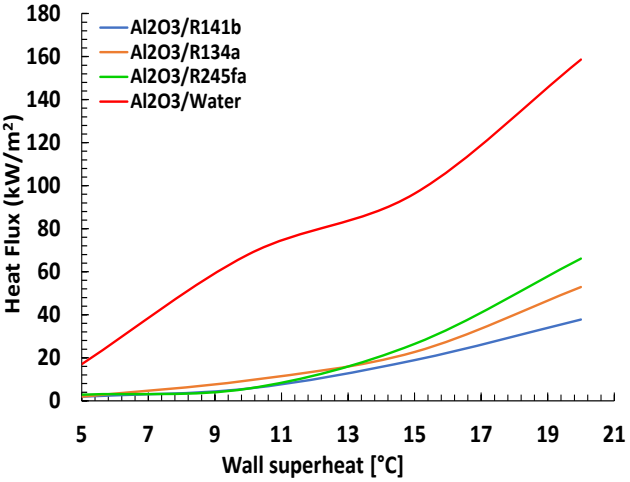


***Figure 62*** *Heat flux vs superheat using different base fluids, SPIP: 0.9.*

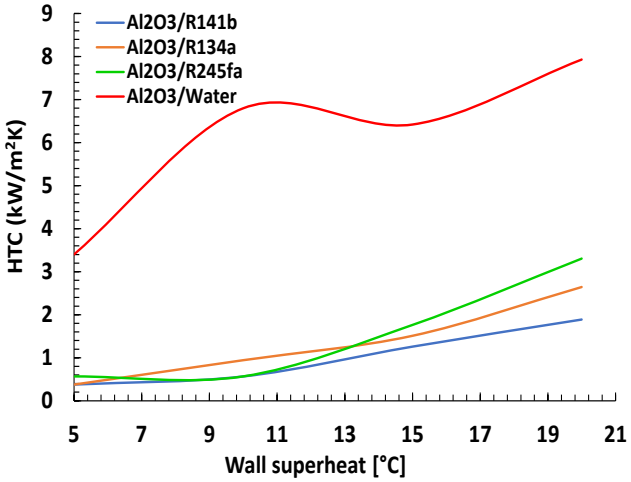


***Figure 63*** *HTC vs superheat using different base fluids, SPIP: 0.9.*

Figure 60 to Figure 63 shows the heat flux and HTC for nanofluids with water and different refrigerants as base fluid. It is noticeable that regardless of SPIP, at low wall superheats, the refrigerant-based nanofluids have a very low heat flux and HTC than water-based nanofluid. At SPIP 0.9, the refrigerant-based nanofluids always have a far lower heat flux and HTC at all wall superheat temperatures than water-based nanofluids. However, at higher superheats at SPIP 16, the refrigerant-based nanofluids have heat flux and HTC values that are much closer to the water-based nanofluid. In fact, it is seen that at SPIP 16, the heat flux and HTC of R245FA based nanofluid surpasses that of the water-based nanofluid.

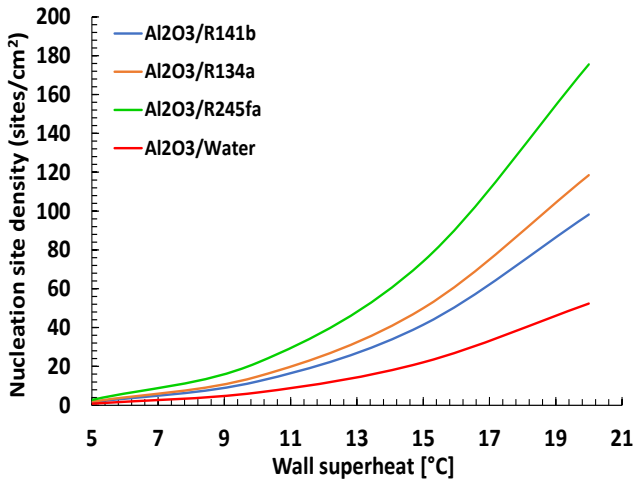


***Figure 64*** *NSD vs superheat using various base fluids, SPIP: 16.*

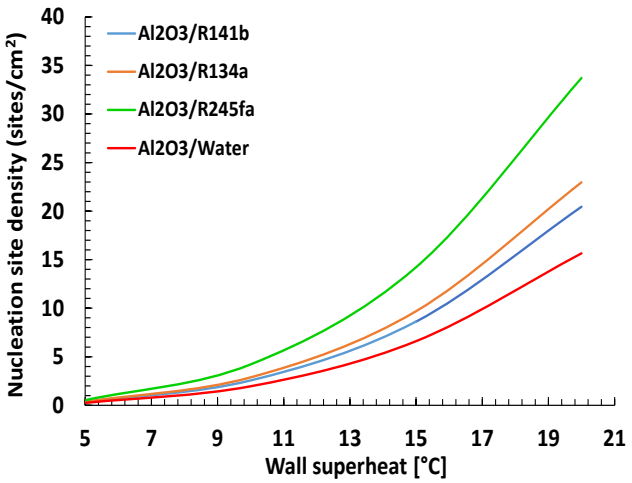


***Figure 65*** *NSD vs superheat using various base fluids, SPIP: 0.9.*

Although the refrigerant-based nanofluids have a much higher nucleation site density than water-based nanofluid as suggested by Figure 64 and Figure 65, the reason why refrigerant-based nanofluids have much lower heat flux values at SPIP 0.9 and lower superheat temperatures at SPIP 16 could be because refrigerants have thermal conductivity values that are about six times lower than that of water. For this reason, even though there are fewer nucleation sites when water-based nanofluid is used, the higher thermal conductivity greatly increases the heat transfer.

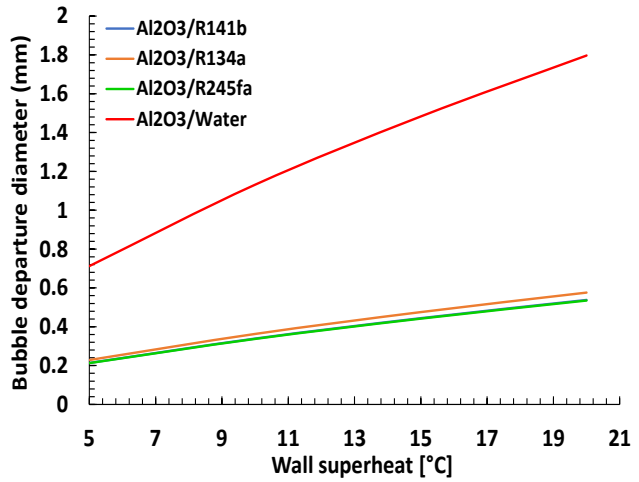


***Figure 66*** *BDD vs superheat using different base fluids, SPIP: 0.9.*

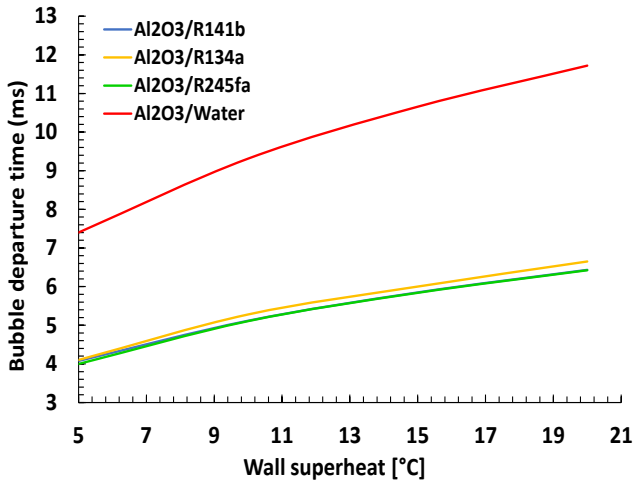


***Figure 67*** *BDT vs superheat using different base fluids, SPIP: 0.9.*

Bubble departure diameter is a function of several parameters, including surface tension and latent heat of vaporization. Since water has a surface tension that is up to 4 times higher and heat of vaporization that is up to 11 times higher than refrigerant-based nanofluids in this study, the bubble departure diameter for water-based nanofluid is much larger compared to refrigerant based nanofluids which have much

smaller bubble diameter (Figure 66). Smaller bubbles allow for more nucleation sites in the same area, thus increasing the nucleation site density. For this reason, at high superheat values at SPIP 16, refrigerant-based nanofluids start showing heat flux and HTC values that are closer to that of water-based nanofluid despite having lower thermal conductivity values. Thus, it can be said that the much higher nucleation site density at higher superheat temperatures for refrigerant-based nanofluid greatly influences the heat transfer to the point that it makes up for its low thermal conductivity.

Figure 68 shows the vapour volume fraction on the heater surface where the left vertical axis shows values for water-based nanofluid whereas the right vertical axis shows values for refrigerant-based nanofluids. It is interesting to note that the refrigerant-based nanofluids have far less vapour on the surface heater. This is expected since the refrigerant-based nanofluids have much smaller heat flux values, and so the vapour is produced at a slower rate. Water-based nanofluid has the highest vapour on the heater surface, followed by R245fa, R134a and R141b.

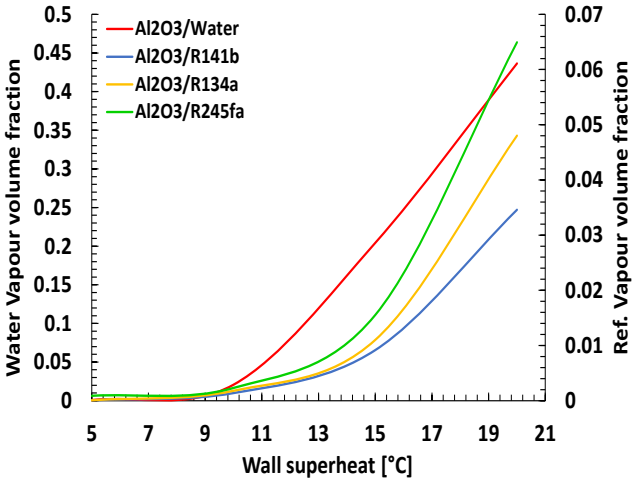


***Figure 68*** *Vapour fraction vs superheat using various base fluids, SPIP: 0.9.*

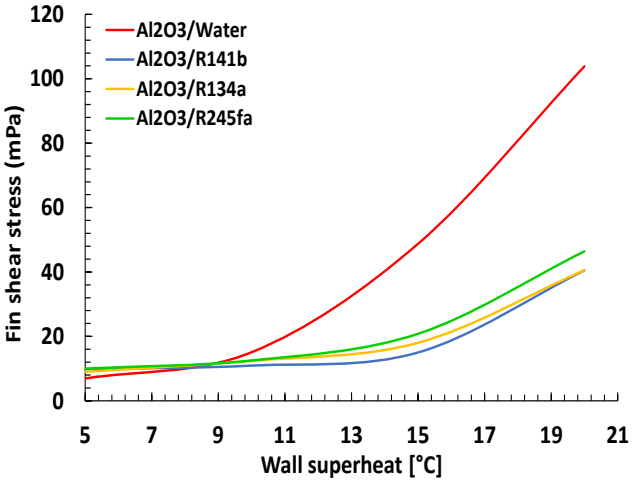


***Figure 69*** *shear stress vs superheat using various base fluids, SPIP: 0.9.*

This order is the same when comparing fin shear stress values (Figure 69). The refrigerant-based nanofluids also have a much lower liquid fin shear stress value despite having a higher viscosity. This could only mean that the surface liquid velocity gradients are lower for refrigerant-based nanofluids.

# 6. CONCLUSION

The investigations show that the heat flux decreases as SPIP approaches 1 and increases as it goes further from 1. This could be because when SPIP is near 1, the nanoparticles deposit on the heating surface and clog the cavities since the nanoparticles and cavities are the same sizes. This prevents bubble growth, and thus, the heat flux decreases. When the SPIP is smaller than 1, the particles are larger than the cavities, so they can sit on top of cavities but cannot clog them completely. For this reason, the heat flux when SPIP is lower than 1 is still higher than when SPIP is close to 1. When the SPIP is greater than 1, the particles are smaller than the cavities, and when particle deposition occurs on the heater surface, the particles split the existing cavities into two or smaller cavities where a higher number of smaller bubbles grow. This increases the number of nucleation sites, and as a result, the heat flux also increases. The deposition thickness was not directly simulated as it would dramatically increase in the complexity and computation time of the simulation. Clogging is taken into account while calculating the nucleation site density in Eq. 46. Clogging occurs when the roughness and the particle size are nearly the same (SPIP 1) and as seen in Figure 51, Eq. 46 took this into account by showing a decrease in nucleation sites which is the effect of clogging.

With an increase in concentration, the heat flux decreases possibly due to higher deposition thickness. At 2% vol. concentration, HTC enhancement is seen only at SPIP 8 and SPIP 16 when compared to pure water, whereas at 1% vol. concentration, HTC enhancement is seen at all SPIP except SPIP 0.9 and SPIP 0.5. At 0.5% vol. concentration, HTC enhancement is seen at all SPIP except SPIP 0.9.

As the aspect ratio and the number of fins increases, the heat flux increases due to a higher heat transfer surface area. However, there is a dip in HTC as the wall superheat temperature increases from 10 to 15 °C at fin aspect ratios of 0.6 and higher regardless of the number of fins. This dip is enhanced as the aspect ratio and the number of fins increases. When comparing base fluids, it was found that water-based nanofluids mostly have a higher heat flux value. However, at SPIP 16, it was found that R245FA based nanofluid has higher heat flux values than water at higher superheat temperatures.

## Future work

Future work would consist of a full 3D simulation taking directly into account the particle deposition and clogging and validated against the author's own experimental findings.

# 7 REFERENCES


Abadi, S.M.A.N.R., Ahmadpour, A. and Meyer, J.P., Numerical simulation of pool boiling on smooth, vertically aligned tandem tubes. *International Journal of Thermal Sciences,* Vol. 132, 2018, 628-644.

Adio, S.A., Mohsen, S. and Meyer, J.P., Influence of ultrasonication energy on the dispersion consistency of Al2O3–glycerol nanofluid based on viscosity data, and model development for the required ultrasonication energy density, *Journal of Experimental Nanoscience*, Vol. 11(8), 2016, 630-649.

Adio, S.A., Sharifpur, M. and Meyer, J.P., Investigation into Effective Viscosity and Electrical Conductivity of γ-Al2O3-Glycerol Nanofluids in Einstein Concentration Regime, *Heat Transfer Engineering*, Vol .36, 2013, 1241-1251.

Agarwal, R., Verma, K., Agrawal, N.K., Duchaniya, R.K. and Singh R., Synthesis, characterization, thermal conductivity and sensitivity of CuO nanofluids, *Applied Thermal Engineering*, Vol 102, 2016, 1024-1036.

Ahmadi, M.H., Nazari, M.A., Ghasempour, R., Madah, H., Shafii, M.B. and Ahmadi, M.A., Thermal conductivity ratio prediction of $Al_2O_3$/water nanofluid by applying connectionist methods, *Colloids and Surfaces A: Physicochemical and Engineering Aspects,* Vol 541, 2018, 154-164.

Ahmadpour, A., Abadi, S.M.A.N.R. and Meyer, J.P., Numerical investigation of pool boiling on a staggered tube bundle for different working fluids, *International Journal of Multiphase Flow,* Vol. 104, 2018, 89-102.

Ahmed, O., Hamed, M.S., Experimental investigation of the effect of particle deposition on pool boiling of nanofluids, *International Journal of Heat and Mass Transfer,* Vol. 55(13-14), 2012, 3423-3436.

Akbari, M., Galanis, N. and Behzadmehr, A., Comparative analysis of single and two-phase models for CFD studies of nanofluid heat transfer, *International Journal of Thermal Sciences,* Vol. 50(8), 2011, 1343-1354.

Alawi, O.A., Sidik, N.A.C., Xian, H.W., Kean, T.H. and Kazi, S.N., Thermal conductivity and viscosity models of metallic oxides nanofluids, *International Journal of Heat and Mass Transfer*, Vol 116, 2018, 1314–1325.

Ali, N., Teixeira, J.A. and Addali, A., A Review on Nanofluids: Fabrication, Stability, and Thermophysical Properties, *Journal of Nanomaterials,* 2018,

ANSYS, 2017. *Ansys Fluent Theory Guide.* [Online] Available at: http://www.ansys.com

Antal, S.P., Lahey Jr, R.T. and Flaherty, J.E., Analysis of phase distribution in fully developed laminar bubbly two-phase flow, *International Journal of Multiphase Flow,* Vol. 17(5), 1991, 635-652.

Ayoobi, A., Khorasani, A.F. and Tavakoli, M.R., The effects of subcooled temperatures on transient pool boiling of deionized water under atmospheric pressure, *AUT Journal of Mechanical Engineering,* Vol. 4, 2019, 67-78.

Ayoobia, A., Khorasani, A.F., Ramezanizadeh, M. and Afshari, A., Experimental investigation of transient pool boiling characteristics of Fe3O4 ferrofluid in comparison with deionized water, *Applied Thermal Engineering,* Vol. 179, 2020, 115642.

Azari, A., Kalbasi, M. and Rahimi, M., CFD and experimental investigation on the heat transfer characteristics of alumina nanofluids under the laminar flow regime, *Brazilian Journal of Chemical Engineering,* Vol. 31, 2014, 469-481.

Bang, C. and Chang, S.H., Boiling heat transfer performance and phenomena of $Al_2O_3$–water nano-fluids from a plain surface in a pool, *International Journal of Heat and Mass Transfer,* Vol. 48(12), 2005, 2407-2419.

Barreneche, C. *et al.* "Handbook on industrial applications of nanofluids in energy sector" Deliverable 11, 2020.

Behroyan, I., Ganesan, P., He, S. and Sivasankaran, S., CFD models comparative study on nanofluids subcooled flow boiling in a vertical pipe, *Numerical Heat Transfer, Part A: Applications,* Vol. 73(1), 2018, 55-74.

Benjamin, R.J. and Balakrishnan, A.R., Nucleation Site Density in Pool Boiling of Saturated Pure Liquids, *Experimental Thermal and Fluid Science,* Vol.15(1), 1997, 32-42.

Bergles, A.E., Nirmalan, V., Junkhan, G.H. and Webb, R.L., Bibliography on augmentation of convective heat and mass transfer. *Heat transfer laboratory report HTL-19, lowa state university, 1979.*

Bhuiyan, M.H.U., Saidur, R., Amalina, M.A. and Mostafizur, R.M., Effect of surface tension on SiO2 - methanol nanofluids*, IOP Conf. Series: Materials Science and Engineering*, Vol 88, 2015.

Bock, B.D., Bucci, M., Markides, C.M., Thome, J.R. and Meyer, J.P., Pool boiling of refrigerants over nanostructured and roughened tubes, *International Journal of Heat and Mass Transfer,* Vol. 162, 2020, 120387.

Cengel, Y. and Ghajar, A.J., *Heat and Mass transfer fundamental and applications,* McGraw-Hill Education, 2015

Chauhan, A., 2017. *CPU Cooling in Data Center Using a Thermosiphon Loop with,* s.l.: Rochester Institute of Technology.

Chavan, D., Pise, A., Experimental Investigation of Effective Viscosity and Density of Nanofluids, *Materials Today: Proceedings,* Vol 16, 2019, 504–515.

Chen, G., Jia, M., Zhang, S., Tang, Y. and Wan, Z., Pool boiling enhancement of novel interconnected microchannels with reentrant cavities for high-power electronics cooling, *International Journal of Heat and Mass Transfer,* Vol. 156, 2020, 199836.

Chevalier, J., Tillement, O. and Ayela, F., Rheological properties of nanofluids flowing through microchannels, *Applied Physics Letters*, Vol. 91, 2007, 1–3.

Chopkar M., Sudarshan S., Das P.K. and Manna, I., Effect of Particle Size on Thermal Conductivity of Nanofluid. *The Minerals, Metals & Materials Society and ASM International*, Vol 39, 2008.

Chopkar, M., Das, A.K., Manna, I. and Das, P.K., Pool boiling heat transfer characteristics of ZrO2–water nanofluids from a flat surface in a pool, *Heat Mass Transfer,* Vol. 44, 2008, 999-1004.

Çiftçi, E. and Sözen, A., Heat transfer enhancement in pool boiling and condensation using h-BN/DCM and SiO2/DCM nanofluids: experimental and numerical comparison, *International Journal of Numerical Methods for Heat & Fluid Flow,* Vol. 30, 2020.

Cole, R., A photographic study of pool boiling in the region, *American Institute of Chemical engineers,* Vol. 6(4), 1960, 533-538.

Corcione, M., Empirical correlating equations for predicting the effective thermal conductivity and dynamic viscosity of nanofluids, *Energy Conversion and Management*, Vol. 52(1), 2001, 789–793.

Corcione, M., Heat transfer features of buoyancy-driven nanofluids inside rectangular, *International Journal of Thermal Sciences,* Vol. 49(9), 2010, 1536-1546.

Coursey, J.S. and Kim, J., Nanofluid boiling: the effect of surface wettability, *International journal of heat and fluid flow,* Vol. 29(6), 2008, 1557-1585.

Das, S. K., Putra, N., Thiesen, P. and Roetzel, W., Temperature Dependence of Thermal Conductivity Enhancement for Nanofluids, *ASME Journal of Heat Transfer*, Vol 125, 2003, 567–574.

Das, S.K., Narayan, G.P. and Baby, A.K, Survey on nucleate pool boiling of nanofluids: the effect of particle size relative to roughness, *Journal of nanoparticle research,* Vol. 10, 2008, 1099-1108.

Das, S.K., Putra, N. and Roetzel, W., Pool boiling characteristics of nanofluid, *International Journal Heat and Mass Transfer,* Vol.46(5), 2003, 851-862.

De Schepper, S.C.K., Heynderickx, G.J. and Marin, G.B., Modeling the evaporation of a hydrocarbon feedstock in the convection section of a steam cracker, *Indiana: Computers & Chemical Engineering,* Vol. 33(1), 2009, 122-132.

Del Valle, V.H. and Kenning, D.B.R., Subcooled flow boiling at high heat flux, *International Journal of Heat and Mass Transfer,* Vol. 28(10), 1985, 1907-1920.

Djbbenn, 2006. *Thermal paste and how to use it.* [Online] Available at: https://www.techpowerup.com/articles/overclocking/134

Eggers, J. R. and Kabelac, S., Nanofluids revisited, *Applied Thermal Engineering,* Vol. 106, 2016, 1114-1126.

Fan, S., Jiao, L., Wang, K. and Duan, F., Pool boiling heat transfer of saturated water on rough surfaces with the effect of roughening techniques, *International Journal of Thermal Sciences,* Vol. 159, 2020, 120054.

Faulkner, D. and Khotan, M., Practical design of a 1000 W/cm2 cooling system. *Annual IEEE Semiconductor Thermal Measurement,* 2013, 223-230.

Feldmann, H. and Luke, A., Nucleate Boiling in Water for Different Pressures, *International Refrigeration and Air Conditioning conference,* 2008

Gobinath, N., Venugopal, T., Palani, K. and Samuel, A.A., Numerical modelling of thermophoresis in water-alumina nanofluid under pool boiling conditions, *International Journal of Thermal Sciences,* Vol. 129, 2018, 1-13.

Golorin, V.S., Kol'chugin, B.A. and Zakharova, E.A., Investigation of the mechanism of nucleate boiling of ethyl alcohol and benzene by means of high-speed motion-picture photography, *Heat Transfer Research,* Vol.10(4), 1978, 79-98.

Golubovic M.N., Hettiarachchi, H.D.M., Worek, W.M., Minkowycz, W.J., Nanofluids and critical heat flux, experimental and analytical study, *Applied Thermal Engineering,* Vol. 29, 2009, 1281-1288.

Gorenflo, D., Pool boiling, *VDI Heat Atlas (English version),* 1993

Gouda, R.K., Pathak, M. and Khan, M.K., Pool boiling heat transfer enhancement with segmented finned microchannels structured surface, *International Journal of Heat and Mass Transfer,* Vol. 127, 2018, 39-50.

Gupta, R.R., Bhambi, S. and Agarwal, V.K., CFD modeling for nucleate pool boiling of nanofluids, *An International Journal of Computation and Methodology,* Vol. 75(6), 2019, 402-412.

Li, H., Vasquez, S.A., Punekar, H. and Muralikrishnan, R., *Prediction of Boiling and Critical Heat Flux Using an Eulerian Multiphase Boiling* Model*. Fluids and Thermal Systems; Advances for Process Industries*, Vol. 6, 2011, 463-476.

Ham, J. and Cho, H., Theoretical analysis of Pool boiling characteristics of $Al_2O_3$ nanofluid, *Applied Thermal Engineering,* Vol. 108, 2016, 158-171.

Ham, J., Kim, H., Shin, Y. and Cho, H., Experimental investigation of pool boiling characteristics in Al2O3 nanofluid according to surface roughness and concentration, *International Journal of thermal science,* Vol. 144, 2017, 86-97.

Harish, G., Emlin, V. and Sajith, V., Effect of surface-particle interactions during pool boiling of nanofluids, *International journal of thermal science,* Vol. 50(12)*,* 2011, 2318-2327.

He, Y.R., Li, H.R., Hu, Y.W., Wang, X.Z. and Zhu, J.Q., Boiling heat transfer characteristics of ethylene glycol and water mixture based ZnO nanofluids in a cylindrical vessel, *International Journal of Heat and Mass Transfer,* Vol. 98, 2016, 611–615

Heris, S. Z., Experimental investigation of pool boiling characteristics of low-concentrated CuO/ethylene glycol–water nanofluids, *International Communications in Heat and Mass Transfer,* Vol. 38, 2011, 1470-1473.

Hsu, H.Y., Lin, M.C, Popovic, B., Lin, C.R. and Patankar, N.A., A numerical investigation of the effect of surface wettability on the boiling curve, *Plos One,* Vol. 12 (11), 2017, e0187175.

Huang, C.K., Lee, C.W. and Wang, C.K., Boiling enhancement by TiO2 nanoparticle deposition, *International Journal of Heat and Mass Transfer,* Vol. 54(23-24), 2011, 4895-903.

Jia-Fei, Z. and Zhong-Yang, L., Dependence of nanofluid viscosity on particle size and pH value, *Chinese Physics Letter*, Vol. 26(6), 2009, 10–13.

Jones, B.I., McHale, J.P. and Garimella, S.V., The influence of surface roughness on nucleate pool boiling heat transfer, *Journal of heat transfer,* Vol. 131, 2009.

Kamel, M.S., Al-agha, M.S., Lezsovits, F. and Mahian, O., Simulation of pool boiling of nanofluids by using Eulerian multiphase model, *Journal of Thermal Analysis and Calorimetry*, Vol. 142, 2019, 439-505

Kamel, M.S. and Lezsovits, F., Enhancement of pool boiling heat transfer performance using dilute cerium oxide/water nanofluid: An experimental investigation, *International Communications in Heat and Mass Transfer,* Volume 114, 2020, 104587.

Kathiravan, R., Kumar, R., Gupta, A. and Chandra, R., Preparation and pool boiling characteristics of copper nanofluids over a flat plate heater, *International Journal of Heat and Mass Transfer,* Vol. 53(9-10), 2010, 1673-1681.

Kathiravan, R., Kumar, R., Gupta, A. and Chandra, R., Characterization and Pool Boiling Heat Transfer Studies of Nanofluids, *J. Heat Transfer,* Vol. 131(8), 2009, 081902.

Kenning, D. B. R., 2011. *Pool boiling.* [Online] Available at: http://www.thermopedia.com/content/1046/

Khanafer, K. and Vafai, K., A critical synthesis of thermophysical characteristics of nanofluids, *International Journal of Heat and Mass Transfer,* Vol. 54(19-20), 2011, 4410-4428.

Khooshehchin, M., Mohammadidoust , A. and Ghotbinasab, S., An optimization study on heat transfer of pool boiling exposed ultrasonic waves and particles addition, *International Communications in Heat and Mass Transfer,* Vol. 114, 2020, 104558.

Kim, H., Kim, J. and Kim, M.W., Effect of nanoparticles on CHF enhancement in pool boiling of nano-fluids, *International Journal of Heat and Mass Transfer,* Vol. 49*,* 2006, 5070-5074.

Kim, H., Hwang, I. and Kim, S., Numerical study on the pool boiling heat transfer of water-based nanofluids on a vertical surface, *Journal of Nanotscience and Nanotechnology,* Vol. 17, 2017, 8404-8410.

Kim, J., Jun, S., Lakshnaraian, R. and You, S.M., Effect of surface roughness on pool boiling heat transfer at a heated surface having moderate wettability, *International Journal of Thermal Sciences,* Vol. 101, 2016, 992-1002.

Kim, J.S., Shin, D.H., You, S.M. and Lee, J., Pool boiling heat transfer on bare and microporous surfaces confined in a narrow gap, *International Journal of Heat and Mass Transfer,* Vol. 162, 2020, 120-129.

Kim, S.J., Bang, I.C., Buongiorno, J. and Hu, L.W., Surface wettability change during pool boiling of nanofluids and its effect on critical heat flux, *International Journal of Heat and Mass Transfer,* Vol. 50,(19-20)*,* 2007, 4105-4116.

Kim, Y.C, Effect of surface roughness on pool boiling heat transfer in subcooled water-CuO nanofluid, *Journal of Mechanical Science and Technology,* Vol. 28 (8), 2014, 3371-3376

Krepper, E., Končar, B. and Egorov, Y., CFD modelling of subcooled boiling — concept, validation and application to fuel assembly design, *Nuclear Engineering and Design,* Vol. 237(7), 2007, 716-731.

Kshirsagar, J.M. and Shrivastava, R., Experimental investigation of nucleate pool boiling characteristics of high concentrated alumina/water nanofluids, *Heat and Mass Transfer,* Vol. 54, 2018, 1779-1790.

Kurul, N. Podowski, M., Multidimensional effects in forced-convection subcooled boiling, *International Heat Transfer Conference Digital Library,* Vols. 1-7, 1990, 21-26.

Kwark, S.M., Kumar, R., Moreno, G., Yoo, J. and You, S.M., Pool boiling characteristics of low concentration nanofluids, *International Journal of Heat and Mass Transfer,* Vol. 53(5-6), 2011, 972-981.

Lasance, C. J. M., 2005. *Advances In High-Performance Cooling For Electronics.* [Online] Available at: https://www.electronics-cooling.com/2005/11/advances-in-high-performance-cooling-for-electronics/

Lee, S., Choi, S.U.S., Li, S. and Eastman, J. A., Measuring Thermal Conductivity of Fluids Containing Oxide Nanoparticles, *ASME Journal of Heat Transfer*, Vol 121, 1999, 280–289.

Li, C.H. and Peterson, G. P. Experimental investigation of temperature and volume fraction variations on the effective thermal conductivity nanoparticle suspensions (nanofluids), *Journal of Applied Physics*, Vol. 99, 2006.

Li, X., Li, K., Tu, J. and Buongiorno, J., On two-fluid modeling of nucleate boiling of dilute nanofluids, *International Journal of Heat and Mass Transfer,* Vol. 69, 2014, 443-450.

Li, X., Yuan.Y. and Tu, J., A parametric study of the heat flux partitioning model for nucleate boiling of nanofluids, *International Journal of Thermal Sciences,* Vol. 98, 2015, 42-50.

Li, Z., Sarafraz, M.M., Mazinani, A., Hayat, T., Alsulami, H. and Goodarzi, M., Pool boiling heat transfer to CuO-H2O nanofluid on finned surfaces, *International Journal of Heat and Mass Transfer,* Vol. 156, 2020, 119780.

Liu, Z.H. and Liao, L., Sorption and agglutination phenomenon of nanofluids on a plain heating surface, *International Journal of Heat and Mass Transfer,* Vol. 51(9-10)*,* 2008, 2593-2602.

Liu, Z.H., Xiong, J.G. and Bao, R., Boiling heat transfer characteristics of nanofluids in a flat heat pipe evaporator with micro-grooved heating surface, *International Journal of Multiphase Flow,* Vol. 33(12), 2007*,* 1284-1295.

LiLi, G., Lin, Z., ZhiLei, M., Chen, X., ZhangPing, X., MingZhao, D., The Numerical Simulation of Flow and Boiling Heat Transfer of Two Phases in Horizontal Tube, *Asia-Pacific Power and Energy Engineering Conference,* 2012.

Lotfi, R., Saboohi, Y. and Rashidi, A.M., Numerical study of forced convective heat transfer of Nanofluids: Comparison of different approaches, *International Communications in Heat and Mass Transfer,* Vol. 37, 2010, 74-78.

Mahdavi, M., Sharifpur, M. and Meyer, J.P., Exploration of nanofluid pool boiling and deposition on a horizontal cylinder in Eulerian and Lagrangian frames, *International Journal of Heat and Mass Transfer,* Vol. 125, 2018, 959-971.

Manetti, L.L., Kiyomura, I.S., Cunha, A.P, Junior, M.A.S.P. and Cardoso, E.M, Surface roughness and nanofluid concentration effects on the surface wettability and nanofluid boiling heat transfer, *Brazillian Congress of Thermal Sciences and Engineering,* Vol. 16, 2016.

Meissner, H.P. and Michaels, A.S., Surface Tensions of Pure Liquids and Liquid Mixtures, *Industrial and enginnering chemistry,* Vol. 41(12), 1949, 2782-2787.

Mesquita, A.Z. and Rodrigues, R.R., Detection of the Departure from Nucleate Boiling in Nuclear Fuel Rod Simulators, *International Journal of Nuclear Energy, 2013.*

Minocha, N., Joshi, J.B., Nayak, A.K., Vijayan, P.K., 3D CFD simulation of passive decay heat removal system under boiling conditions: Role of bubble sliding motion on inclined, *Chemical Engineering Science,* Vol. 145*,* 2016, 245-265.

Mohammed, H. I., Giddings, D. and Walker, G.S., CFD simulation of a concentrated salt nanofluid flow boiling in a rectangular tube, *International Journal of Heat and Mass Transfer,* Vol. 125*,* 2018, 218-228.

Murshed, S.M.S., Leong, K.C. and Yang, C., Enhanced thermal conductivity of TiO2—water based nanofluids, *International Journal of Thermal Sciences,* Vol 44(4), 2005, 367-373.

Naghibzadeh, S.M., Goharkhah, M., Sharifpur, M. and Meyer, J.P., Effects of interphase momentum exchange models on simulation of subcooled flow boiling, *International Communications in Heat and Mass Transfer,* Vol. 118, 2020, 104863.

Narayan, G.P., Anoop, K. and Das, S.K., Mechanism of enhancement/deterioration of boiling heat transfer using stable nanoparticle suspensions over vertical tubes, *Journal of Applied Physics*, Vol. 107(7), 2007, 074317-074317-7.

Nazari, A. and Saedodin, S., An experimental study of the nanofluid pool boiling on the aluminium surface, *Journal of Thermal Analysis and Calorimetry,* Vol. 135(3), 2019, 1753-1762.

Nguyen, C.T., Desgranges, F., Roy, G., Galanis, N., Maré, T., Boucher, S. and Angue Mintsa, H., Temperature and particle-size dependent viscosity data for water-based nanofluids – Hysteresis phenomenon, *International Journal of Heat and Fluid Flow*, Vol. 28(6), 2007, 1492–1506.

Okawa, T., Takamura, M. and Kamiya, T., Boiling time effect on CHF enhancement in pool boiling of nanofluids, *International Journal of Heat and Mass Transfer,* Vol. 55(9-10), 2012, 2719-2725.

Park, K.J., Jung, D. and Shim, S.E., Nucleate boiling heat transfer in aqueous solutions with carbon nanotubes up to critical heat fluxes, *International Journal of Multiphase Flow,* Vol. 35, 2009, 525-532.

Pham, Q.T., Kim, T.I., Lee, S.S. and Chang, S.H., Enhancement of critical heat flux using nano-fluids for invessel retention-external vessel cooling, *Applied Thermal Engineering,* Vol. 35, 2012, 157-165.

Raja, R.A.A., Sunil, J. and Maheswaran, R., Estimation of Thermo-Physical Properties of Nanofluids using Theoretical Correlations, *International Journal of Applied Engineering Research ISSN 0973-4562,* Vol 13(10), 2018, 7950-7953.

Rejvani, M., Alipour, A., Vahedi, S.M., Chamkha, A.J. and Wongeises, S., Optimal characteristics and heat transfer efficiency of SiO2/water nanofluid for application of energy devices: A comprehensive study, *International Journal of Energy Research,* Vol.43 (14), 2019, 8548-8471.

Ren, S. and Zhou, W., Numerical investigation of nucleate pool boiling outside a vertical tube under sub-atmospheric pressures, *International Communications in Heat and Mass Transfer,* Vol. 116, 2020, 104662.

Rostami, S., Raki, E., Abdollahi, A. and Goldanlou, A.S., Effects of different magnetic fields on the boiling heat transfer coefficient of the NiO/deionized water nanofluid, an experimental investigation, *Powder Technology,* Vol. 376, 2020, 398-409.

Sahoo, B.C., Vajjha, R.S., Ganguli, R., Chukwu, G.A. and Das, D.K., Determination of Rheological Behaviour of Aluminium Oxide Nanofluid and Development of New Viscosity Correlations, *Petroleum Science and Technology*, Vol. 27, 2009, 1757–1770.

Salman, B.H., Mohammed, H.A. Munisamy, K.M. and Kherbeet, A.S., Characteristics of heat transfer and fluid flow in microtube and microchannel using conventional fluids and nanofluids, *Renewable sustainable energy,* Vol. 28, 2013, 848-880.

Sarafraz, M.M.and Hormozi, F., Experimental investigation on the pool boiling heat transfer to aqueous multi-walled carbon nanotube nanofluids on the micro-finned surfaces, *International Journal of Thermal Science,* Vol. 100, 2016, 255-266.

Sato, Y. and Niceno, B., Pool boiling simulation using an interface tracking method, *International Journal of Heat and Mass Transfer,* Vol.125, 2018, 876-890.

Seong, D.P., Sung, B.M., and Bang, C., Effect of thickness of boiling-induced nanoparticle deposition on the saturation of critical heat flux enchacement, *School of Mechanical and Nuclear Engineering*, 689-798, 2014.

Sharifpur, M., Tshimanga, N., Meyer, J.P. and Manca, O., Experimental investigation and model development for thermal conductivity of α-Al2O3-glycerol nanofluids, *International Communications in Heat Mass Transfer,* Vol 85, 2017, 12–22.

Sharifpur, M., Yousefi, S. and Meyer, J.P., A new model for density of nanofluids including nanolayer, *International Communications in Heat and Mass Transfer*, Vol. 78, 2016, 168-174.

Sheikhbahai, M., Esfahany, M.N. and Etesami, N., Experimental investigation of pool boiling of Fe3O4/ethylene glycol-water nanofluid in electric field, *International Journal of Thermal Sciences,* Vol. 62, 2012, 149-153.

Shetty, A.A., Ghosh, P., Mondal, S.S., Patra, N. and Singh, R.S., Effective numerical model for flow boiling of a nanofluid, *International Journal of Thermal Technologies,* Vol. 7(2), 2017, 105-107.

Shoghl, S.N. and Bahrami, M., Experimental investigation on pool boiling heat transfer of ZnO, and CuO water-based nanofluids and effect of surfactant on heat transfer coefficient, *International Communications in Heat and Mass Transfer,* Vol. 45, 2013, 122-129.

Simon, D., Paz, C., Eirís, A. and Suárez, E., Eulerian model for the prediction of nucleate boiling of refrigerant in heat exchangers, *Advanced Computational Methods and Experiments in Heat Transfer,* Vol. 11, 2010, 51-59.

Simpson, S., Schelfhout, A., Golden, C. and Vafaei, S., Nanofluid Thermal Conductivity and Effective Parameters, *Applied Sciences 9,* Vol 87(1), 2018.

Soltani, S., Etemad, S.G. and Thibault, J., Pool boiling heat transfer performance of Newtonian nanofluids, *Heat Mass Transfer,* Vol.45(12)*,* 2009, 1555-1560.

Sonawane, S.S., Khedkar, R.S. and Wasewar, K.L., Effect of sonication time on enhancement of effective thermal conductivity of nano TiO2–water, ethylene glycol, and paraffin oil nanofluids and models comparisons, *Journal of Experimental Nanoscience*, Vol. 10(4), 2015, 310-322.

Suriyawong, A. and Wongwises, S., Nucleate pool boiling heat transfer characteristics of TiO2–water nanofluids at very low concentrations, *Experimental Thermal and Fluid Science,* Vol. 34, 2010, 992-999.

Syam Sundar, L., Venkata Ramana, E., Singh, M.K. and De Sousa, a. C.M., Viscosity of low volume concentrations of magnetic Fe3O4 nanoparticles dispersed in ethylene glycol and water mixture, *Chemical Physics Letters*, Vol. 554, 2012, 236–242.

Timofeeva, E. V., Routbort, J.L. and Singh, D., Particle shape effects on thermophysical properties of alumina nanofluids, *Journal of Applied Physics*, Vol. 106(1), 2009.

Trisaksri, V. and Wongwises, S., Nucleate pool boiling heat transfer of TiO2–R141b nanofluids, *International Journal of Heat and Mass Transfer,* Vol. 52(5-6), 2009, 1582-1588.

Uppal, R., 2018. *Nanofluids for thermal management.* [Online] Available at: https://idstch.com/technology/energy/nanofluids-next-generation-solution-thermal-management-electronics-transformer-space-nuclear-systems-military-vehicles-submarines-power-electronics-directed-energy-weapons/

Vassallo, Kumar, R., D'Amico, S., Pool boiling heat transfer experiments in silica–water nano-fluids, *International Journal of Heat and Mass Transfer,* Vol. 47, 2004, 407–411.

Walters, R., 2012. *Cool your pc by submerging it in oil.* [Online] Available at: https://www.geek.com/geek-cetera/cool-your-pc-by-submerging-it-in-oil-1495403/

Wang, J., Mengzhen, D. and Xueling, L., Numerical simulation of pool boiling with special heated surfaces, *International Journal of Heat and Mass Transfer,* Vol. 130, 2019, 460-468.

Wang, X., Xu, X. and Choi, S.U., Thermal Conductivity of Nanoparticle - Fluid Mixture, *Journal of Thermophysics and Heat Transfer*, Vol. 13(4), 1999, 474–480.

Wang, X.J. and Li, X.F., Influence of pH on Nanofluids' Viscosity and Thermal Conductivity, *Chinese Physics Letter*, Vol 26, 2009.

Wei, L., Dai, R., Zeng, M. and Wang, Q., Review of two types of surface modification on pool boiling enhancement: Passive and active, *Renewable and Sustainable Energy Reviews,* Vol. 130, 2020, 109926.

Wen, D. and Ding, Y., Experimental investigation into the pool boiling heat transfer of aqueous based γ-alumina nanofluids, *Journal of Nanoparticle Research,* Vol. 7, 2005, 265-274.

Wen, D., Corr, M., Hu, X. and Lin, G., Boiling heat transfer of nanofluids: The effect of heating surface modification, *International Journal of Thermal Sciences,* Vol. 50, 2011, 480-485.

White, S.B., Shih, A.J. and Pipe, K.P., Effects of nanoparticle layering on nanofluid and base fluid pool boiling heat transfer from a horizontal surface under atmospheric pressure, *Journal of Applied Physics,* Vol. 107, 2010, 114302.

Witharana, S. 2003. Boiling of refrigerants on enchanced surface and boiling of nanofluids. *Ph.D. Thesis, Royal institute of technology, Stockhol, Sweden.*

Wu, H.L., Peng, X.F. Ye, P. and Gong, Y.E., Simulation of refrigerant flow boiling in serpentine tubes, *International Journal of Heat and Mass Transfer,* Vol. 50, 2007, 1186-1195.

Xie, H., Wang, J., Xi, T. and Liu, Y., Thermal Conductivity of Suspensions Containing Nanosized SiC Particles, *International Journal of Thermophysics,* Vol. 23, 2002, 571–580.

Yang, X.F. and Liu, Z.H., Pool boiling heat transfer of functionalized nanofluid under sub-atmospheric pressures, *International Journal of Thermal Sciences,* Vol. 50(12), 2011, 2402-2412.

Yang, Y.M. and Ma, J.R., Boiling of suspension of solid particles in water, *International Journal on Heat and Mass Transfer,* Vol. 27(1), 1984, 145-147.

Yao, S., Huang, X., Song, Y. and Zhang, S., Effects of nanoparticle types and size on boiling heat transfer performance under different pressures, *AIP Advances,* Vol. 8, 2018.

Yao, W. and Morel, C., Volumetric area prediction in upward bubbly two-phase flow, *International Journal of Heat and Mass Transfer,* Vol. 47(2), 2004, 307-328.

You, S.M., Kim, J.H., and Kim, K.H., Effect of nanoparticles on critical heat flux of water in pool boiling heat transfer, *Applied Physics Letters,* Vol. 83(16), 2003, 3374-3376.